Model Design and Analysis for Amorphous Materials

A dissertation presented to

the faculty of

the College of Arts and Sciences of Ohio University

In partial fulfillment

of the requirements for the degree

Doctor of Philosophy

Bin Cai

August 2011

This dissertation titled

Model Design and Analysis for Amorphous Materials

by

BIN CAI

has been approved for

the Department of Physics and Astronomy

and the College of Arts and Sciences by

David A. Drabold

Distinguished Professor of Physics

Howard D. Dewald

Interim Dean, College of Arts and Sciences

Abstract

CAI, BIN, Ph.D., August 2011, Physics

Model Design and Analysis for Amorphous Materials (112 pp.)

Director of Dissertation: David A. Drabold

In this work, I first introduce various modeling methods for amorphous materials. I discuss "melt-and-quench", computer alchemy and building block techniques for *ab-initio* modeling; RMC and INVERT for biased modeling. Based on these modeling methods, I present atomistic models for a-InN, a-GaN, a-$Ge_2Sb_2Te_5$, g-$Ge_2As_4Se_4$, g-$AsGe_{0.8}Se_{0.8}$, a-GeO_2, a-H_2O and B or P doped a-Si:H. By applying different analysis methods, I discuss the structural and electronic properties of these materials. I show a tetrahedral network with a tiny electronic gap for a-InN. The a-GaN model exhibits a similar network with a-InN but with a bigger gap. In the study of a-$Ge_2Sb_2Te_5$, I track the dynamic changes of network at 500 K, and correlate the structural changes in the course of the simulation with changes in electronic structure. For g-$Ge_2As_4Se_4$ and g-$AsGe_{0.8}Se_{0.8}$, I found that the 8-N rule is often violated in these two ternary chalcogenide glasses. I conclude that a-GeO_2 models exhibit similar tetrahedral structure with a-SiO_2. The low density a-H_2O model could be described as water molecules are packed in a way such that O atom with its first four O neighbors forms a tetrahedral structure with medium range order. The mechanism of H passivation in B or P doped a-Si:H are also discussed.

Approved: _____

David A. Drabold

Distinguished Professor of Physics

To Xueline (Mom) and Yimin (Dad).

Acknowledgments

Looking back over the past five years, it is an absolutely fantastic experience for me studying at Ohio University. I am extremely happy that I am able to achieve the goal of getting PhD in Physics and make my dream come true. At the end of this important chapter of my life, I would like to take this opportunity to express my deep gratitude to all people who help, encourage and support me throughout my academic career.

First and foremost, I want to say THANK YOU to Dr. David A. Drabold who is not only a great advisor but also a mentor, role model, friend to me. It is my great honor to work with him. I am really impressed with his wide knowledge of science, great enthusiasm for research and extreme kindness to people. I feel joyful and benefit a lot from each conversation and discussion with him. Without his guidance, there is no chance I could have any achievements in this field.

I am also very grateful to all collaborators in my research work. Their help and contribution are invaluable. I would like to thank Dr. Gang Chen who always gives me great suggestions from experimental aspect. I want to thank Dr. Stephen Elliott who invited me for research collaboration to Cambridge University. I am very grateful to Dr. Xiaodong Zhang who offered me an internship in MD Anderson Cancer Center. I also want to thank Dr. Andrew Goodwin, Dr. Himanshu Jain, Dr. James Lewis and Dr. Martin Kordesch for those helpful conversations and discussions.

I would like to thank all committee members for their time and suggestions when assembling this dissertation. I also want to thank all my former and current team members, especially, Dr. Mingliang Zhang, Dr. Fakhar Inam, Binay Prasai and Yuting Li, for their advice and support. I want to thank the Department of Physics and Astronomy and Ohio University providing me perfect working and studying environment.

Finally, I wish to express my profound gratitude to my parents. Their love and all time support is the major source of power for me to chase my dream and achieve my

goals. I also want to thank Fangchan Liang, my significant other, for her love, support and encouragement throughout this endeavor.

Table of Contents

Page

List of Tables

List of Figures

1 Chapter: Introduction

Amorphous materials, especially amorphous semiconductors, play an ever more important role in modern technology. Due to the applications in photovoltaics, infrared detectors, optoelectronic devices and FLASH memory, the physics of amorphous semiconductors has drawn renewed interest. By definition, amorphous solids are disordered materials which lack translational periodicity. Compared with crystals, because of the absence of long-range order, the traditional diffraction experiment measurements only provide limited information about the amorphous structure. Thus, computer simulation is considered to be one possible way to obtain structural information of amorphous material and to predict their physical properties. Since most features of amorphous materials depend on their topology, the creation of experimentally and theoretically credible models is the starting point of any study on such materials.

The idea of creating "Materials by Design" means that materials might be designed to satisfy selected *priori* conditions. Based on whether or not the experimental information is included, the modeling strategies could be divided into two categories: direct modeling and biased modeling. Once the appropriate models are generated, the properties of such material could readily be studied through various analysis methods. In this chapter, I will first review different modeling techniques applied when generating glass models: for direct modeling, I will mainly focus on the *ab-initio* Molecular Dynamic method. Based on this method, I will introduce "melt-and-quench", computer alchemy and building block techniques. For biased modeling, I will mainly discuss the application of Reverse Monte Carlo (RMC) method and the Invariant Environment Refinement Technique (INVERT). More discussions on direct and biased modeling could be found in Ref. [3, 4]. In the second part of this chapter, the most frequently used analysis methods, both for structure and electronic properties, are reviewed.

1.1 Modeling techniques

1.1.1 Direct Modeling

As mentioned above, the first modeling category is direct modeling, which requires no experimental input. To directly simulate the interaction between atoms and calculate the total energy and forces of a system, an appropriate interatomic potential is needed. Classical empirical potentials, tight-binding technique and *ab-initio* modeling are three typical methods used in direct modeling. Starting in the 1950's, a limited number of classical empirical potentials were proposed to simulate the interaction and forces between atoms. These potentials are usually initialized by first guessing a functional form with controllable parameters. By fitting the known properties of a material, such as bond-length, bond-angle and lattice constant, the potential will be corrected through adjusting those controllable parameters. Before applying to real simulation, those empirical potentials need to be carefully tested. The tight-binding technique is based on the idea that a linear combination of atomic orbitals could be used to describe the electronic eigenstates. Under this representation, an empirical tight-binding Hamiltonian could be formed. The complexity of TB modeling is between classical potentials and *ab-initio* modeling. Several review papers for TB method applied in disorder system may be found in Ref. [5, 6]. The *ab-initio* modeling is a more accurate method which originates from the fundamental view of electronic structure of materials. In the following discussion, I will introduce the basic concept in *ab-initio* method and discuss different modeling techniques based on *ab-initio* Molecular Dynamic (*ab*-MD) simulation. The following equations 1.1-1.8 and more detailed discussion of density functional theory could be found in Ref. [7].

Ab-initio modeling, or first principle calculation, is often based on the density functional theory (DFT). Due to the huge number of electrons, it is impossible to directly

solve the many body Hamiltonian and obtain the many-particle wavefunctions of solids. Alternatively, by using electronic charge density rather than many-particle wavefunctions as variables, the DFT provides a way to convert many-body problem to a complex, effective single electron problem. Kohn, Hohenberg and Sham successfully developed the DFT and make it applicable to solid state physics [8, 9].

The formulation of DFT based on two Hohenerg-Kohn theorems[8]. The first Hohenerg-Kohn theorem proves that the ground state electron density $n(\mathbf{r})$ determines all properties of the system, such as the external potential, the total energy, wavefunctions for all states, except for a constant shift of energy. The second theorem indicates that there is a universal functional for total energy in terms of the electron charge density, $E[n]$, which will be globally minimized by the ground state electron density. Based on these two theorems, we could write[7]:

$$E[n] = F[n] + \int d^3 r V_{ext}(\mathbf{r}) n(\mathbf{r}) \tag{1.1}$$

$V_{ext}(\mathbf{r})$ is the external potential. Functional $F[n]$ contains all internal energies of the interacting electron gas. Though the electron density is the key to everything, no one has found out a way to accurately obtain any properties directly from the density. In 1965, by introducing "Kohn-Sham" orbitals, the interacting many-particle system was treated with a non-interacting auxiliary system. According to Kohn-Sham approach[9], the charge density $n(\mathbf{r})$, kinetic energy T_s, and Hartree energy (the classical electrostatic interaction) $E_{Hartree}[n]$, of an independent-particle system with single-electron wave function representation are expressed as

$$n(\mathbf{r}) = 2 \sum_{i,occ} |\psi_i|^2 \tag{1.2}$$

$$T_s = -\frac{\hbar^2}{2m} \sum_{i,occ} \langle \psi_i | \nabla^2 | \psi_i \rangle \tag{1.3}$$

$$E_{Hartree}[n] = \frac{1}{2} \int d^3r d^3r' \frac{n(\mathbf{r})n(\mathbf{r}')}{|\mathbf{r} - \mathbf{r}'|} \tag{1.4}$$

Thus, the Hohenberg-Kohn expression will be re-written as

$$E[n] = T_s[n] + \int d^3r V_{ext}(\mathbf{r})n(\mathbf{r}) + E_{Hartree}[n] + E_{xc}[n] \tag{1.5}$$

The first three terms: T_s, $\int d^3r V_{ext}(\mathbf{r})n(\mathbf{r})$ and $E_{Hartree}[n]$ reflect the contribution of a non-interacting many-particle system. The last term $E_{xc}[n]$ contains all non-classical interaction of the many-body system. By applying variational principle, we obtain the Kohn-Sham equation,

$$H_{KS}(\mathbf{r}) |\psi_i\rangle = \epsilon_i |\psi_i\rangle \tag{1.6}$$

with

$$H_{KS}(\mathbf{r}) = -\frac{\hbar^2}{2m} \nabla^2 + V_{KS,eff}(\mathbf{r}) \tag{1.7}$$

$V_{KS,eff}(\mathbf{r})$ is the effective potential depend on electron density $n(\mathbf{r})$, with the form

$$V_{KS,eff} = V_{ext}(\mathbf{r}) + \frac{\delta E_{Hartree}}{\delta n(\mathbf{r})} + \frac{\delta E_{xc}}{\delta n(\mathbf{r})} = V_{ext}(\mathbf{r}) + V_{Hartree}(\mathbf{r}) + V_{xc}(\mathbf{r}) \tag{1.8}$$

There are different approximate functionals to describe the exchange-correlation potential, such as local density approximation (LDA), generalized-gradient approximations (GGAs) and Hybrid functionals[7]. If the approximate form of $V_{xc}(\mathbf{r})$ is determined, then the true ground state density and energy could be obtained by solving Kohn-Sham eigenvalue problem. In real calculation, the Kohn-Sham equation is solved self-consistently. With the initial guess of electron density, the effective potential is

calculated and the Hamiltonian is determined. After solving Kohn-Sham equation, the new electron density will be obtained from electron eigenstates. The new density will be used as input for a new iteration, until the electron density is converged.

In this dissertation, *ab-initio* Molecular Dynamics (*ab*-MD, [3]) is used as a major tool in all direct modeling project. When such schemes are applied, with appropriate pseudopotential, the internal force and velocity of atoms in a system will be calculated. Through Newton's second law, the coordinates of atoms at any given time will be determined. By controlling the temperature (means atomic kinetic energy), the system will be annealed or relaxed to seek suitable local energy minima, representation of the amorphous phase. The final model will be the one with a minimum total energy.

One of the most popular techniques using *ab*-MD is called the "melt-and-quench" method. The MD simulation is first performed at a temperature well above melting point which forces the system to lose memory of the initial configuration and represent the liquid state. Then the system is brought to a lower temperature, with an appropriate quench rate. Finally, the system is rapidly quenched to 0K and relaxed to an energy minimum. The advantage of "melt-and-quench" method is that one can use any initial configuration as starting point. The bad news is that this method is time-consuming, especially for big systems. The final model may contain an exaggerated concentration of defects, such as wrong bonds, over- and under- coordinated atoms. However, since the "melt-and-quench" method is unbiased and very simple, it could be universally applied to model any amorphous materials, especially for materials that little is known for their structure. In this dissertation, "melt-and-quench" is used as one of the basic modeling techniques throughout the study on a-InN (Chapter 2), a-GaN (Chapter 3) and phase-change memory materials (Chapter 4).

Some elements in the periodic table, usually in the same group, form similar structures (like Si and Ge, all forming tetrahedral structures in their amorphous phase). In

this case, an initial model could be made based on previously generated models by replacing the old species with new ones and rescaling the cell to fit mass density requirement of new materials and allowing for relaxation effect. For example, a-GaN could be generated by replacing As with N atoms in a-GaAs model. This method may be called *Computer Alchemy*. Then, the initial model will be annealed at high temperature, allowing the system to find energy minima. A reasonable initial configuration will definitely reduce the simulation time, so this method is quite efficient, especially when modeling large systems. In this dissertation, 250-atom models of a-InN and a-GaN are generated by computer alchemy technique. The modeling details could be found in Chapter 2 and Chapter 3.

For some glasses, there are fundamental units, "building blocks" (BBs), that exist in both the liquid and glassy phases. If one can first generate energetically reasonable building blocks, the final amorphous models could be obtained by assembling those BBs [3, 10, 11]. This method is called Building Block modeling which actually provides a short path to generate atomistic models for complex stoichiometries, especially useful for building large models. I will systematically discuss the BB modeling technique and apply it to build *ab-initio* models of g-$Ge_2As_4Se_4$ and g-$AsGe_{0.8}Se_{0.8}$ (Chapter 5).

To sum up, the *ab-initio* MD method is an unbiased modeling technique and it usually produces reliable models. However, it often requires a long simulation time and is extremely time-consuming for large systems. Moreover, the short simulated time scale (picoseconds), compared with real experiment, might give rise to properties which contradict experimental observations.

In this dissertation, most *ab-initio* MD calculations are carried out by using periodic boundary conditions with the Vienna Ab-initio Simulation Package (VASP). VASP is based on density functional theory using a plane wave basis [12]. The model preparation and simulation details are mentioned in each chapter.

1.1.2 Biased Modeling

The other category of modeling schemes is called information based modeling, or biased modeling, which involves the prior information such as experimental requirement in the model. The Reverse Monte Carlo (RMC) method and Invariant Environment Refinement Technique (INVERT) are typical biased modeling schemes. When such methods are used, there is often a cost function (or objective function) which quantifies the difference between a certain property of current model and the same property provided by experiment. For example, in constrained RMC modeling, the cost function could be expressed as

$$\xi = \sum_{j=1}^{K} \sum_{i=1}^{M_k} \eta_i^j \{F_E^j(Q_i) - F_c^j(Q_i)\}^2 + \sum_{l=1}^{L} \lambda_l P_l \tag{1.9}$$

This expression of cost function is from Ref. [4]. The cost function $\xi(Q, \eta; \lambda, P)$ depends on η (associated with the weight factor and uncertainty of experiment), generalized variable Q which associates with some properties $F(Q)$ ($F_E(Q)$ is the experimentally measured value and $F_c(Q)$ is theoretically calculated value) and constraint functions λP where λ and P respectively represents the weight factor and penalty functions. The "add-on" penalty functions allows one to add extra constraints such as bond angle. Moreover, K stands for the number of experiment data sets, M_k indicates the total data points in kth experiment. Thus, the modeling process is actually an optimization of objective function and the final model will be one satisfying both the data and the constraints. Most biased modeling is iterative. At each iteration, the effect of the new update on configuration will be evaluated. This will be repeated until the cost function is minimized/maximized and satisfies some stopping criteria.

The problem with the traditional RMC method is that the final model obtained by minimizing/maximizing cost function is not unique. Some models may have unphysical

structures contradicting chemical common sense. To improve the RMC method, Cliffe, Dove, Drabold and Goodwin have proposed a new method, called the "Invariant Environment Refinement Technique" (INVERT), which improved the topological and chemical order of a-Si, C_{60}, and a-SiO_2 [13]. The core concept contained in INVERT+RMC method is the idea of structural uniformity: each distinct site is required to have an identical local environment to the maximum degree possible [14]. In Chapter 6, the INVERT+RMC method is further developed and applied to model glassy GeO_2, by jointly fitting partial pair-correlation functions rather than the total correlation function as in previous calculations. Then the technique was applied to model low density amorphous ice (a-H_2O), for which the uniformity is imposed on the medium range order. For these two cases, I found that imposing spatial uniformity may significantly improve the atomistic model, and the RMC+INVERT method is shown to offer significant advantage over the conventional RMC technique for particular systems.

Therefore, the biased modeling has the advantage to generate experimental credible models and it is very efficient to model large systems in some cases. However, it depends on the availability of experimental data and constraints added in the cost function. The final model may contain unphysical features which cannot be completely ruled out.

1.2 Structure and Electronic Structure Analysis

1.2.1 Structure Analysis Methods

The structure characters could be analyzed through a set of distribution functions and structure, or building block, statistics.

1.2.1.1 Pair Correlation Function

The most popular and simple position distribution function is pair correlation function. Centered upon one atom, this function represents the probability of finding

another atom at some position $\vec{r}$. Some of the discussion and equations in this section could be found in Ref. [10]. The pair correlation function can be written as:

$$g(\vec{r}) = \rho^{-2} V^{-1} N(N-1) < \delta(\vec{r} - \vec{r_{ij}}) > \tag{1.10}$$

ρ is the density of the model, V is the volume of the model. r_{ij} is the distance between the two atoms. $< ... >$ means "take the average over all configurations". If all ions are treated as point particles, then

$$g(\vec{r}) = \frac{N(N-1)}{\rho^2 V} \frac{1}{N(N-1)} \sum_{i,i\neq j} \delta(\vec{r} - \vec{r_{ij}}) \quad = \rho^{-2} V^{-1} \sum_{i,i\neq j} \delta(\vec{r} - \vec{r_{ij}}) \tag{1.11}$$

We could apply angular average to $g(\vec{r})$ and extract the radial pair correlation function $g(r)$,

$$g(r) = \int \frac{d\Omega}{4\pi} g(\vec{r}) = \rho^{-2} V^{-1} \sum_{i,i\neq j} \iint \frac{\sin\theta}{4\pi} d\theta d\varphi \frac{1}{r^2 \sin\theta} \delta(r - r_{ij}) \delta(\theta - \theta_{ij}) \delta(\varphi - \varphi_{ij}) \tag{1.12}$$

finally,

$$g(r) = \rho^{-2} (4\pi)^{-1} V^{-1} r^{-2} \sum_{i,i\neq j} \delta(r - r_{ij}) \tag{1.13}$$

For amorphous material, the radial pair correlation functions contain important local structural information. The peaks appearing in $g(r)$ describe the average distance of atom pairs and for large distance $g(r) \to 1$. It is sensitive only to pair correlations and is a highly uncomplete measure of disorder.

1.2.1.2 Structure Statistics

It is often informative to quantify specific units (such as coordination) or building blocks (such as tetrahedral structures, rings) in a specific model. In these cases the

component statistic will be applied. Usually, the results are tabled for comparison. one important statistic is the mean coordination which quantifies the average local environment for each atom.

In principle, the component statistics is a descriptive tool and evaluation method for realistic models.

1.2.2 Electronic Structure Analysis

Many applications of amorphous semiconductors are associated with their electronic structure. The electronic structure is often analyzed through electronic density of states (EDOS). The EDOS could be expressed as the sum of a set of δ functions over all eigenvalue E_i,

$$g(E) = \frac{1}{N} \sum_{i=1}^{Nbasis} \delta(E - E_i) \tag{1.14}$$

One important electronic property revealed by the EDOS is the electronic gap. The electronic gap is associated with electronic conductivity and plays an essential role for electronic properties in most cases.

For amorphous materials and glasses, it is always important and necessary to associate the irregularities/defects in topology with local features in the density of states. One possible way to quantify the localization is the measurement of inverse participation ration (IPR). Considering a system with N atoms, the IPR – $I(E)$, of a specific state with energy E is defined as

$$I(E) = N \sum_{i} Q(i, E)^2 \tag{1.15}$$

$Q(i, E)$ represents the charge localized on atom site i. In principle, IPR describes the extent of localization of a specific energy state. If the state is uniformly distributed, $I(E) = 1/N$. Otherwise, if the state is highly localized, $I(E) \to 1$. Moreover, by

comparing the contributions of different atoms on the same state, one could find out the key structure which could significantly affect the electronic structure. For example, in a-Si, IPR analysis and eigenvector projection showed that the tail states of EDOS are strongly associated with short bonds and long bonds "structural filaments" [15, 16].

1.3 Dissertation Outline

In the following part of this dissertation, I will show the research work on eight different amorphous materials including a-InN (Chapter 2), a-GaN (Chapter 3), Ge-Sb-Te (Chapter 4), g-$Ge_2As_4Se_4$ and g-$AsGe_{0.8}Se_{0.8}$ (Chapter 5), a-GeO_2 and a-H_2O (Chapter 6) and B or P doped a-Si and a-Si:H (Appendix A). In each chapter, the model preparation and analysis details will be discussed. The dissertation consists primarily of papers that I wrote, in call cases, with co-authors.

The following work in Chapter 2 is published as

B. Cai and D. A. Drabold, Physical Review B **79**, 195204 (2009).

2 Chapter: *Ab-initio* Models of Amorphous InN

2.1 Background

A material of considerable current interest is the narrow gap semiconductor InN. Since GaN is an established wide-gap material, it is appealing to consider InGaN alloys for photovoltaic and other applications. Studies in this direction [17, 18] would benefit from basic information about a-InN. These materials might possess a continuously variable range of optical gaps to optimize absorption of the solar spectrum [19].

There has been controversy over the band gap of zincblende crystalline-InN (c-InN) both in experimental and theoretical work. In experiment, a narrow band gap of 0.7 eV [20, 21] was reported, which contrasts with previous values near 1.89eV [22]. Subsequently, these small gaps have been confirmed by additional experiments [23–25]. In theoretical work, calculations based upon density functional theory within the Local Density Approximation (LDA) always yield a tiny or even negative gap [26]. Methods using self-interaction and relaxation corrected pseudopotentials (SIRC) report a large gap around 1.3 eV [27]; but semi-empirical LDA methods show a gap around 0.85 eV [28]. For amorphous InN (a-InN), a large optical gap around 1.7eV was measured in 2006 [29]. However, no further experiments have been performed. No theoretical work has appeared on a-InN.

In this paper, I present atomic models of amorphous InN obtained from *ab-initio* molecular dynamics based on plane wave LDA. The structural, dynamical, and electronic properties are discussed. To my knowledge, there is neither theoretical or experimental work on structural properties or vibrational modes. After creating small but reasonable models of a-InN, I *predict* the vibrational spectrum and electronic properties. I particularly seek to connect the electronic structure to the topology of the network to better comprehend electronic and optical experiments. I demonstrate by direct calculation

that the topology of a-InN is a chemically ordered continuous random network very much along the lines proposed by Mousseau and Barkema [30].

2.2 Model Preparation

The simulations presented in this work are performed with the Vienna Ab-initio Simulation Package (VASP), based on Density Functional Theory within the local density approximation (LDA) and Vanderbilt's ultrasoft pseudopotentials [12, 31, 32].

To construct a realistic a-InN model, I began with the quench from the melt technique for a 64-atom model [3]. The initial configuration was melted at 2000 K and equilibrated for 800 steps. Then, the system is quenched to $400K$, with a mean quench rate $61K/ps$. The system initially possesses a nitrogen dimer. According to Mott's $8-N$ rule and the electronegativity of these two elements, in theory,it is unlikely to form homopolar bond. Thus, I artificially moved this pair apart, then re-equilibrated the system at $400K$ for 1000 steps ($2.5ps$). Then the 64-atom a-InN model was relaxed to an energy minimum. During the MD procedure, the volume of the cell was constant. During the final relaxation, I allowed the volume and shape of the cell to change to ensure a zero-pressure model with no artificially imposed symmetries imposed on the shape of the cell. To check the small model, a 250-atom model was formed by relaxing an a-GaAs model [30] with Ga and As atoms replaced by In and N atoms, respectively. I rescaled the cell to reproduce the density of c-InN (also the density for 64-atom model) and relaxed the system at constant volume.

2.3 Topology Analysis

I present the topology of 64-model in Fig. 2.1. Because the shape of the cell is allowed to change during relaxation, the final cell is not quite cubic, but nearly so. The density of the final model is $6.97g/cm^3$ which is modestly larger then $6.81 \pm (0.05)g/cm^3$,the density of c-InN. Where coordination is concerned, I note that all

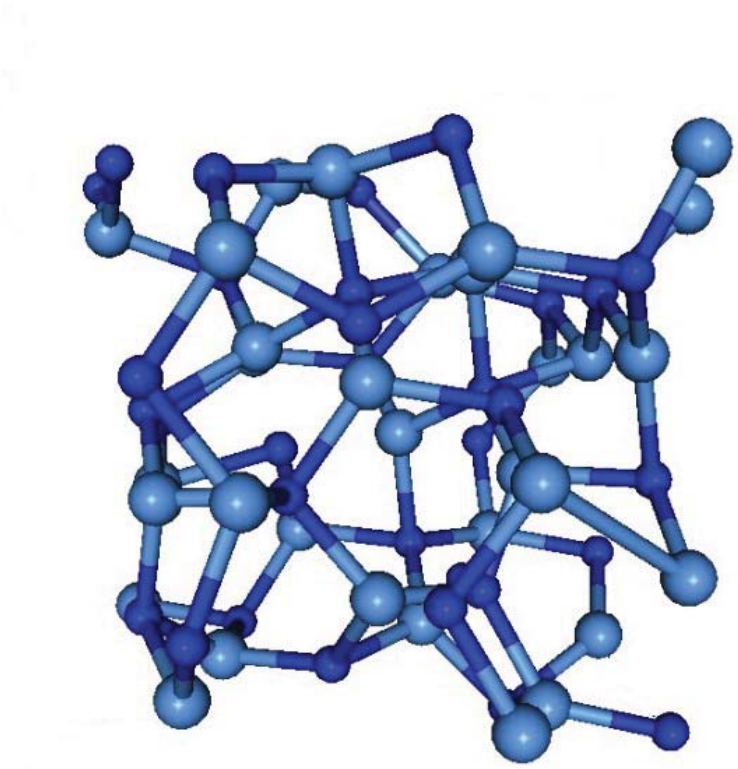

Figure 2.1: (Color online) The structure of 64 atom model of a-InN. The blue (small sphere) represents Nitrogen, and the grey (larger sphere) represents Indium.

N atoms are fourfold and all but two In atoms are fourfold. There are no "wrong" (homopolar) bonds such as N-N or In-In in the model. It is gratifying to see chemical order emerge so unambiguously from an unbiased melt-quench procedure, a strong indication that homopolar bonds are rare in the material. For comparison, in the 250-atom model, I found that 87% N atoms are four-fold, 9% are three-fold and less than 4% are five-fold. Similarly, for In atoms, 88% are four-fold, 8% are three-fold and 4% are five fold. Also there is one N-N bond in the 250-atom model, which could probably be eliminated if desired using the approach I employed for the 64-atom model. I summarize the results for the topology in Table 2.1. The little increase in the under and over coordinated atoms in 250-atom cell could be attributed to the fact that the model is energetically relaxed while 64-atom cell is obtained through melt-quench technique, so the miss-coordination could be just an artifact of the relaxation technique used. However, the apparent difference in coordination statistics is negligible in the sense that it did not cause any considerable change in the structural and electronic properties compared to the smaller 64-atom cell. Thus, I conclude that the 64-atom model and 250-atom model are consistent with each other.

Table 2.1: The statistical distribution of the main structural components in 64- and 250-atom models.

Model	N_3	N_4	N_5	In_2	In_3	In_4	In_5	n_N	n_{In}
64-atom	0	32(100%)	0	0	1(3.1%)	30(93.8%)	1(3.1%)	4	4
250-atom	11(8.8%)	109(87.2%)	5(4%)	1(0.8%)	10(8%)	110(88%)	4(3.2%)	3.95	3.94

I plot the pair-correlation functions of both models in Fig. 2.2. For 250 model, the small peak under $2\mathring{A}$ appearing in N-N plot is due to the homopolar bond mentioned before. For 64-model, the small peak and shoulder in N-N and In-In plot around $3\mathring{A}$ is due to the size effect. Besides that, the partial pair correlation functions of both models are

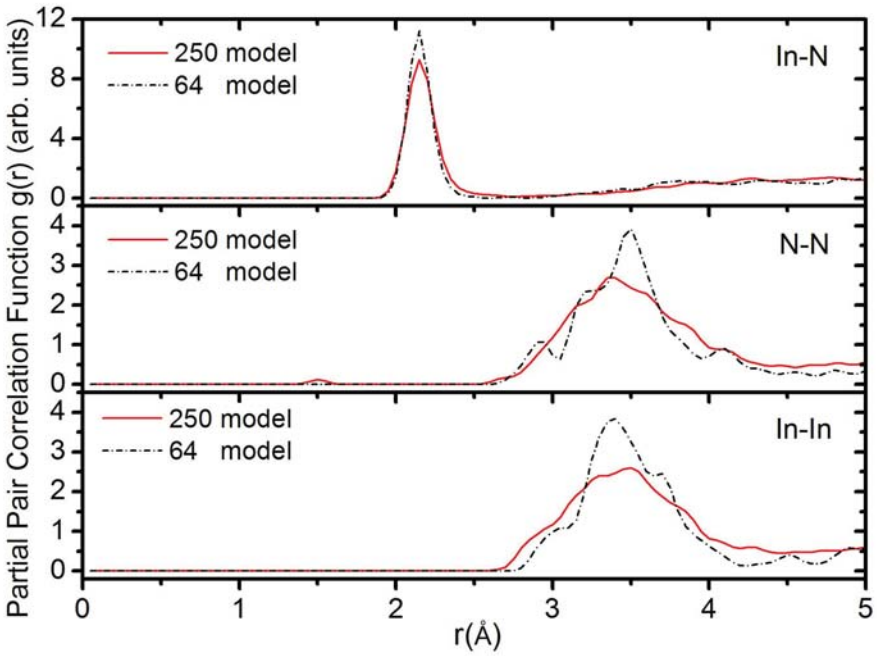

Figure 2.2: (Color online) Partial pair correlation functions of a-InN of 64-model (dashed line) and 250-model (solid line). From top to bottom,In-N,N-N,In-In.

quite similar. There is a sharply defined peak at 2.15$\mathring{A}$ for In-N. However, for N-N and In-In, the peak is broader, and centered near 3.5$\mathring{A}$ and 3.4$\mathring{A}$. Thus, the In-N pairs provide the dominant contribution to the first peak of total pair correlation function. The N-N and In-In pairs provide the second peak of total pair correlation function. To my knowledge, no experimental data is available, so this work is actually a *prediction*.

I also analyzed the angle distribution for In-N-In bonds and N-In-N bonds. The In-N-In angle has a mean value of 109.12^o, which is close to the tetrahedral angle 109.47^o. The angle distribution shows the FWHM is around 28^o. The mean value of N-In-N bond angle is 108.78^o, but the distribution is broader, with a FWHM around 34^o. This result shows that Nitrogen and Indium atoms form tetrahedral units. However, there are some unexpected angles in the sample. I present the ring statistic result in Table 2.2. From the table, I notice that there are no odd-membered rings in the network, and this merely reiterates the absence of homopolar bonds. However, there are a few four-member rings. The existence of four-member rings implies that there are edge-sharing tetrahedra and other special units in the model which do not exist in c-InN. The situation is somewhat analogous to the case of a-SiO_2 [33], where the O-Si-O angles are tightly constrained near θ_T and the Si-O-Si angles have a broader distribution. I also computed the ring statistics in the 250-atom model. The results are also listed in Table 2.2. Thus, from all of the data, I can conclude that 250-atom model has basically similar properties with 64 atom models. It is to be admitted that the 250 atom is probably superior, since strain effects are certain to be smaller in the larger supercell.

Table 2.2: Ring statistics of a-InN. The number of n-member rings, n=3 through n=7.

$Ring-Size$	n_3	n_4	n_5	n_6	n_7
64-atom	0	30	0	320	0
250-atom	0	140	0	628	8

2.4 Vibrational Properties

I describe the vibrational properties by analyzing the vibrational density of states (VDOS). In experiment, the VDOS can be obtained through inelastic neutron scattering, and information about the VDOS (modulated by hard-to-compute matrix elements) can be inferred from Raman measurements. In simulation, the vibrational energies are obtained from the dynamical matrix (matrix of the second derivatives of the energy with respect to the atomic positions). In VASP, the dynamical matrix (Hessian Matrix) is determined by displacing each atom 0.015Å in three orthogonal directions. This yields the force-constant matrix, from which the dynamical matrix is easily obtained [34]. Then the vibrational eigenvalues (the vibrational frequencies) are obtained by diagonalization. The density of states is obtained by Gaussian broadening of the eigenvalues. Fig. 2.3 shows the vibrational state density of 64-atom model. There are two bands in VDOS. The lower (acoustic) band goes up to $240cm^{-1}$ with two major peaks at $112cm^{-1}$, $207cm^{-1}$. The higher-energy (optical) band is between $300cm^{-1}$ to $690cm^{-1}$.

2.5 Electronic Structure

The electronic properties of the models are analyzed through the electronic density of states (EDOS) and inverse participation ratio (IPR). The EDOS are projected onto different atomic species and orbitals. I plot the detailed gap structure for both 64- and 250-atom models in Fig. 2.4 and Fig. 2.5. I found for both models that N atoms contribute more to valence tail but less to conduction tail relative to In. Secondly, the projections into s, p and d channels shows that the valence tail states are mostly associated with p electrons and the d electrons offer a larger contribution to the conduction band tail. The importance of the projection into the d-subspace emphasizes the need to include valence d states or polarization orbitals in a local orbital representation.

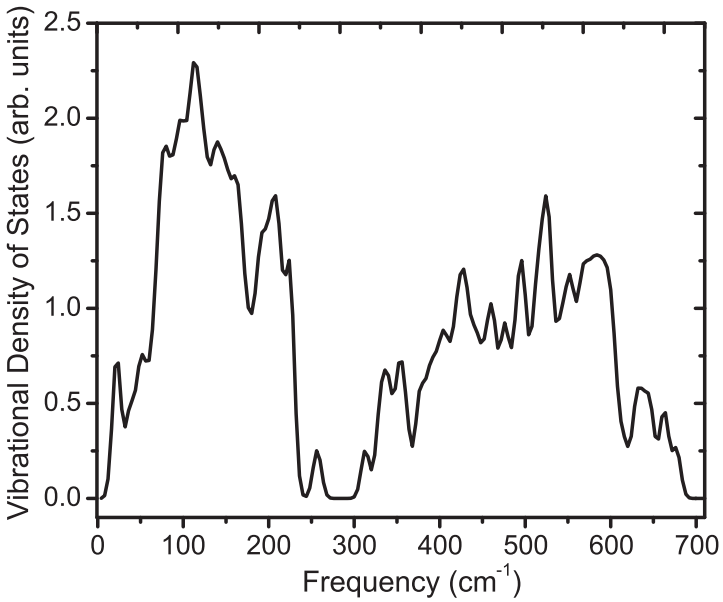

Figure 2.3: Vibrational density of states of 64-atom model of amorphous InN. The vibrational eigenvalues were Gaussian broadened with a width of $7cm^{-1}$

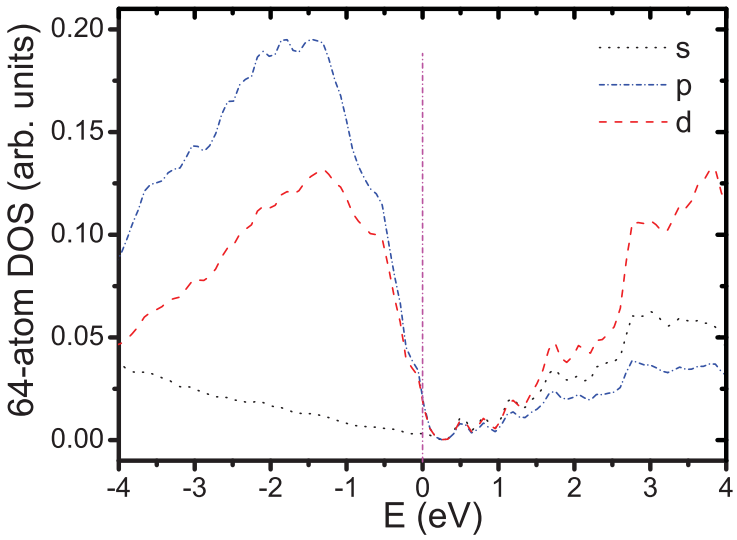

Figure 2.4: (Color online) Density of electron states around Fermi Level of 64-atom models. 32 **k** points were used. Vertical line indicates the position of Fermi level, ϵ_F.

For the 64-atom model, I found that the shape of the DOS converges when more than 30 special **k** points are considered [35]. By considering only the Γ point, it appears that there is a small gap separating the valence and conduction bands. To correctly determine the position of ϵ_F and to ensure the convergence of the density of states, I repeated the analysis with various numbers of **k** points. ϵ_F shifts to the very top of the valence tail when sufficient **k** points are included. The results for 32 **k** points and 108 **k** points almost coincide, suggesting that DOS calculation is adequate for 32 points. For the 250-atom model, the calculation based only on Γ is enough to produce accurate EDOS. Similar to 64-atom model, a very small gap is observed. I accept the measured gap of $\approx 1.7eV$ [29] and suspect that the small gap largely has the same origin as the small LDA gap in c-InN, though the situation in the amorphous phase is more complex thanks to the formation of tails, especially at the conduction edge.

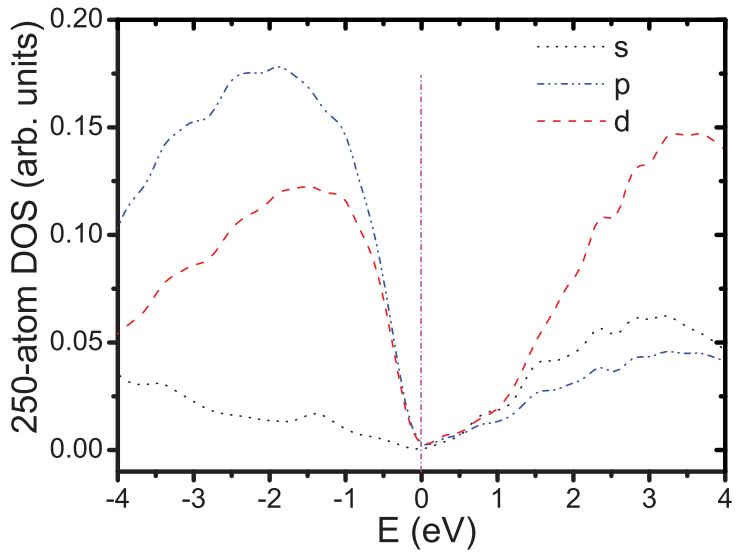

Figure 2.5: (Color online) Density of electron states around Fermi Level of 250-atom model. Only Γ was used. Vertical line indicates the position of Fermi level, ϵ_F.

Thus, I conclude that for both models that the Fermi level lies just at the top of valence tail which means there is at most a tiny gap. By carefully studying the difference between HOMO and LUMO level, I observed that the gap is smaller than 0.2eV. This is not a surprising result, since the density functional approximations underestimate the gap, and particularly so in InN in view of work on the topologically similar crystalline phases. Nevertheless, there is no reason to believe that the topology or dynamics should be critically affected by this, and furthermore, it is of interest to analyze the Kohn-Sham orbitals near the gap to gain insight into the defect states and levels.

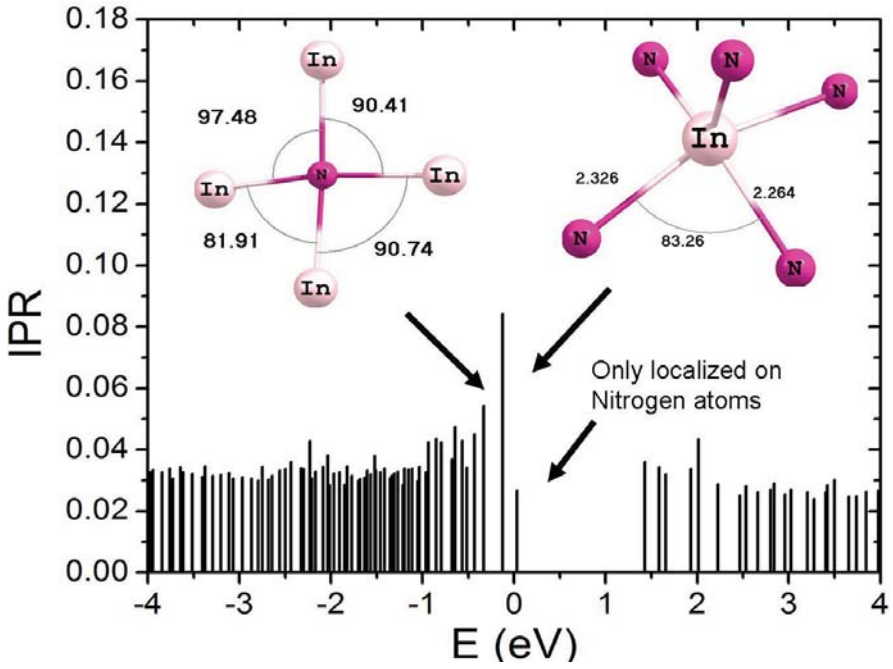

Figure 2.6: (Color online) IPR for different states near the optical gap, and special units upon which the states are localized (see text).

In Fig.2.6, I present the inverse participation ratio (IPR) plotted against energy for the 64-atom model. The IPR ($\mathcal{I} = 1$)measures how localized (spatially compact) each state is. For a uniformly extended state, $\mathcal{I} = 1 \approx 1/N$, here $N = 64$, the number should be 0.016.

For an ideally localized state, the $\mathcal{I} = 1$ value should be close to unity. From Fig.2.6, I observe that the IPR is never large, which indicates the localization of those states is not very high. However, there are some weakly localized states on the tail. The results are confirmed by IPR analysis for 250-atom model: the IPR there is commensurately small and valence and conduction band tail have a few somewhat localized states.

If I project the IPR onto different atoms, I determine the specific atoms on which a selected state is localized. I observe for the 64-atom model that one valence tail state is localized on an N atom which form four angles near 90^o. Another valence tail state is localized on two N atoms which are the fourth and fifth neighbors of the only 5-fold In atom (also with longer bond lengths larger than typical). Also the gap states are preferentially localized on N atoms, and less so onto In atoms.

Finally, to understand the electronic signature of defects in the amorphous phase, I performed the calculation on models with defects such as vacancies, anti-site defects and wrong bonds. I only consider single defect in each case. For example, for vacancy, I take one atom out of the system; for anti-site defect, I replace one N (or In) atom with In (or N) but do *not* relax the system. When single N vacancy is introduced, ϵ_F shifts toward the conduction edge and additional conduction tail states which are localized on the neighbors of that N vacancy are pushed into the gap. Similar to N vacancy, highly localized conduction band tail states are induced by the N anti-site defect. But the shift in ϵ_F is small compared with N vacancy, and toward conduction band. Since Fermi level shifts toward conduction band, these two kinds of defects make the semiconductor n-type. On the contrary, a remarkable movement of ϵ_F toward valence band tail is observed in the presence of an In vacancy. The In anti-site defect also slightly shifts ϵ_F to the valance tail. In both case, highly localized valance band tail states are observed which correspondingly associate with neighbors of In vacancies and In anti-site defect. Thus, these two kinds of

defects may make the system p-type. Finally, for N-N “wrong” bond, it produces both valence tail states and conduction states. The Fermi level is shifted into gap.

2.6 Conclusions

I have discussed the topology, vibrational dynamics and electronic structure of amorphous InN. The topology of this material is found to be tetrahedral and chemically ordered. I hope my model will provide a helpful starting point for future work.

The following work in Chapter 3 is submitted as:

B. Cai and D. A. Drabold, Physical Review B (2011).

3 Chapter: Properties of Amorphous GaN Obtained from First-principles Simulations

3.1 Introduction

With a profound impact on lighting technology and other applications, crystalline GaN bas been the subject of vast inquiry[36–38]. However, lattice mismatch with substrates makes it difficult to grow. Recently, *amorphous* GaN has become attractive due to its potential to solve the lattice match problem and its natural isotropy. A number of experiments have investigated the structural and optoelectronic properties of a-GaN[39–44]. In 1997, Stumm and Drabold proposed that a-GaN might find use as an electronic material[45, 46].

The structure of a-GaN is controversial. Some experiments observe a large concentration of homopolar bonds[47], contradicting other studies[43]. I did not observe N-N or Ga-Ga bonds in my computer models, but other calculations suggest a more disordered network[48]. Doping of a-GaN is an important topic, but a full understanding of the intrinsic electronic features of undoped a-GaN, like the origin of defect states and tail states, is a necessary precursor. Naturally, the detailed properties depend upon the mode of growth of the material; my work is most relevant to least defective “ideal” a-GaN.

It has been more than a decade since the first a-GaN model was proposed, a time during which many experiments have been carried out, and simulation tools have experienced major developments. Therefore, additional calculations have been undertaken to generate atomistic models of a-GaN and to further explore its interesting properties.

In this paper, I propose atomistic a-GaN models formed *via ab initio* molecular dynamic simulation with a plane wave basis. The network topology is analyzed through radial and angular distribution functions, and structural statistics. I find that Ga and N atoms strongly prefer to be four-fold, and homopolar bonds are rare in the network. I also

predict electronic properties and connect the electronic structure to the topology of the network. I show that the conduction edge has Urbach (exponential) form and is extraordinarily delocalized, and the valence edge is very sharp with highly localized states. Doping is briefly discussed. Vibrational properties and dielectric functions are predicted.

3.2 Models and Simulation Methods

All calculations in this work are performed with the Vienna Ab-Initio Simulation Package (VASP)[12] based on density functional theory (DFT) within the local density approximation (LDA) and Vanderbilt's ultrasoft pseudopotentials. Three models are generated via computer alchemy: a 64-atom model (obtained from a 64-atom InN model of Ref. [49]), 250-atom model I (obtained from 250-atom a-GaAs model of Ref. [30]) and 250-atom model II (obtained from 250-atom a-InN model of Ref. [49]). The 64-atom model is annealed and equilibrated at 500K and 250-atom model I is annealed and equilibrated at 300K. After zero-pressure relaxation, the density of the 64-atom model is $5.8 g/cm^3$, 95% of the crystalline GaN density; both 250-atom models have mass density around $5.6 g/cm^3$, 92% of the crystalline GaN density. The new 64-atom model shows an improved cohesive energy (lower by 0.16eV/atom) compared with the previous model[45]. Where chemical order is concerned, there are no homopolar bonds in the 64-atom model and 250-atom model I, and only one N-N bond in the 250-atom model II as one might expect for a partly ionic system. For coordination, I note that most atoms tend to be four-fold, suggesting that a-GaN retains the zinc-blende/wurtzite character of crystalline GaN, in significant contrast to the early study[45]. I list the structural properties in Table 3.1. Since the 64-atom a-GaN was made from melt-and-quench method, while the both 250-atom models are generated only by a energetic relaxation, the little increase of over- and under-coordinated atoms in both 250-atom models could be the

artifact of the relaxation technique used. This result suggests that an ideal a-GaN is a chemically ordered continuous random network.

3.3 Results and Discussions

Table 3.1: The statistical distribution of the main structural components of three models.

Model	N-N	Ga-Ga	N_3	N_4	N_5	Ga_3	Ga_4	Ga_5	n_N	n_{Ga}
64-atom	0	0	3%	97%	0	6%	91%	3%	3.97	3.97
250-atom model I	0	0	11%	87%	2%	9%	89%	1%	3.91	3.91
250-atom model II	2%	0	9%	89%	2%	11%	87%	2%	3.92	3.90

I plot the partial pair-correlation functions of the three models in Fig. 3.1. For the Ga-N partial, there exists a sharp first peak around 1.94Å for all three models. The pre-peak/shoulders in Ga-Ga partial (marked by black arrow) indicate that there exists two local environment for Ga atoms and I will show that those two Ga sites are related to edge-sharing N tetrahedral structures. Due to the N-N bond, there is a small peak around $1.53\mathring{A}$ in N-N partial of 250-atom model II (marked by black arrow). Overall, the pair correlation functions of three models exhibit similar features and they are close to the results of Ref. [46].

Next, I analyze the angle distributions for Ga-N-Ga bonds and N-Ga-N bonds. The 250-atom models yield major peak positions close to $\theta_T = 109.47°$ for both Ga-N-Ga and N-Ga-N angle. For the 64-atom model, the major peak positions are slightly off θ_T, the mean value of of N-Ga-N and Ga-N-Ga angle, being 109.15° and 108.65° respectively. Thus, I conclude that a-GaN retains strong vestiges of its crystalline short-range order and tends to form a tetrahedral structure. I observe a pre-peak around 80° for the 64-atom model (shoulders for the 250-atom model) in the Ga-N-Ga angle distribution which

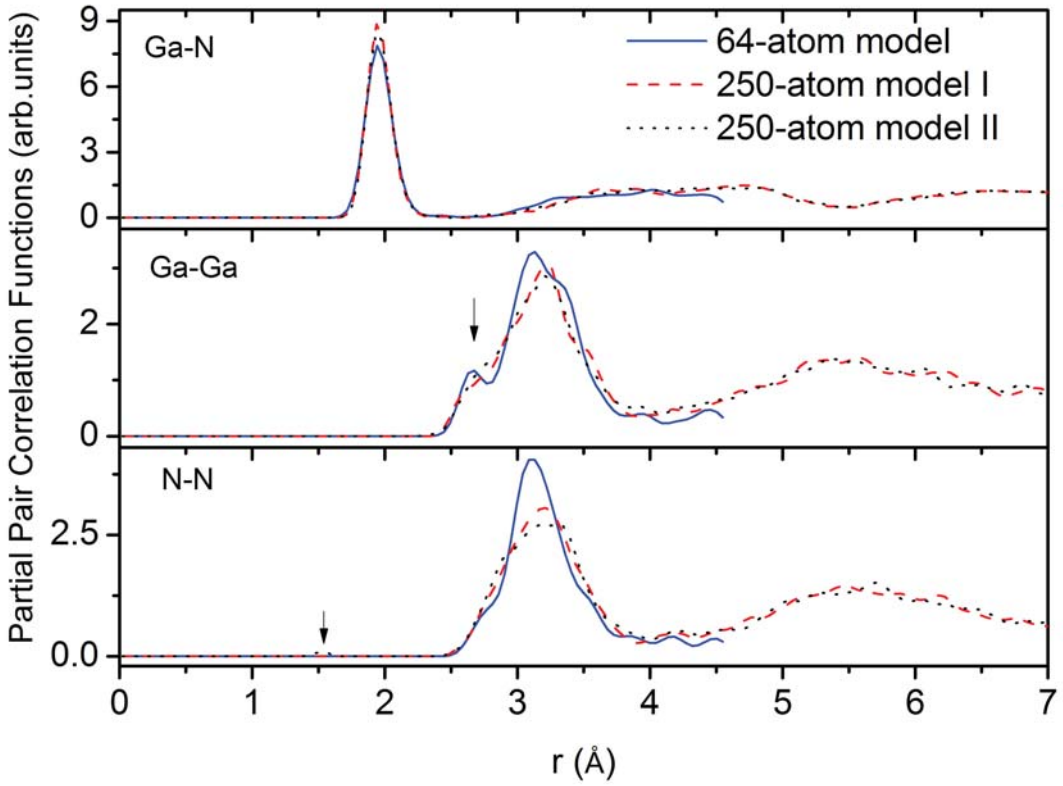

Figure 3.1: (Color online) Partial pair correlation functions of the three models (see text). In the Ga-Ga partial, the pre-peak/shoulders are marked by a black arrow. For the N-N partial, the black arrow marks the peak due to the only N-N bond in 250-atom model II.

implies that there are two distinct sites for Ga atoms. After a detailed investigation, I find that the small angle is due to edge-sharing units with distorted angles (appearing as four-member-rings with Ga-N-Ga angle between 75° and 95°). I will show that this kind of distortion is responsible for some of the electronic tail states.

The vibrational properties of a-GaN are characterized through the vibrational density of states (VDOS). Starting with a thoroughly relaxed cell, the force constant and dynamical matrix is obtained from perturbing each atom in turn by 0.015Å, and computing forces on all atoms in the model for each perturbed conformation. The VDOS

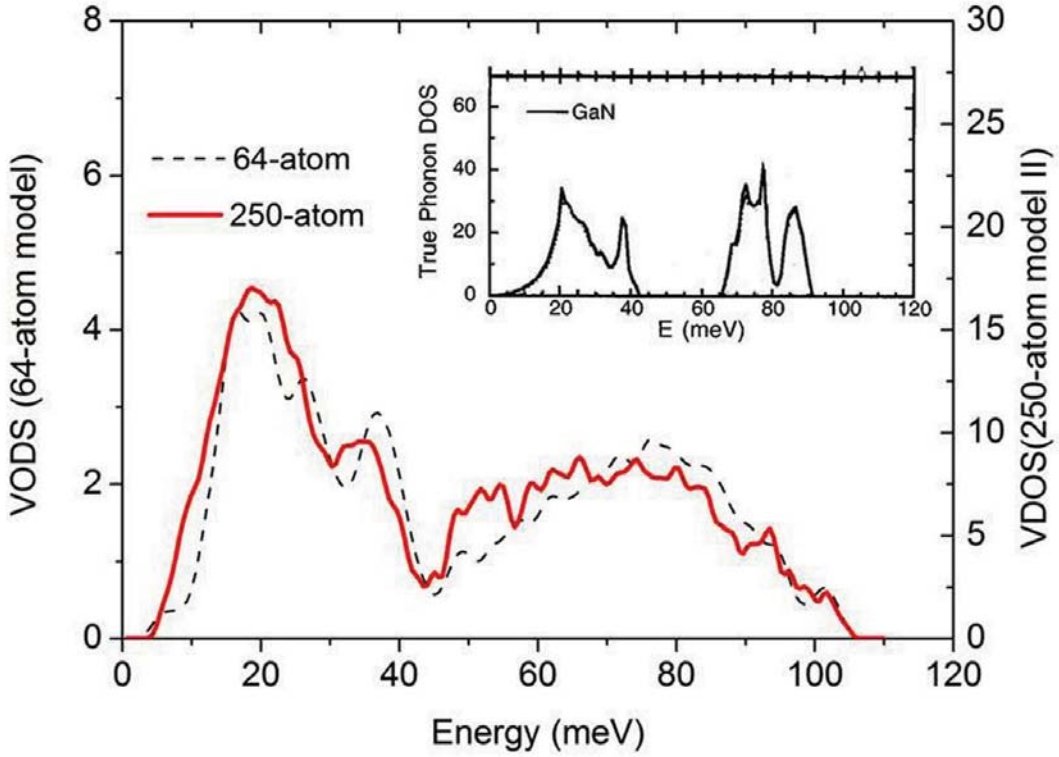

Figure 3.2: (Color online) Vibrational density of states of 64-atom model and 250-atom model II. The eigenvalues were Gaussian broadened with a width of 1meV. The VDOS of crystal wurtzite GaN is plotted as an inset from Ref. [2].

of the 64-atom model and 250-atom model II are reported in Fig. 3.2. Both models show similar features. For comparison, I also plot the VDOS of crystalline GaN from Ref. [2] as insert. My results show that the amorphous VDOS retains some features of crystal VDOS such as the two peaks in the first band. However, I did not observe two distinguished peaks in the optical band[50], and the gap between the acoustic band and the optical band fills in substantially. The results are quite consistent with a recent Raman study[43].

I describe the electronic structure by analyzing the electronic density of states (EDOS), inverse participation ratio (IPR) of the individual states, and dielectric functions.

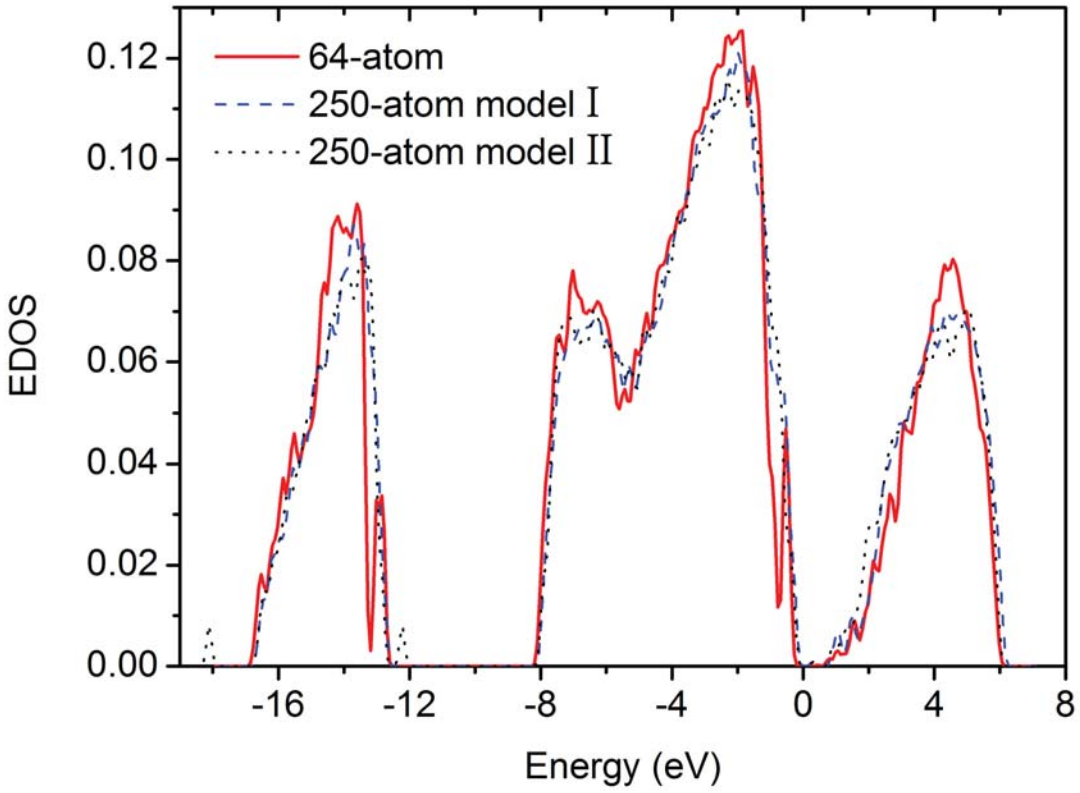

Figure 3.3: (Color online) Electronic density of states of 64-atom model(32 K-points are used), 250-atom model I(8 K-points are used) and 250-atom model II(8 K-points are used). The Fermi level is at 0 eV.

Fig.3.3 shows the EDOS of the three models. Overall, all three EDOS have similar character with slight differences in detail. The conduction band tail is *dramatically* broader than the valence band tail. If I define the band gap as the difference between highest extended energy level of states in the valence band and lowest extended energy level of states in the conduction band (excluding the mid-gap and tail states), I estimate that the band gap to be about 3.0eV for the 64-atom model and 2.3eV for the 250-atom models. I indicate this in Fig.3.4 (the region between black arrows is taken as optical band gap). The band gaps obtained from my models are smaller than the experimental value 3.1eV[42]. This is primarily due to the LDA which is well-known to underestimate the

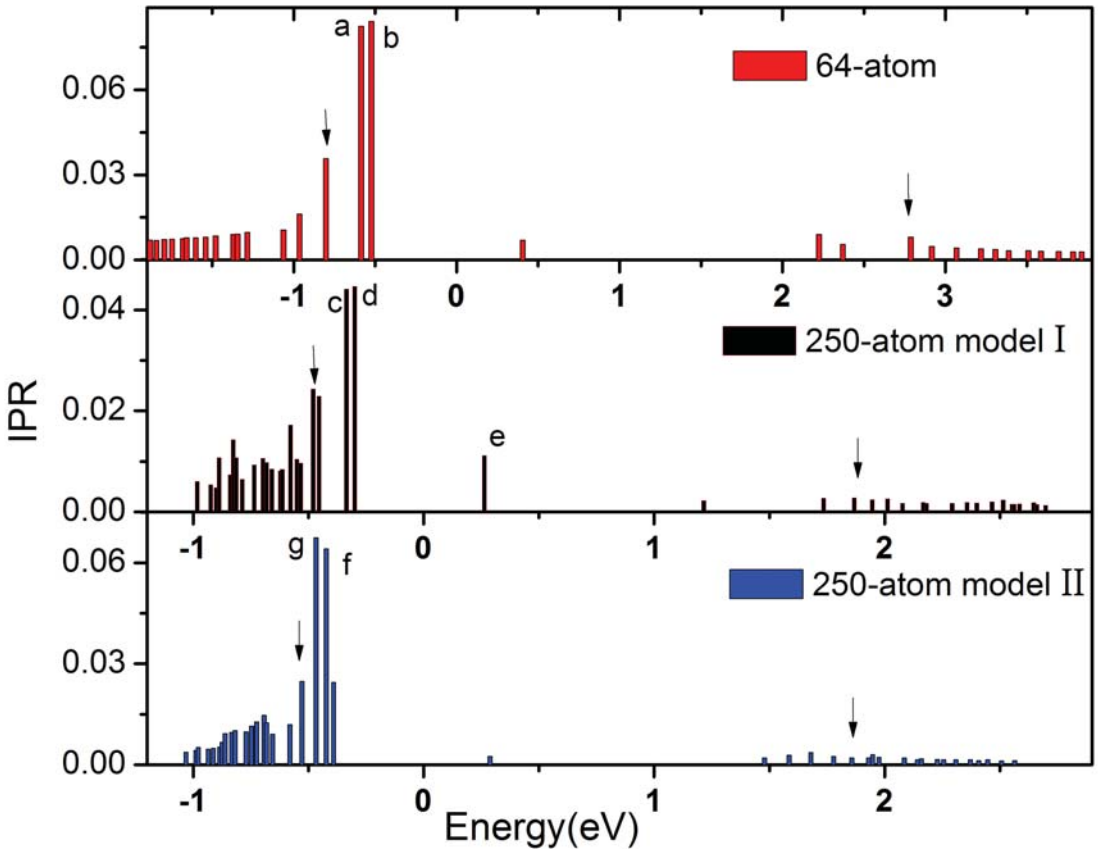

Figure 3.4: (Color online) Inverse participation ratio analysis for three models. Large IPR implies strong localization. For each model, the optical band gap are estimated by excluding the mid-gap and tail states (region between two black arrows in each plot). Note the highly delocalized conduction tail. The Fermi level is at 0eV.

band gap[51]. By fitting the conduction band tail to an exponential, I report the Urbach energy, $E_u \approx 420meV$ for the 64-atom model and $E_u \approx 490meV$ for the 250-atom model I, comparable to the reported value "several hundred meV" in Ref. [52]. In addition, for 250-atom model II, there are defect states in the deep band region between -18eV and -12eV far below the Fermi level. These defects are due primarily to the N-N bond. Other than the defect states in deep band below -8eV, I did not observe any electronic signature of N-N bond around the optical gap.

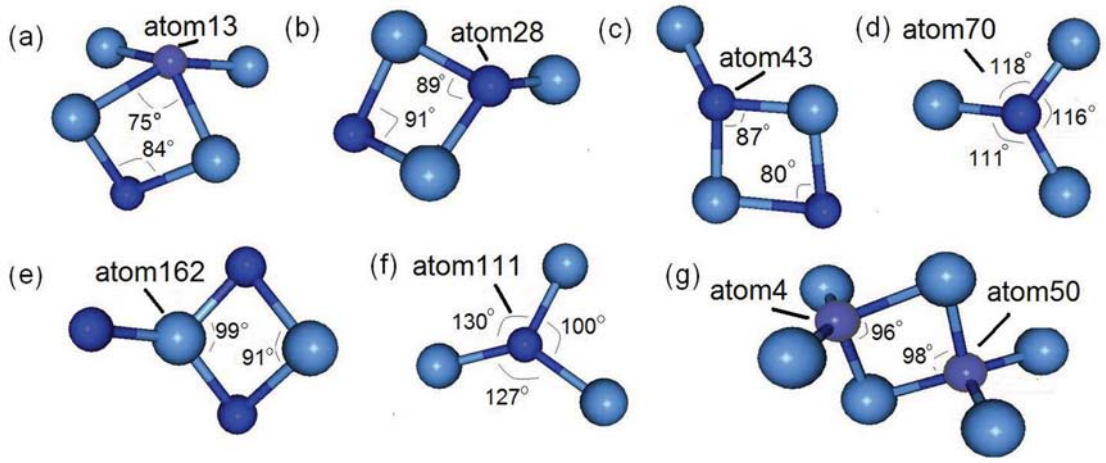

Figure 3.5: (Color online) Atomistic origin of electronic tail and gap states correlated with state *a*-*g* indicated in Fig.3.4. Dark(small) atom is N; light (large) atom is Ga. (a) atom-13 is associated with tail states *a* and *b*. (b) atom-28 is associated with tail state *b*. (c) atom-43 is associated with tail states *c* and *d*. (d) atom-70 is associated with tail state *d*. (e) atom-162 is associated with tail state *e*. (f) atom-111 is associated with tail state *f*. (g) atom-4 and atom-50 are associated with tail state *g*.

To characterize the localization of the tail states around the gap, I performed an IPR analysis for all three models. The IPR measures the degree of localization given an electronic state[53]. For highly localized states, IPR=1; for extended states, IPR=1/*N*, where *N* is the number of atoms. The results are plotted in Fig.3.4. By projecting the EDOS onto different atomic orbitals, I find that the valence tail is built from N-p, Ga-p and Ga-d orbitals. This implies a high sensitivity to bond angle disorder, which is presumably the reason for high localization. The conduction tail is localized on Ga-s and N-s orbitals. Since the s-s interaction is *only affected by bondlength*, the conduction tail states exhibit remarkably weak localization and the conduction tail is almost immune to angle disorder. This situation is somewhat similar to a-SiO_2, where there is also a large asymmetry on IPR between valence band and conduction band tails as discussed by Robertson[54, 55]. To my knowledge, this effect has not been reported in nitrides. The asymmetry in width

and localization of tail states suggests that *n* and *p* doping for a-GaN will be quite different[56]. Due to the highly localized valence-band tail states, it will be more difficult to move the Fermi level toward the valence mobility edge, complex compensations may happen and mobility is likely to be poor. Thus, the p-type doping is expected to be relatively more difficult than n-type doping to obtain the same carrier concentration[57].

To correlate electronic structure with topological units, I picked seven electronic states (*a*-*g* in Fig.3.4) with relatively high IPR and projected them onto individual atom sites. In Fig.3.5, I present the characteristic atomic sites associated with those tail states *a*-*g*. In the 64-atom model, the tail states *a* and *b* are highly localized on atom-13 (Fig.3.5(a)) whose four neighbors are almost in the same plane, with distorted Ga-N-Ga angle 75°; the state *b* is also localized on atom-28(Fig.3.5(b)), the only three-fold N atom in the network which formed a small Ga-N-Ga angle near 89°. In 250-atom model I, three-fold N atom-43 (Fig.3.5(c)), which formed a 87° Ga-N-Ga angle, is strongly associated with eigenstate *c* and *d*; the tail state *d* are also localized on atom-70 (Fig.3.5(d)), a three-fold N atom with all its neighbors almost in the same plane; moreover, the conduction-band tail state *e* is mainly localized on atom-162 (Fig.3.5(e)), a three-fold Ga atom with disordered N-Ga-N angle. In 250-atom model II, three-fold N atom-111 whose three neighbors are almost in the same plane (Fig.3.5(f)), contribute more to the valance-band tail state *f*; two four-fold N atoms, atom-4 and atom-50, formed edge-shared tetrahedron with disordered Ga-N-Ga angle, are strongly associated with electronic state *g*. Overall, atoms with distorted angle are associated with valence tail states. Finally, I briefly remark that, for the 64-atom model, the imaginary part of dielectric function $\epsilon(w)$ has a major peak position around 6.8eV for all three directions. This result is comparable to the experimental work reported in Ref. [44].

3.4 Conclusions

In conclusion, I created a-GaN atomistic models using state of the art methods. Most atoms in the network tend to be four-fold and form tetrahedral structures. I predict a 3.0eV optical band gaps for 64-atom model and 2.3eV for 250-atom model. I find an interesting and large asymmetry in localization between valence and conduction tail due to the different orbital interaction, which should yield quite distinct properties in *n* and *p* type doping. The atomistic origin of tail and defect states is discussed, and the disorder in bond angle is likely to introduce valence tail states, whereas the conduction tail is due primarily to bond length disorder. The vibrational density of states retains some qualitative features from the crystal, and the dielectric functions shows a peak around 6.8eV, both of which are in agreement with experiment. My work focuses primarily on "ideal" GaN to establish a reference model. Ion bombarded samples are indeed likely to exhibit far more disorder[47, 48].

Part of the following work in Chapter 4 is published as

B. Cai, D. A. Drabold and S. R. Elliott, Applied Physics Letters **97**, 191908 (2010).

Part of the work is submitted to:

B. Cai, B. Prasai and D. A. Drabold, Book Chapter "Atomistic simulation of flash memory materials based on chalcogenide glasses", the book under the working title "Flash Memory", ISBN 978-953-307-272-2, Intech publisher, 2011.

4 Structural Fingerprints of Electronic Change in the Phase-change Material: $Ge_2Sb_2Te_5$

4.1 Background

For Ge-Sb-Te (GST) alloys, there exists a rapid and reversible transition between crystalline and amorphous states. Controlled modification of electrical conductivity and optical properties of the transition is the basis for promising FLASH and optical memory devices. Akola and Jones [58] analyzed the structure of liquid and amorphous phases, and compared the electronic structure with the crystal phase. In 2008, Hegedus and Elliott [59] reproduced the crystal-amorphous transition by MD simulation, and they found that the rapid crystal growth was due to the presence of crystal fragments – four member square rings (so-called "seeds") in amorphous and liquid phases. Their work provided a way to track the dynamic changes of network topology and electronic structure at the same time. Welnic and co-workers [60] studied the origin of optical properties and argued that the optical contrast between amorphous and crystalline phases is due to a change in local order of Ge atoms. Despite this progress, the correlation between topology and electronic structure, most especially the origin of the change in the electronic gap, is still imperfectly understood. One of the challenges is the basic limitation of the LDA for estimating the gap.

4.2 Model Preparation

I began the work by creating amorphous $Ge_2Sb_2Te_5$ models by using the Vienna *Ab-initio* Simulation Package (VASP)– a plane-wave DFT code, using a PAW potential and the GGA-PBE method [59]. 63-atom amorphous $Ge_2Sb_2Te_5$ models with lattice constant 12.5 Å were made as follows. The system was first melted and equilibrated at 1000K, followed by a rapid quench to 500K with a quench rate of 16K/ps. Then the

Table 4.1: Mean coordinations, bond types and seeds(four member square rings) statistics at 500K. The result obtained at 1000K is listed in brackets (coordination cutoff=3.2Å).

	N_{tot}	N_{Te}	N_{Ge}	N_{Sb}
Te	3.4(3.0)	20%(30%)	47%(41%)	33%(29%)
Ge	4.6(4.3)	86%(71%)	5%(13%)	9%(16%)
Sb	4.1(3.6)	69%(62%)	11%(20%)	20%(18%)
N_{seed}	18(1.8)	52%(10%)	69%(12%)	53%(10%)

system was equilibrated for 20 ps and data collection began at 10ps. For the crystal phase, 108-atom crystal $Ge_2Sb_2Te_5$ cells with lattice constant 21.316Å are generated based on NaCl rock-salt structure with 10% vacancies: 60 Te atoms occupied the Na sites; 24 Ge atoms and 24 Sb atoms randomly occupied the Cl sites which left 10 Cl sites unoccupied. The system was then relaxed under zero-pressure until the minimum total energy was obtained.

4.3 Result and Discussions

4.3.1 Bond Statistics

The calculated atomic coordinations for a-$Ge_2Sb_2Te_5$(500K) and l-$Ge_2Sb_2Te_5$(1000K) are listed in Table 4.1 with a 3.2Å cut-off. These results are similar to [58], although in my case, the mean coordination of Ge atoms is slightly increased after thermal quench and equilibration, which may be due to the higher equilibration temperature used and/or size artifacts for the smaller model. More highly-coordinated Ge and Sb (5-fold,6-fold) atoms appeared in the amorphous phase, which suggests that a near-octahedral structure may be formed (square-rings and 8-atom cubes). These results indicate that structural ordering is enhanced in the amorphous phase relative to the liquid. Moreover, the number of wrong bonds (Te-Te,Ge-Ge,Sb-Sb and Ge-Sb) are decreased

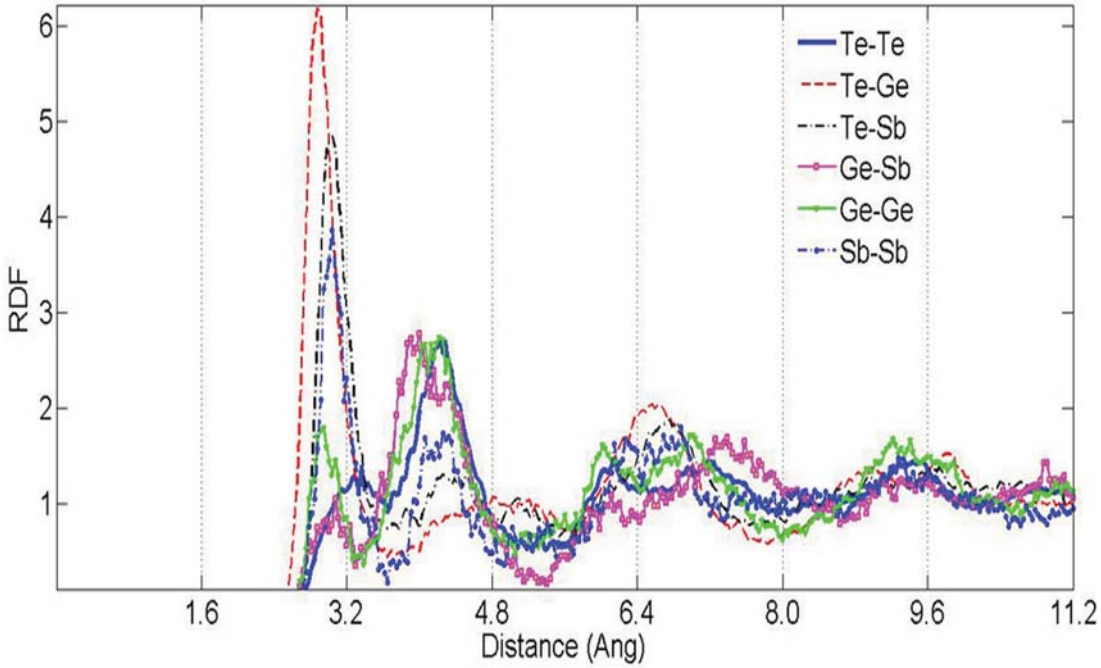

Figure 4.1: Partial radial distribution functions for a-$Ge_2Sb_2Te_5$.

from 1000K to 500K which indicates that the chemical order is also improved. The average number of "seeds" (four member square rings) shows an increase in the amorphous phase and more than 50% of the atoms are involved in "seeds", compared to only 10% in the liquid phase. The calculated partial radial distribution functions are plotted in Fig. 4.1. The first peak in the Te-Ge and Te-Sb partials are located at 2.81Å and 2.92Å. The shallow first minima imply that the coordination is sensitive to the cutoff value selected. The Te-Ge partial has a broad and weak second peak. However, the Te-Sb partial possesses a second peak with a maximum at 4.4Å which indicates that Ge and Sb atoms differ in local environment relative to Te atoms. Regarding the homopolar bonds, there is a major peak for the Sb-Sb partial centered at 2.9Å. These results are similar to other simulations [58] and also experimental results [61].

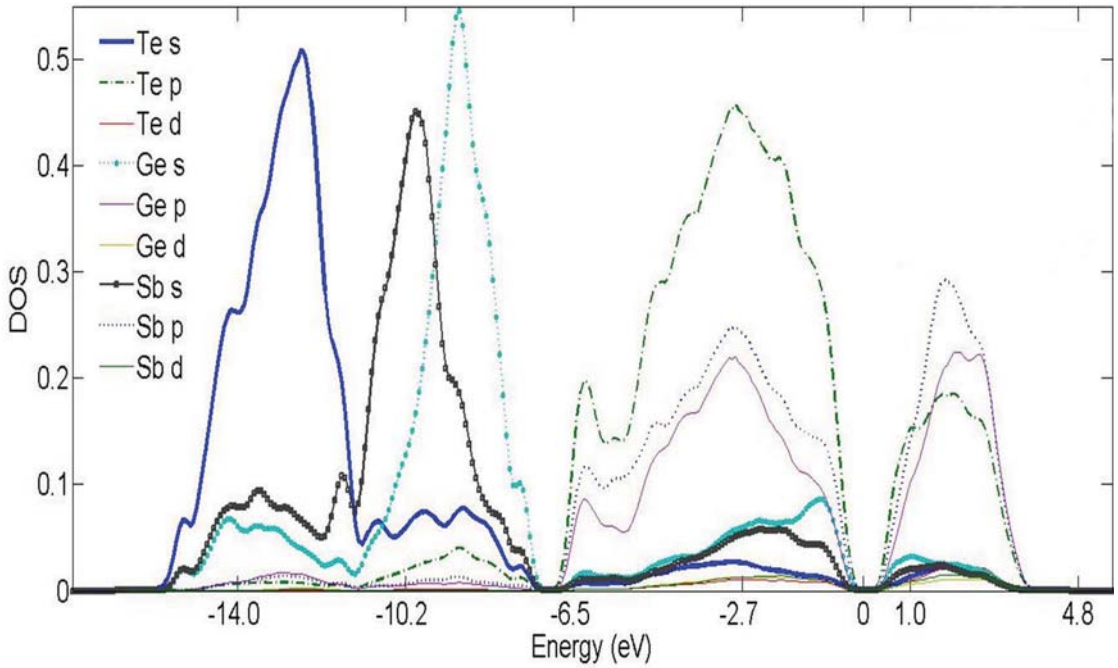

Figure 4.2: Electronic densities of states projected onto different atomic species and orbitals. The Fermi level is at 0 eV.

4.3.2 Electronic Structure

The electronic structure is analyzed through the electronic density of states (EDOS) obtained from Hartree-Fock (HF) calculations. HF is used only to analyze the EDOS, not for forces and total energies. HF is known to exaggerate both the optical gap and charge fluctuations in the electron gas. These features are helpful to us here for diagnosing structural correlations. In the following discussion, the calculated EDOS is averaged over 1000 configurations from the last 2 ps when the cell is in thermal equilibrium at a fixed temperature of $500K$. Finally, the averaged HF result of the amorphous phase gives an electronic gap around $0.4eV$ which is wider than the DFT result–0.2eV [58] and is closer to the experimental value–$0.7eV$ [62]. Although the gap is still smaller than the

experimental value, it is much improved over LDA, and this may imply that HF provides a better starting point for analysis of the electronic structure.

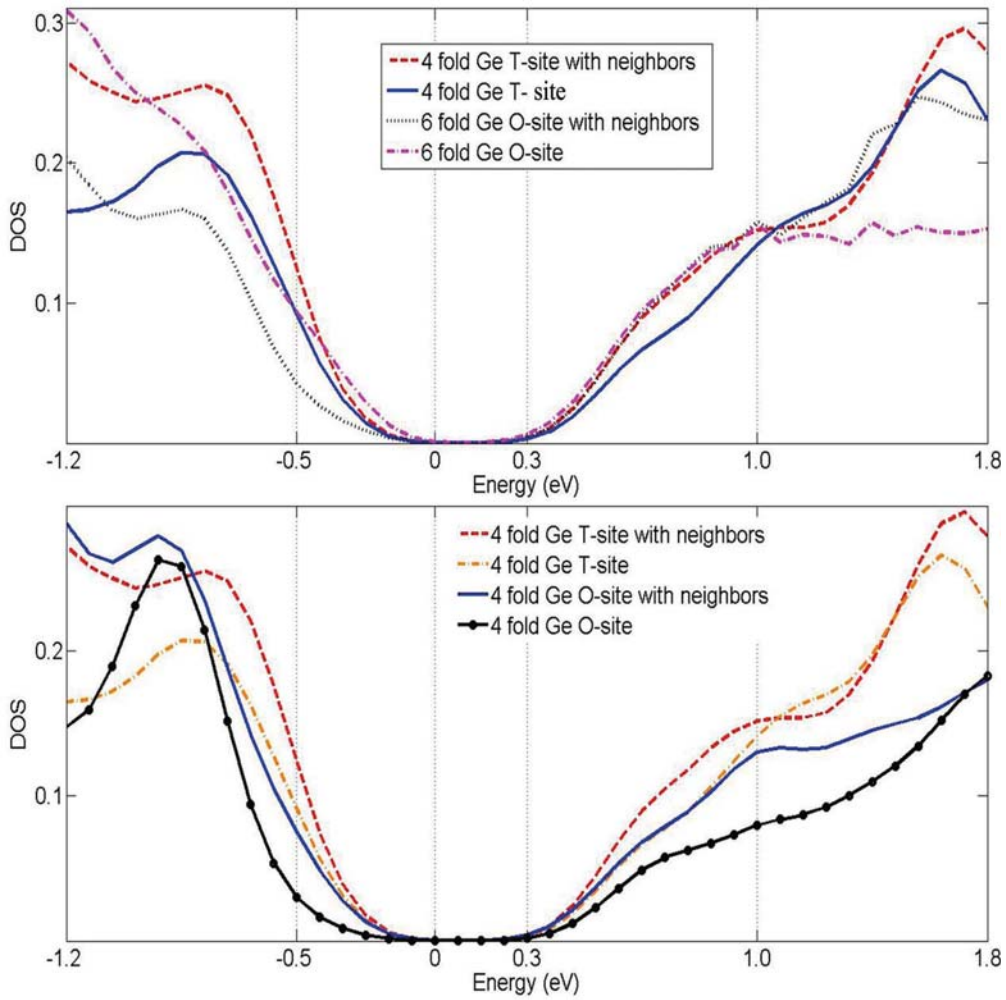

Figure 4.3: Projected EDOS on Ge atoms at tetrahedral and octahedral sites. "T" and "O" represent tetrahedral and octahedral sites. The "Ge-T/O site" plot only considers the contribution of Ge atoms to the EDOS, while the "Ge-T/O site with neighbors" plot contains the contribution of Ge atoms and their neighbors. The Fermi level is at 0 eV.

To correlate topology with electronic structure, I projected the EDOS onto different local sites and are able to attribute the electronic states to specific structural units. I first show the averaged EDOS for different species and orbitals in Fig. 4.3. The key findings

are that, for all three species, p orbitals dominate the gap and tail states; if considering the species, Te-p, Sb-p, Ge-p, Ge-s and Sb-s are important in determining tail states and the magnitude of the gap (Fig. 4.3). To further correlate structural oddities with electronic states, I also sort atoms with specific features into different groups and accumulate the contribution to EDOS. I briefly report that groups forming homopolar or heteropolar bonds showed that there is a significant difference at a "deep gap" around $-7eV$ below the Fermi level ($0eV$) in EDOS (atoms involved in heteropolar bonds form a bigger deep gap); however, atoms forming homopolar bonds have a minor impact on tail states and the electronic gap near the Fermi level. Considering the coordination, for Te, 2-fold Te atoms contribute to a narrowed gap and conduction-band tail states appear; for Ge atoms, the contributions for 3, 4, 5 and 6-fold atoms are almost the same; for Sb atoms, the conduction-band tail of 6-fold Sb atoms is pushed to a low-energy level and the valence-band tail associated with 3-fold Sb atoms which satisfy the "8-N" rule is pushed into a higher energy region. While there are differences in electronic tail states and the gap value associated with coordination numbers, the influence is fairly weak. Similarly, sorting atoms involved in "seeds" or not also showed a minor impact on gap magnitude and tail states.

I also considered the "umbrella flip" of Ge atoms. I compared the EDOS of Ge atoms sitting at octahedral sites (O-site) and tetrahedral sites (T-site), as I illustrate in Fig. 4.3. The projected EDOS on Ge atoms and their neighbors are all considered. The results indicate that 6-fold octahedral Ge and tetrahedral Ge have a similar local gap. However, 4-fold Ge at an octahedral site (4 neighbors with 90 degree angles) have both a shifted valence-band tail and conduction-band tail which may result in a bigger gap. Thus, from the result, sp^3 hybrids introduced by a Ge umbrella-flip may not be the reason for an increased gap in the amorphous phase, but the octahedral Ge existing in the amorphous

phase at least would not increase the electronic gap. Analysis of $Ge_1Sb_2Te_5$ showed a similar result [63].

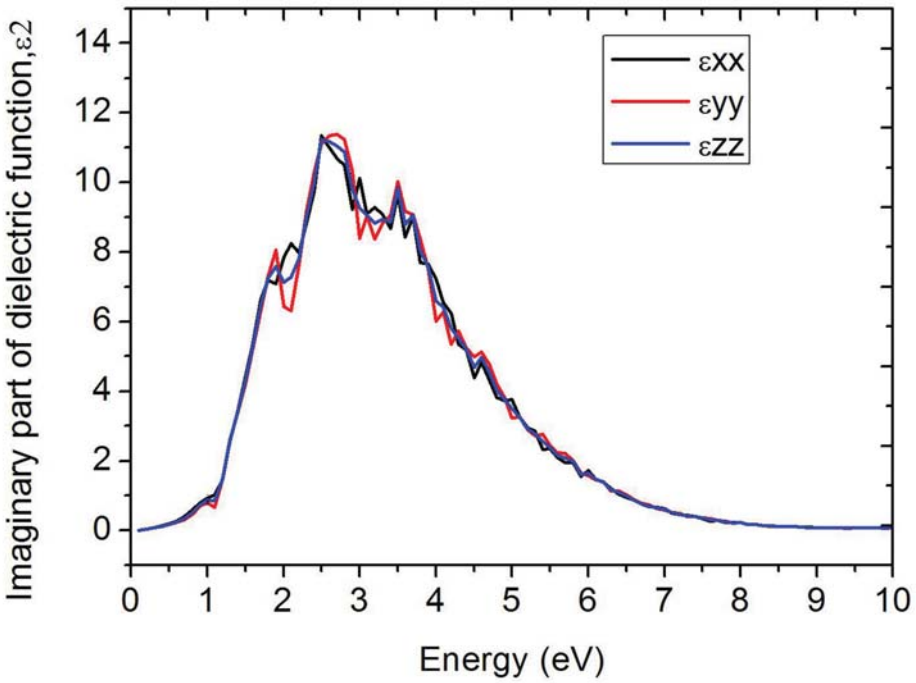

Figure 4.4: AC Dielectric function of a-$Ge_2Sb_2Te_5$. Due to finite size effect, the calculation can not predict valid value for small ω ($\omega \lesssim 2eV$).

Finally for this section, I show one last static property – the dielectric function $\epsilon(\omega)$ in Fig. 4.4. The imaginary part of the dielectric function in three directions are plotted in Fig. 4.4. ϵ reaches its peak for an energy of about 2.5eV and this spectrum is comparable with both experimental and simulation result [63, 64]. Notice that due to the finite-size effect, the result is not valid for $\omega \to 0$. To obtain accurate results for small ω, an extrapolation procedure is required.

4.3.3 Dynamic Analysis

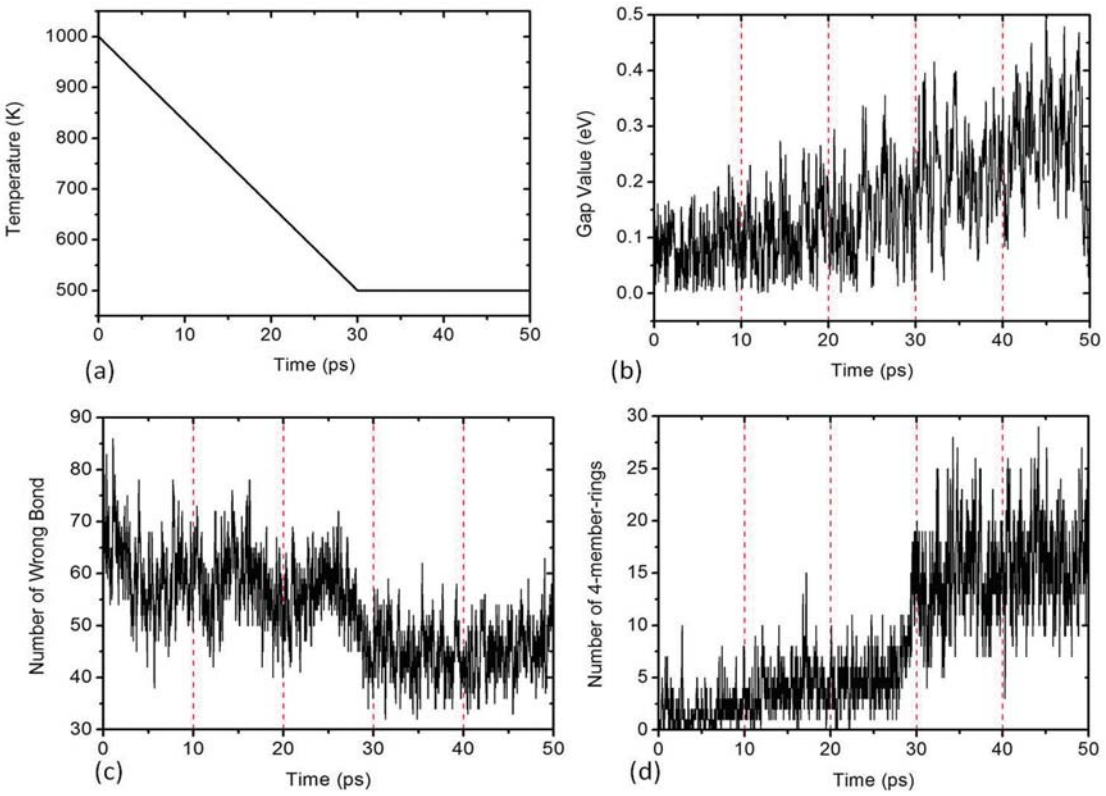

Figure 4.5: Dynamic change of temperature, gap value, number of wrong bonds and squares (seeds).

Next, I performed a dynamic analysis for a-$Ge_2Sb_2Te_5$. I tracked the structure and the electronic gap during a quench from 1000K to 500K with thermal equilibration at 500K (Fig. 4.5). Significant structural changes started to occur after 24ps (the temperature was then near 640K). The number of homopolar bonds dropped, the number of 4-membered rings increased, and the mean coordination increased. The changes in topology are similar to those reported by Ref. [59] and all these shifts signal an increase of both chemical order and structural order. The electronic gap, which I take to be the difference between Highest Occupied Molecular Orbital (HOMO) and Lowest Unoccupied Molecular Orbital

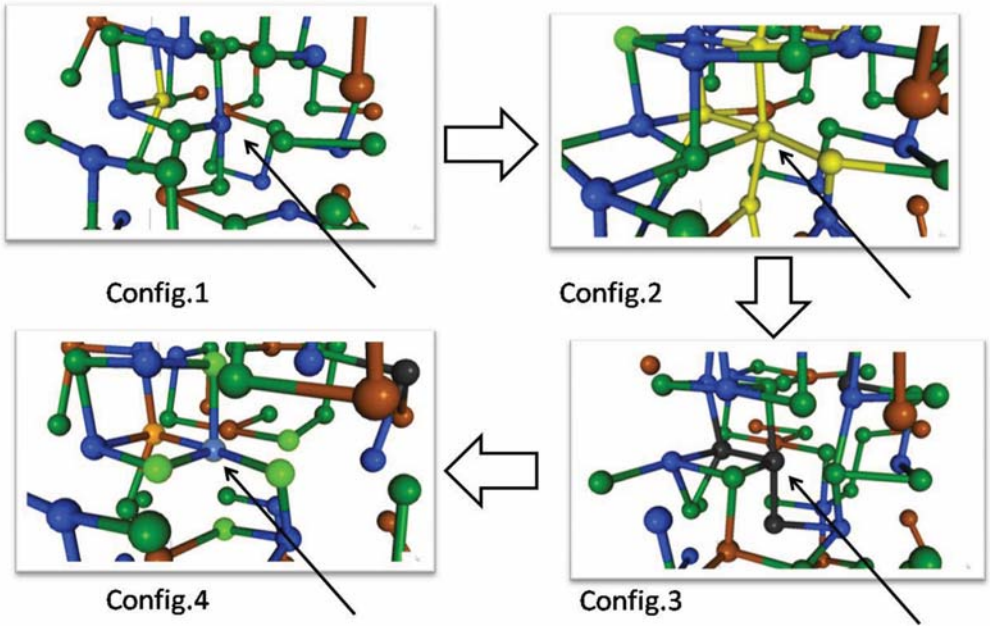

Figure 4.6: Snapshots of topology changes for one Ge atom and its six neighbors (Ge-blue, Sb-brown, Te-green). The central Ge atom is identified by black arrows. The valence-band tail states appear in Config.2 and are localized on yellow atoms. The conduction-band tail states appear in Config.3 and are localized on black atoms.

(LUMO) levels, increased overall, but I observed that there are considerable fluctuations, even for the well-equilibrated system. Local geometry may have huge consequences on the gap.

To study how changes in the local environment at a specific site affected the electronic gap, I tracked a specific unit in the system during equilibration and I show such an evolution for both the topology and the electronic structure in Fig. 4.6 and Fig. 4.7. I mainly focused on one Ge atom which occupied a near-octahedral site (6 nearest Te neighbors with around 90 degree bond angles, indicated by a black arrow in Fig. 4.6) and its six nearest neighbors. I correlated their local bondings and electronic density of states for many time steps. Configurations 1 and 4 exhibit the biggest gap. However, at intermediate steps between configurations 1 to 4, tail states appear. At configuration 2, a

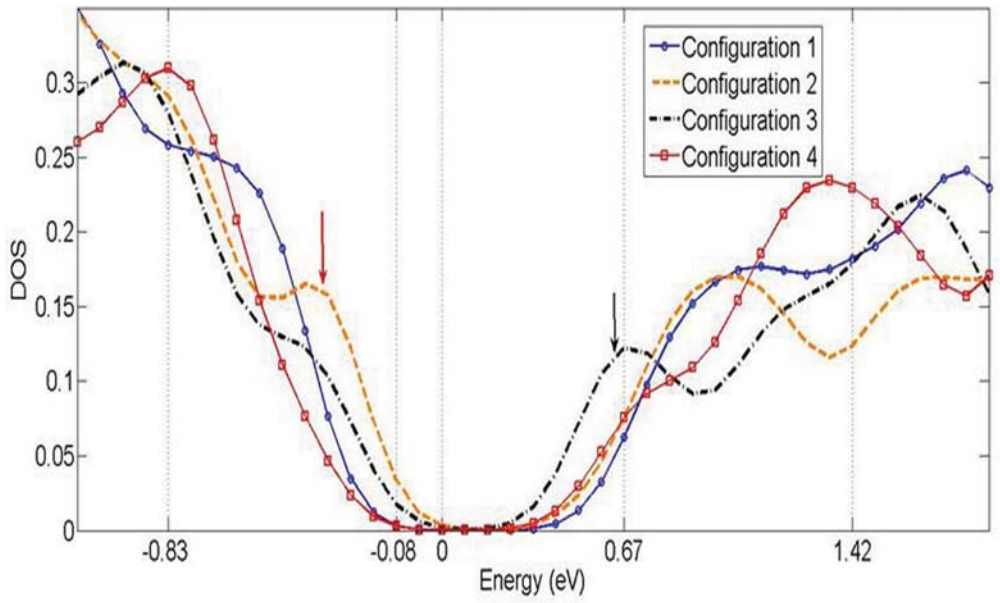

Figure 4.7: Instantaneous snapshots of EDOS correlated with the configurations of Fig. 4.6. A smaller gap appear in Config.2&3. The valence-band tail states (orange arrow) are associated with yellow atoms in Config.2 of Fig. 4.6. The conduction-band tail states (black arrow) are associated with black atoms in Config.3 of Fig. 4.6. The Fermi level is at 0 eV.

valence-band tail state was present and it was mainly localized on the central Ge atom and four of its nearest neighbors (yellow atoms in Config.2 of Fig. 4.6); at configuration 3, a conduction-band tail appears, mainly localized on the center Ge atom and two of its nearest neighbors (black atoms in Config.3 of Fig. 4.6). I should emphasize that from configurations 1 to 4, the whole network did not experience a major change, but the electronic gap fluctuates. Thus, the appearance of valence-band and conduction-band tails are strongly associated with distortions at this Ge site. The simulations emphasize the dynamic nature of the electronic band tails in $Ge_2Sb_2Te_5$.

4.3.4 Relaxation Analysis for Crystal Phase of $Ge_2Sb_2Te_5$

In this section, I discuss relaxation effects for crystalline $Ge_2Sb_2Te_5$ with 10% vacancies. As mentioned above, the 108-atom cell was obtained based on the NaCl

rock-salt structure. I show the electronic density of states for both unrelaxed and relaxed models in Fig. 4.8 obtained through HF calculations. For both models, Te atoms have a major effect on the valence tail which may be due to the vacancies; Sb atoms contribute more to conduction tail. I could see clearly that the electronic gap opened up after relaxation. Moreover, I tracked the dynamic change of the Highest Occupied Molecular Orbital (HOMO) and Lowest Unoccupied Molecular Orbital (LUMO) and plot them in Fig. 4.9. It is clear from the plot that the total energy is reduced and both HOMO and LUMO levels are shifted. The HOMO level is pushed away by 0.1eV and the LUMO level is pushed up by 0.2eV.

Since the crystal model has 10% vacancies, the relaxation actually introduced slight distortion into the network. The structural statistics indicate that the mean coordination of Te, Ge and Sb atoms all decreased. The mean coordination of Te are decreased from 4.8 to 4.28, Sb and Ge dropped from 6 to 5.47 and 5.23 correspondingly. The angle distribution, especially the X-Ge-X and X-Sb-X angle distributions, are also changed. This result indicates that the existence of vacancies and the distortion happened to the network will have a impact on gap. Thus, by controlling the concentration of vacancies and distortion, I may obtained different electronic gap values. This result is similar to results on other Ge-Sb-Te alloys [64].

4.4 Conclusions

I made $Ge_2Sb_2Te_5$ models with a ‘quench from melt’ method. HF calculations give a 0.4eV electronic gap for the amorphous phase. I found that Te-p, Sb-p, Ge-p, Ge-s and Sb-s orbitals are most important to tail states. 6-fold octahedral Ge and 4-fold tetrahedral Ge give rise to similar gaps but 4-fold octahedral Ge results in a bigger gap with both shifted valence-band and conduction-band tails. The study also reveals a large fluctuation

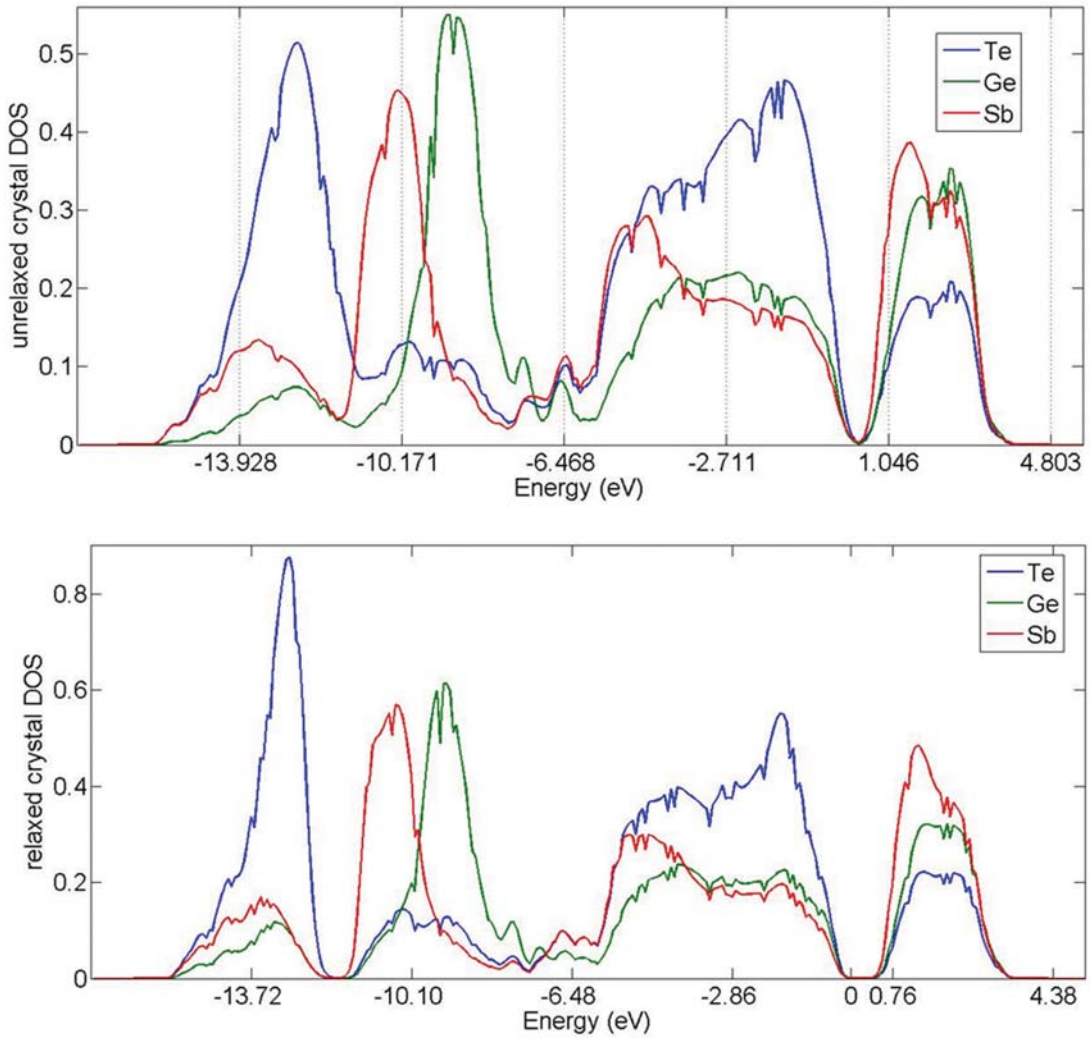

Figure 4.8: Electronic density of states of crystal models projected onto different species of atoms. (Top-panel) Unrelaxed crystal model with vacancies. (Bottom-panel) Relaxed crystal model.

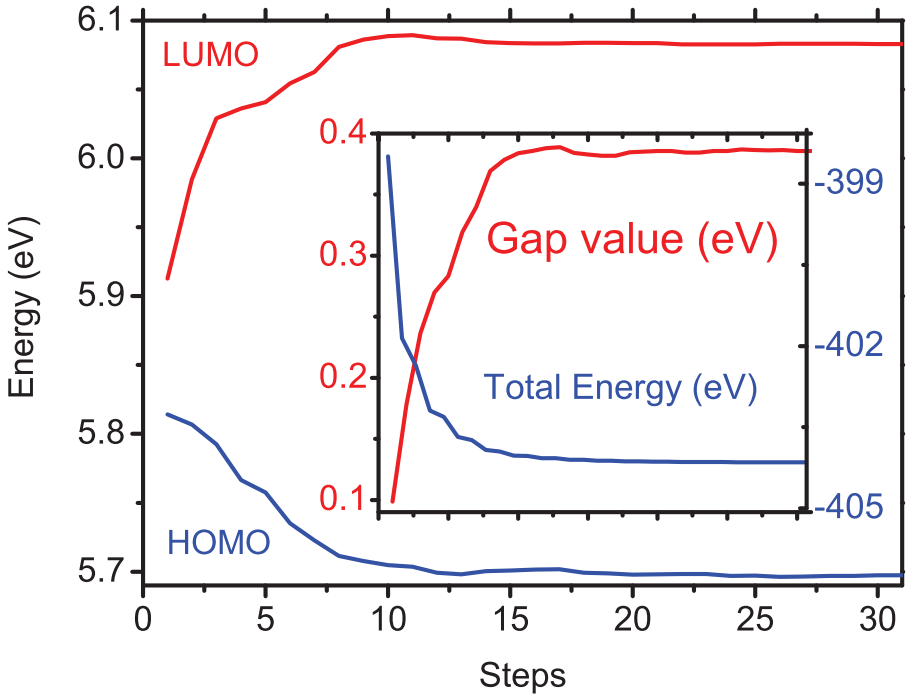

Figure 4.9: Change of LUMO, HOMO level, gap value and total energy during relaxation.

in gap value during thermal equilibration which is partially due to the appearance and disappearance of conduction-band and valence-band tail states. Such fluctuations could be associated with the local structural change/distortion of Ge atoms, which introduce localized tail states and have an impact on the electronic gap. Also, the relaxation analysis on crystal phase of $Ge_2Sb_2Te_5$ indicates that vacancies and distortions may play an important role in determining the electronic gap.

The following work in Chapter 5 is published in

B. Cai, X. Zhang and D. A. Drabold, Physical Review B **83**, 092202 (2011).

5 Building Block Modeling Technique: Application to Ternary Chalcogenide Glasses g-$Ge_2As_4Se_4$ and g-$AsGe_{0.8}Se_{0.8}$

5.1 Background

Owing to promising optoelectronic and electronic features[65–67], chalcogenide glasses have drawn extensive attention during last decade. However, the lack of translational periodicity makes it hard to predict the microscopic structure of these glasses. Experimental results indicate that chemical order is broken and homopolar bonds are observed in chalcogenide glasses[68–70]. To further understand the topology and its role in determining optoelectronic and electronic properties, realistic atomistic models of these glasses are required. One possible way to obtain atomic models for glasses is the standard molecular dynamic (MD) 'melt and quench' method. This method seems to work when there are fundamental units existing in both liquid and glass. For simple Building Blocks (BBs) (involving only a few atoms), realistic models are obtained after a long liquid equilibration and a slow quench procedure. However, if the BBs are complex, such as the case in ternary alloys, it sometimes happens that the 'melt and quench' method fails to obtain the correct structure due to the limitation of short simulation times. If *a priori* information (such as chemical order, correct coordination number, etc.) is unknown for a target material, the 'melt and quench' technique usually starts with random initial configurations and the calculations may be extremely time-consuming for large systems. Also, very large cells may be required if the structure order is complex. The earlier studies indicated that 'melt and quench' method has difficulties in generating realistic atomic models of Ge-As-Se glasses (more details are discussed in Ref.[10]). Thus, in this case, it is of interest to develop a new modeling technique.

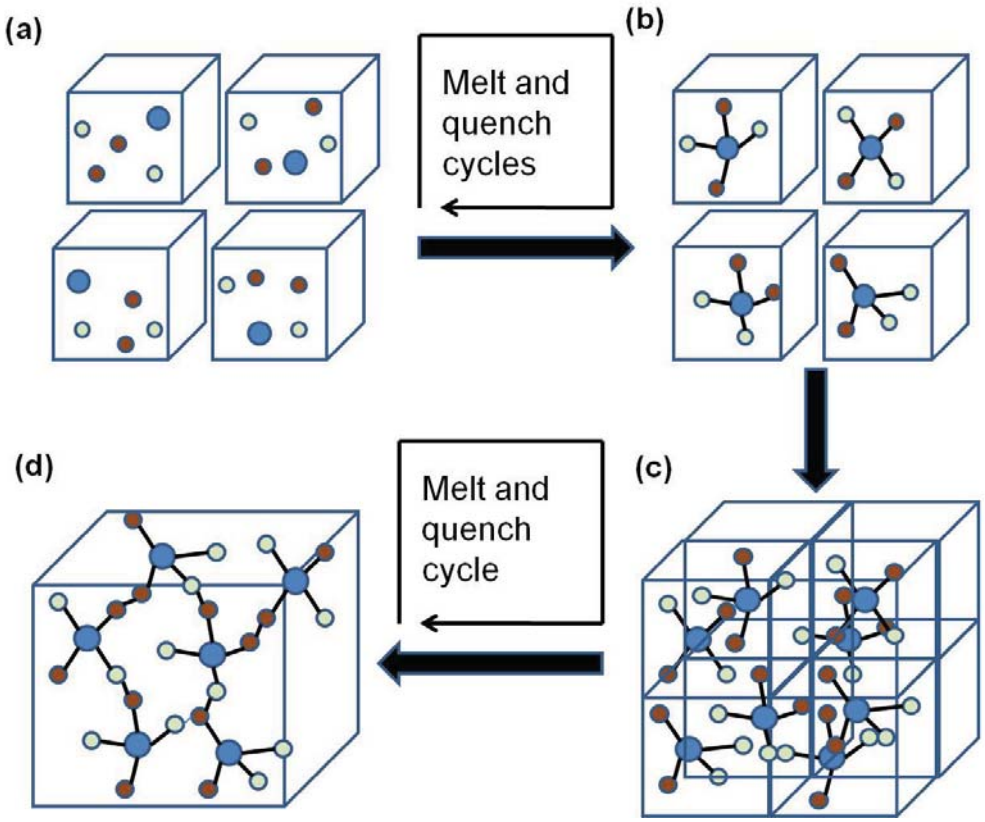

Figure 5.1: (Color online) Flowchart for building block modeling method. (a) Atoms in sub-units cell with random initial positions. (b) Building blocks (BBs) are obtained after several 'melt and quench' cycles with unchanged minimum energy. (c) A large cell built, based on BBs. (d) Final models are obtained after one melt, quench/anneal cycle.

Since BBs play important roles in the 'melt and quench' method, we may first attempt to generate energetically reasonable (energy is minimum) BBs and then build a large cell from those BBs. This idea is based on two assumptions: (1) No dramatic changes in local order occur between the large system and small system; (2) BBs exist in these glasses and the correct chemical order can be obtained by a long *ab-inito* molecular dynamic simulation [3, 10]. In this paper, I describe a systematic modeling technique to obtain BBs and then to achieve big models. By applying this method, *ab-initio* Molecular Dynamic models of g-$Ge_2As_4Se_4$ and g-$AsGe_{0.8}Se_{0.8}$are constructed. I compare radial distribution function of g-$Ge_2As_4Se_4$ with experimental data and predict the partial pair correlation function for both g-$Ge_2As_4Se_4$ and g-$AsGe_{0.8}Se_{0.8}$. The electronic structures are studied through the electronic density of states. I found a $0.34eV$ and a $0.38eV$ electronic band gap for g-$Ge_2As_4Se_4$ and g-$AsGe_{0.8}Se_{0.8}$ within the local density approximation (LDA). The vibrational density of states are also discussed.

5.2 Models and Simulation Method

I start the discussion by describing the MD procedures that are used to generate the atomic models. A flowchart to illustrate this method is given in Fig. 5.1. A small number of atoms are randomly placed into a cubic box, the sub-unit cell, with the correct stoichiometry and experimental mass density. For g-$Ge_2As_4Se_4$, 25 atoms (5 Ge,10 Se and 10 As) are in each sub-unit cell with mass density 4.687g/cm^3 (lattice constant is 8.75Å). For g-$AsGe_{0.8}Se_{0.8}$, 26 atoms (8 Ge,10 As and 8 Se) are in each sub-unit cell with mass density $4.459g/cm^3$ (lattice constant is 9Å). The sub-unit cells are then melted at $5000K$ for 1ps, equilibrated at $2000K$ for 15 ps, cooled over $1000K$ for 15 ps, annealed to $300K$ for 15 ps and quenched to $0K$. These steps are repeated on the same sub-units for several cycles, until the minimum energy structures are unchanged. At this point, energetically optimized BBs are obtained. Then large unit cells are built from these BBs (200 atoms

cells for g-$Ge_2As_4Se_4$ and 208 atoms cell for g-$AsGe_{0.8}Se_{0.8}$). The large cells are equilibrated at 1500K (above the melting point) for 7.5 ps, annealed to 300K and quenched to 0K. All the MD steps are done via the density functional quantum molecular dynamic method FIREBALL96 with local basis sets[71, 72]. The detailed procedure was also discussed in Ref [10]. To further improve the chemical order and eliminate artifacts of the minimal basis, I annealed the models at 300K for 5 ps and quench to 0K with the Vienna Ab-initio Simulation Package (VASP)–a plane wave density functional theory(DFT) code using the local density approximation (LDA)[12, 31]. Finally, the final models are obtained after an energy relaxation. In all calculations, only the Γ point is used to sample the Brillouin zone. The electronic density of states (EDOS) is calculated with VASP.

5.3 Results and Discussions

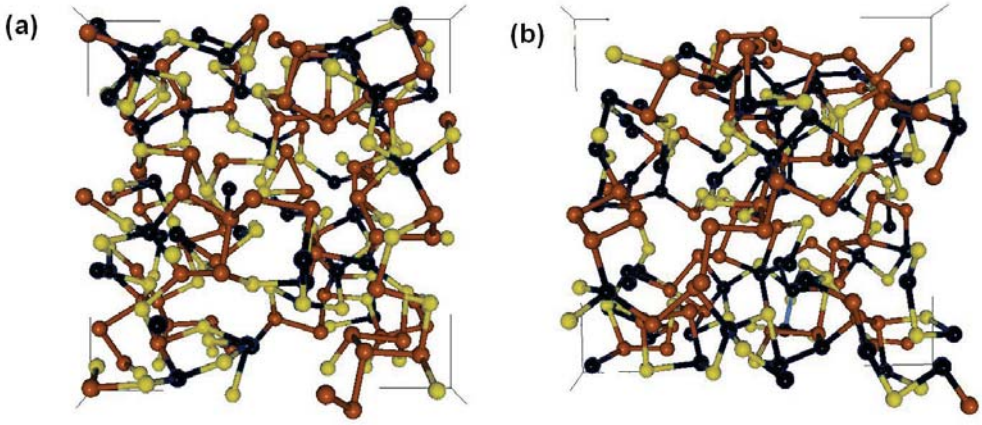

Figure 5.2: (Color online) Atomic models for (a) 200-atom g-$Ge_2As_4Se_4$ and (b) 208-atom g-$AsGe_{0.8}Se_{0.8}$. Black (dark) atoms are Ge. Brown (grey) atoms are As. Green (light) atoms are Se.

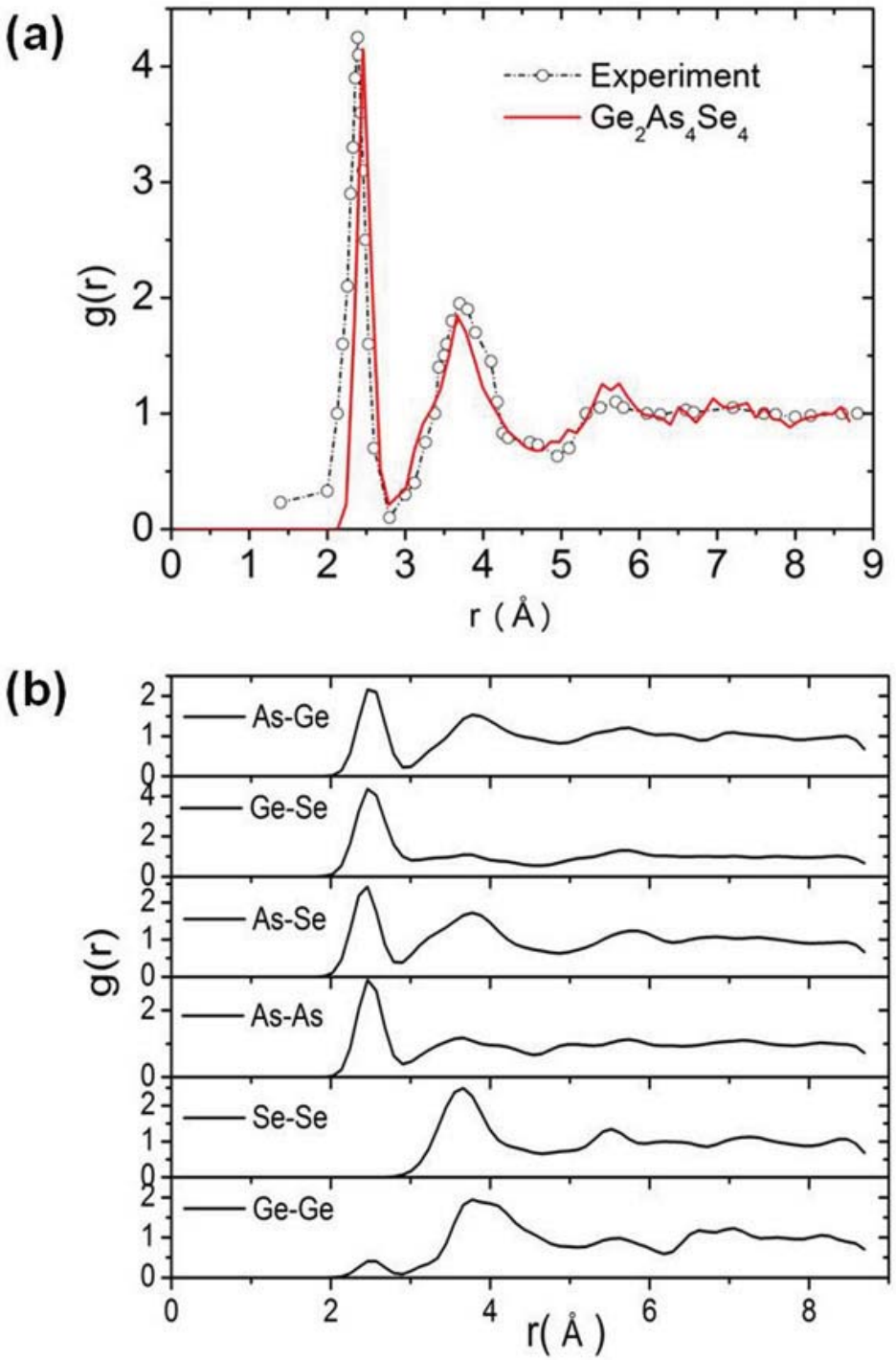

Figure 5.3: (Color online) Radial distributions and partial pair correlation functions of g-$Ge_2As_4Se_4$. Experimental data is from Ref.[1].

Table 5.1: Mean bond length in g-$Ge_2As_4Se_4$ and comparison with Ref.[1].

Bond type	Distance (Å)	Ref.[1]. (Å)
Ge-Ge	2.47	2.51±0.19
Ge-As	2.53	2.44±0.14
Ge-Se	2.53	2.48±0.15
As-As	2.50	2.41±0.07
As-Se	2.44	2.41±0.06

The final models are shown in Fig.5.2. I emphasize that there are no remaining correlations between the sub-unit cells in the final models. For g-$Ge_2As_4Se_4$, the radial distribution functions (RDF) and partial pair correlation functions (PPCF) are shown in Fig.5.3. The calculated total RDF indicates a sharp first peak at 2.47Å, a first minimum at 2.81Å and a broad second peak around 3.7Å. All the peak positions agree with experimental data from Ref.[1], which implies that the building block techniques manage to obtain not only the correct local structure order but also a reasonable medium range order. The partial pair correlation functions for g-$Ge_2As_4Se_4$ are ploted in Fig.5.3(b). Ge-Se, As-Se, Ge-As and As-As all have a strong first peak around 2.5Å which collectively produce the first peak in the total RDF. Se-Se homopolar-bonds are not observed in the models. I also noticed that As atoms bond with both Ge and Se atoms, which does not support the assumption that As-Ge bonds have low formation probability[73]. I list the averaged bond distance in Table 5.1 and they are close to the value predicted in Ref.[1]. Notice that Ref.[1] predicted 2.41Å for As-As bond which is 3% lower than the standard value (2.49Å for amorphous As[74] and 2.51Å in rhombohedric As[75]), the results are actually closer to the standard value. For g-$AsGe_{0.8}Se_{0.8}$, the total RDF shows similar features to g-$Ge_2As_4Se_4$. With an increased concentration of Ge atoms, As-Se partial exhibits a weak first peak and a strong second

peak; the number of Ge-Ge bonds are also increased. Again, Se-Se bonds are not observed.

The structural statistics for coordination and chemical order are computed for both models, and I report the results in Table 5.2. One result is that the '8-N' rule is not valid for my models. For g-$Ge_2As_4Se_4$, the majority of Ge, As and Se are four-fold, three-fold and two-fold, respectively. However, there is a significant fraction of three-fold Ge atoms and three-fold Se atoms in the system. For g-$AsGe_{0.8}Se_{0.8}$, the majority of Ge atoms are still four-fold and As atoms remain three-fold, while *most* Se atoms are three-fold. This may be due to a relatively large concentration of Ge atoms (compared with g-$Ge_2As_4Se_4$) and implies that g-$AsGe_{0.8}Se_{0.8}$ has a more rigid three dimensional network. These under-coordinated Ge atoms and over-coordinated Se atoms do not introduce mid-gap states or highly localized tail sates, so I do not interpret them as a defect. The average coordination $\langle r \rangle$ of the model is 2.93 for g-$Ge_2As_4Se_4$ and 3.08 for g-$AsGe_{0.8}Se_{0.8}$, which is different from the standard values proposed by Thorpe and Phillips (2.8 for g-$Ge_2As_4Se_4$ and 3.0 for g-$AsGe_{0.8}Se_{0.8}$) based on '8-N' constraints [76, 77] (where the averaged coordination $\langle r \rangle$ is calculated as $\langle r \rangle = 4X_{Ge} + 3X_{As} + 2X_{Se}$. X_{Ge}, X_{As} and X_{Se} are the concentration of Ge, As and Se atoms). When $\langle r \rangle$ is bigger than 2.8, it is believed that Ge-As-Se alloys form a three-dimensional rigid network due to the vulcanization or *cross-linking*. The difference here may imply that the constraint counting of Ge-As-Se alloys in this cross-linked 3-D region should be carefully reconsidered. Violations of the $8 - N$ rule are well known in other chalcogenide systems[51].

Without any *a priori* information, the building-block method provided us reasonable models of g-$Ge_2As_4Se_4$ and g-$AsGe_{0.8}Se_{0.8}$. I should be clear that the building block technique is not new in modeling disordered materials. Amorphous Si_3N_4 models were made by Ouyang and co-authors through assembling a small number of fundamental

Table 5.2: Coordination numbers and bond type analysis of computer generated g-$Ge_2As_4Se_4$ and g-$AsGe_{0.8}Se_{0.8}$.

Alloys	Element	Coordination					Bond type		
		5	4	3	2	Mean	Ge%	As%	Se%
g-$Ge_2As_4Se_4$	Ge	4	20	16	0	3.7	3	30	67
	As	0	6	74	0	3.1	18	45	37
	Se	0	1	30	49	2.4	52	48	0
g-$AsGe_{0.8}Se_{0.8}$	Ge	1	37	26	0	3.6	14	34	52
	As	0	8	70	2	3.1	32	49	19
	Se	0	0	39	25	2.6	72	28	0

building blocks[78]. However, the building blocks were built purely from first principle calculation and the recipe is, in principle, perfectly general. Moreover, the final 'melt and quench' cycle for the large cell managed to maintain correct short range order, destroy the correlation of BBs and obtain credible medium range order at the same time. Considering the efficiency, since the large cells are constructed based on reasonable BBs, the simulation has a shorter computation time compared to the traditional method searching for optimum structures from random initials.

The electronic structure was analyzed through electronic density of states (EDOS) and inverse participation ratio (IPR). The IPR measures the localization for each eigenstate. For ideally localized states, $IPR = 1$; for extended states, IPR=N^{-1}, where N is the number of atoms. (Details are discussed in Ref.[53]. All calculations are done via VASP.) The EDOS of g-$Ge_2As_4Se_4$ in Fig.5.4 indicates a $0.34eV$ band gap and a mid-gap state. High IPR states are observed in the region from $-15.5eV$ to $-6.5eV$ and around the

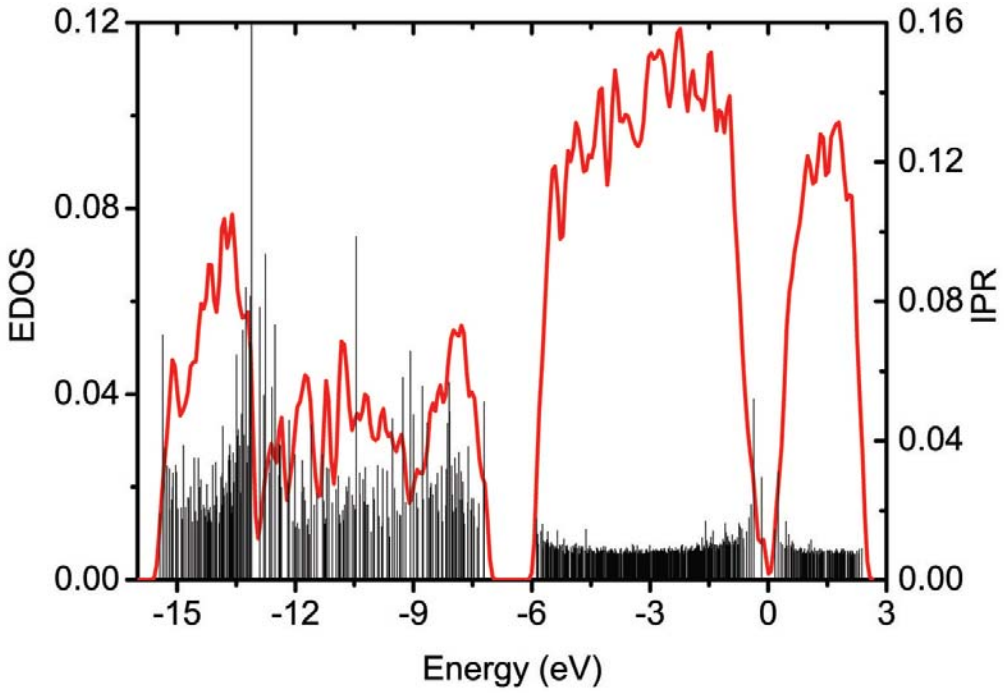

Figure 5.4: (Color online) Electronic density of states (EDOS) and inverse participation ratio (IPR) for g-$Ge_2As_4Se_4$ model. The Fermi level is at 0 eV.

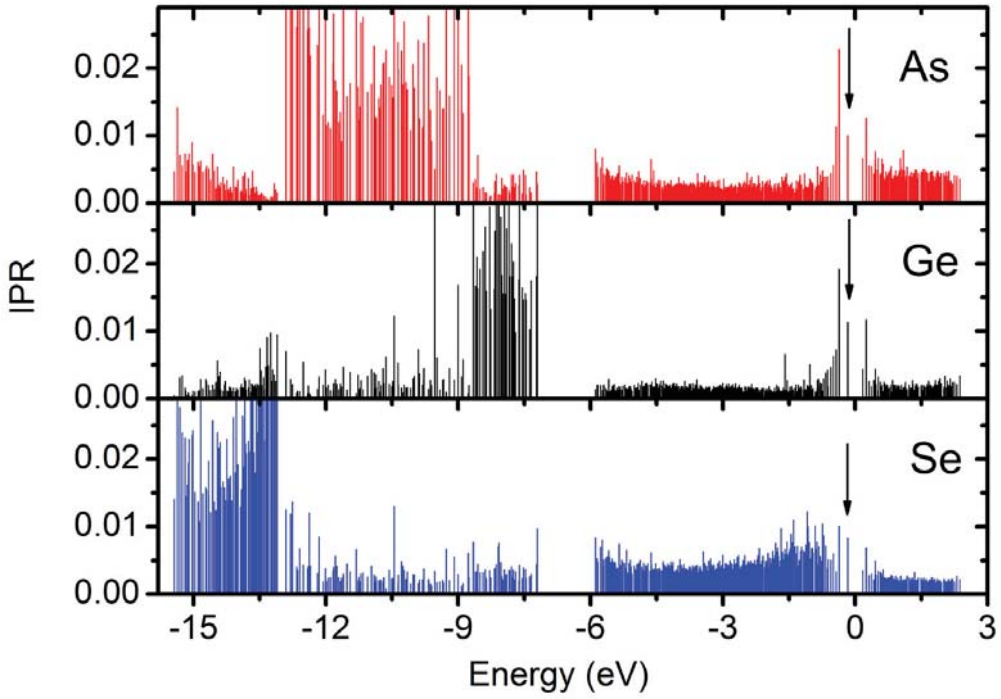

Figure 5.5: (Color online) Projected IPR for g-$Ge_2As_4Se_4$ according to different species. The mid-gap state is marked by black arrow. The Fermi level is at 0 eV.

valence and conduction band edge. I then studied the localization by projecting the density of states onto different species. We could see from Fig.5.5, that Se atoms contribute to the region from -15.5eV to $-13eV$, As atoms contribute to the region from $-12.9eV$ to $-8.6eV$ and Ge atoms contribute to the region from $-8.6eV$ to $-7.2eV$. The eigenstates in the region from $-5eV$ to $-1eV$ are quite extended. The valence band tail states and conduction band tail states are tend to be localized on As and Ge atoms. A further investigation shows that the gap states are mainly localized on over-coordinated (five-fold) Ge atoms and its neighbors. The valence tail state with highest IPR, is localized on a distorted site where three atoms (1 Ge, 1 As and 1 Se) form a triangle. I believe that the 'over-coordinated' Ge site and the distorted triangle site would be eliminated through an extended annealing. The DOS of g-$AsGe_{0.8}Se_{0.8}$ exhibits a similar shape to g-$AsGe_{0.8}Se_{0.8}$ but with a $0.38eV$ band gap and no mid-gap states. As atoms highly contribute to the valence and conduction band tail states. I should point out here that under-coordinated (3-fold) Ge atoms and over-coordinated (3-fold) Se atoms do not introduce localized states or mid-gap states, especially in g-$AsGe_{0.8}Se_{0.8}$ where most Se are 3-fold, which implies that they are not defects in the network. It is well known that the LDA method always under-estimates the magnitude of the band gap, so other techniques could be applied to get a better predication for the band gap[51].

5.4 Conclusions

To sum up, I introduced a BB modeling technique and applied it to obtain atomic models of g-$Ge_2As_4Se_4$ and g-$AsGe_{0.8}Se_{0.8}$. Both models predict reasonable RDFs and PPCFs, and the RDF of g-$Ge_2As_4Se_4$ shows reasonable agreement with experimental data. A significant fraction of over-coordinated Ge and under-coordinated Se are found in the system without introducing defect states in electronic structure, and I believe that these under-coordinated (3-fold) Ge and over-coordinated Se (3-fold) are not defects. This

result may imply that the ‘8-N’ rule is violated and the coordination constraint counting should be reconsidered in the rigid network region of Ge-As-Se alloys. I found a $0.34eV$ band gap with a mid-gap state for g-$Ge_2As_4Se_4$ and $0.38eV$ band gap for g-$AsGe_{0.8}Se_{0.8}$, which could be well under-estimate by LDA method.

The following work in Chapter 6 is published in

B. Cai, A. L. Goodwin and D. A. Drabold, Modelling Simul. Mater. Sci. Eng. **19**, 035010 (2011).

6 Chapter: Spatial Uniformity as a Principle for Determination of Atomistic Structural Models

6.1 Introduction

The lack of translational periodicity is an essential feature of amorphous solids. Because of the absence of long-range order, it is always a challenge to create realistic atomistic models. Still, *local* (short-range) structural order does exist in all amorphous materials. Experimental information about this local ordering is provided by x-ray and neutron diffraction, and other probes. Information-based modeling, including the Reverse Monte Carlo(RMC) method, may be used to generate models consistent with such diffraction measurements. Unfortunately, the atomic models obtained from such methods are not unique. In other words, various, and indeed discrepant models can reproduce the same RDF data, and these models usually have an unphysical concentration of chemical and/or coordination defects. To remedy this, empirical assumptions are usually made and applied with the RMC in the form of constraints on coordination numbers, bond angles etc. For different atomic species, these assumptions vary, so it is hard to form a routine or universal RMC approach.

Recently, a new method, the "Invariant Environment Refinement Technique" (INVERT) has been shown to improve chemical and topological order for C_{60}, a-Si and a-SiO_2[13]. The underlying idea of the technique is the concept of uniformity. By insisting on maximum spatial uniformity, empirical constraints become unnecessary. Thus, the single requirement of maximum uniformity may become a generic prescription for modeling many homogeneously disordered by materials. In this paper, I further develop the RMC+INVERT method and apply it to a-GeO_2 and a-H_2O. For materials with a relatively uniform structure, like GeO_2, fitting partial RDFs, INVERT+RMC leads to much improved models in terms of both chemical order and local topological order (as

gauged by the distribution of bond angles). In the case of a-H_2O, I show that the new technique can impose suitable medium range order and easily handle the rigid molecule constraint. Moreover, for both cases, INVERT+RMC method is more efficient than traditional RMC method.

Of course, no method is a panacea, and INVERT+RMC is no exception. For systems that are not structurally uniform, the method is difficult to apply. I am presently trying to develop suitable generalizations to handle such cases, but the jury is still out! Nevertheless, many important amorphous systems are quite structurally homogeneous, and for these, it is clear that INVERT+RMC is helpful. Moreover, this method is very much based on real space where the whole "INVERT" strategy is most naturally implemented. I admit that to get better atomic models the information from structure factor should be also considered. The INVERT, radial distribution functions and structure factors could be combined together into the modeling process.

Philosophically, it is clear that an ideal structure inversion method should produce models consistent with my full knowledge base: an ideal model contradicts no experiments that I believe and must also be a suitable energy minimum according to accurate interatomic interactions. Thus, INVERT+RMC is useful both as a tool for inverting experimental data, and as a means of requiring a model to agree with experiments within an experimentally constrained molecular relaxation approach[3, 79, 80].

6.2 Method and Development

Compared with traditional RMC, the INVERT+RMC method requires a system to have maximum structural uniformity consistent with the experimental data: namely, each distinct site is required to have an identical local environment to the maximum degree possible. By introducing atomic RDF, $g_i(r)$, the idea is to connect each individual site to

experimental RDF data. To implement this strategy, two major terms are included in the cost function for each individual site: the RDF fitting term (6.1) and the variance term(6.2) which maximize uniformity.

$$\chi^2_{RDF,i} = \sum_r [g_i(r) - g(r)]^2 \tag{6.1}$$

$$\chi^2_{VAR,i} = \sum_j \frac{[d_i(j) - \langle d(j)\rangle]^2}{\langle d(j)\rangle^2} \tag{6.2}$$

The total cost function would then have the form:

$$\chi^2 = \sum_{i=all,atoms} (\chi^2_{RDF,i} + \chi^2_{VAR,i}) \tag{6.3}$$

The RDF term quantifies the difference between the calculated atomic RDF data for each site in the model and the experimental data. The variance term measures the dispersion in local environment for each site. The simplest type of materials, containing a single atomic local environment such as C_{60} and a-Si, have been discussed in a previous paper[13]. For a system with two or more distinct sites, the cost functions will be modified to the form (6.4) and (6.5).

$$\chi^2_{RDF,i\alpha} = \sum_{\beta=allspecies} \sum_r [g_{i,\alpha\beta}(r) - g_{\alpha\beta}(r)]^2 \tag{6.4}$$

$$\chi^2_{VAR,i\alpha} = \sum_{\beta=allspecies} \sum_j \frac{[d_{i\alpha}(j,\beta) - \langle d_\alpha(j,\beta)\rangle]^2}{\langle d_\alpha(j,\beta)\rangle^2} \tag{6.5}$$

In the RDF term, experimental data (a partial RDF) is used for each distinct site. For a site i with type α, different partials $g_{\alpha\beta}(r)$ will be fitted separately according to different type β. In the variance term, the distance to different neighbors with respect to different types will be considered separately. $d_{i\alpha}(j,\beta)$ means the distance from a site i with type α to its j^{th} neighbor with type β; $< d_\alpha(j,\beta) >$ means the average distance from atoms with

type α to their j^{th} with type β. The partial RDF can be obtained experimentally using the method of isotopic substitution in neutron diffraction[68, 70], or other methods.

6.3 Results

6.3.1 a-GeO_2

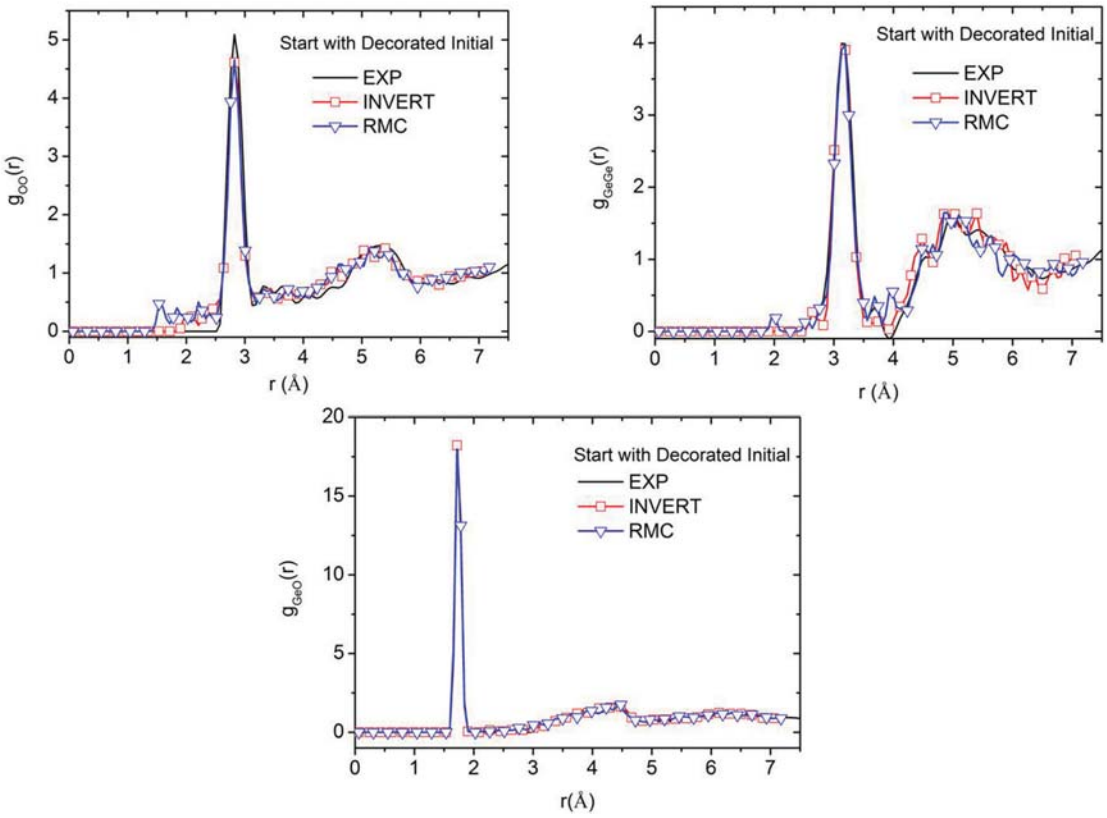

Figure 6.1: Comparison of partial radial distribution functions for 192-atom a-GeO_2 model obtained by different methods staring with decorated initial configuration. (See text.)

I first applied the INVERT+RMC method to model a binary material: a-GeO_2 and compared it with traditional unconstrained RMC method. The experimental partial RDF data is obtained from reference[70, 81]. There are two distinct sites in the a-GeO_2

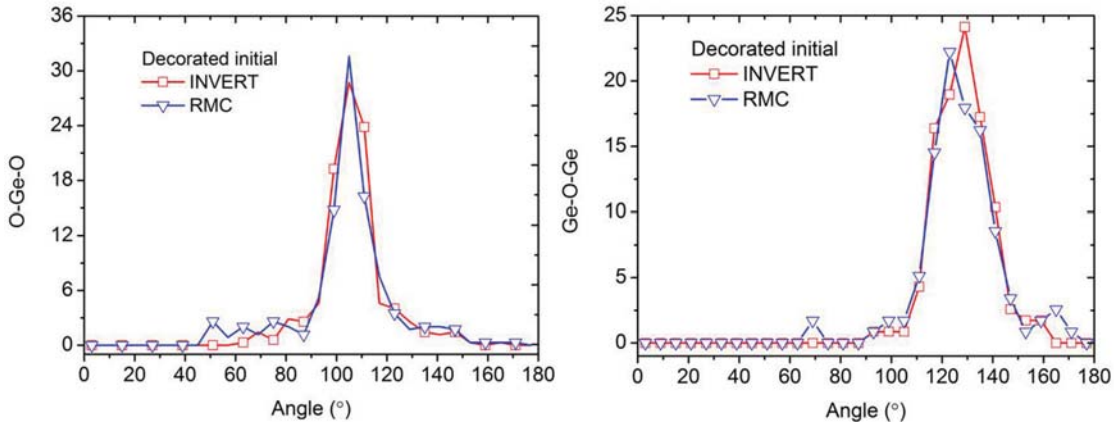

Figure 6.2: Comparison of angle distributions calculated for 192-atom a-GeO_2 model obtained by different methods staring with decorated initial configuration.

network: Ge and O sites. In theory, Ge atoms with its four O atoms form tetrahedral structures with O-Ge-O bond angle around 109.47^o; O atoms are two-fold and form an average bond angle around 132^o[70, 81, 82]. However, I should emphasize that according to experimental results from Salmon and his colleagues, the mean coordination of Ge, n_{Ge-O}, is 3.8(less than 4, I enforce) with $r_{Ge-O} = 1.73$Å.

Two initial configurations are used: decorated initial model and random initial model. The decorated initial configuration is generated by substituting Ge for Si in an a-Si_2 cell (made with WWW method[83]), decorated all the Ge-Ge bonds with a bond-center O, and re-scaled the cell to satisfy experimental mass density[84]. The random initial configuration has totaly randomized atomic coordinations with NO constraints. For comparison, I applied both INVERT and traditional RMC on 192-atom cells with the initial configurations mentioned above. I plot the results with decorated initial configuration in Fig. 6.1 and Fig. 6.2, and random initial configurations in Fig. 6.3 and Fig. 6.4.

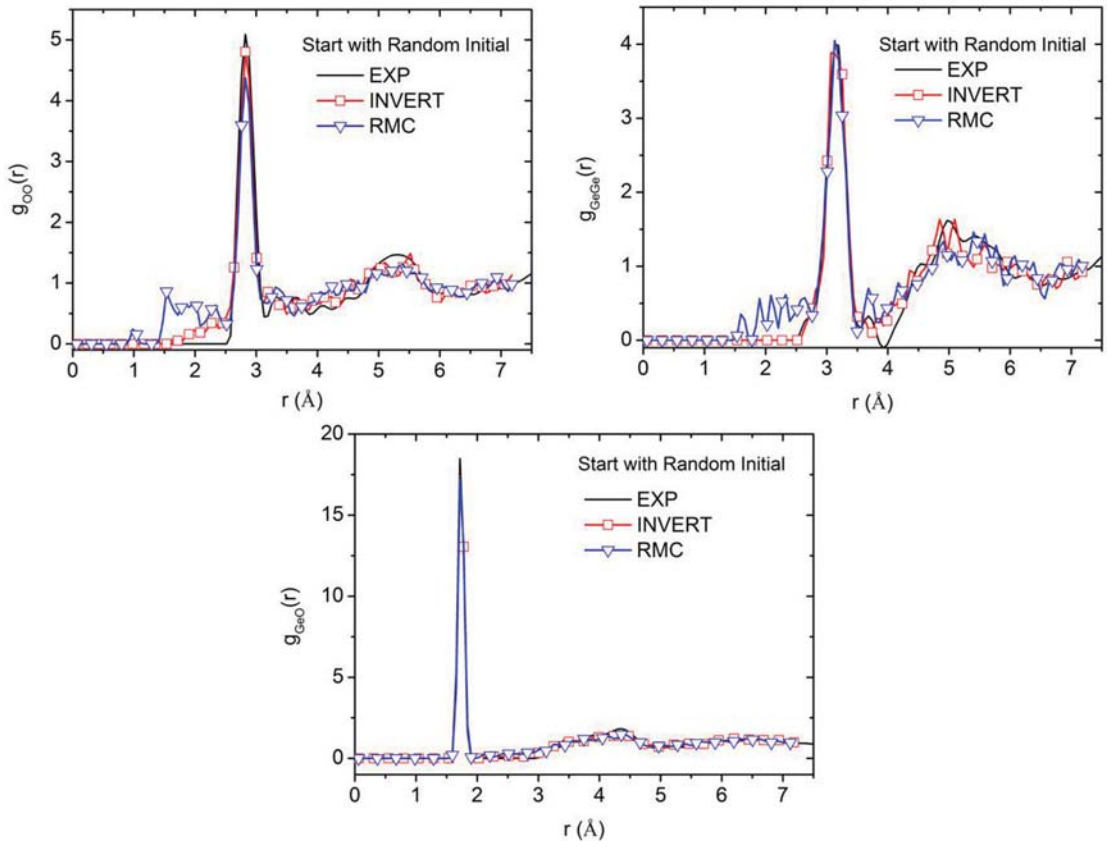

Figure 6.3: Comparison of partial radial distribution functions for 192-atom a-GeO_2 model obtained by different methods starting with random initial configuration. (See text.)

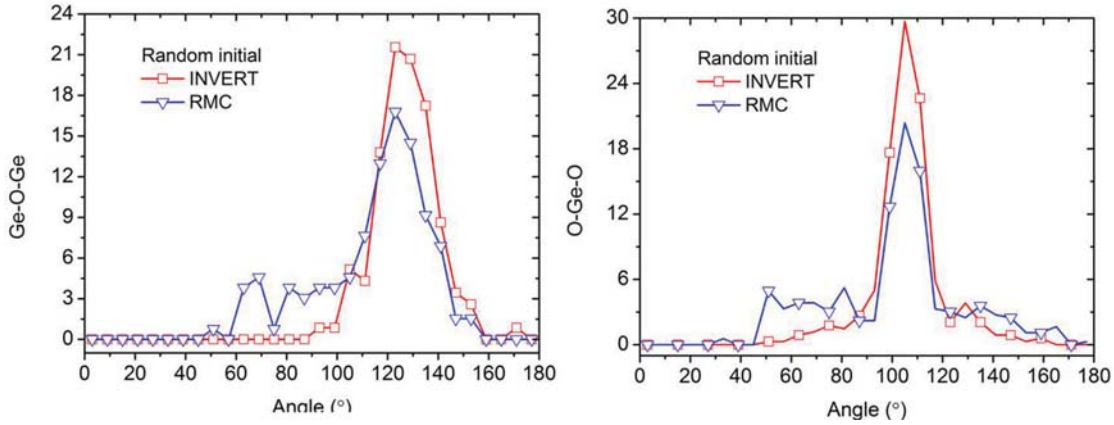

Figure 6.4: Comparison of angle distributions calculated for 192-atom a-GeO_2 model obtained by different methods starting with random initial configuration.

Table 6.1: Structural Statistics of 192-atom models

	INVERT(dec)	INVERT(ran)	RMC(dec)	RMC(ran)
n_{Ge}	3.81	3.75	3.8	3.6
n_O	1.91	1.99	2.1	1.85
$n_{Ge-Ge}(\%)$	0	0	1	5
n_{O-O} (%)	0	6	10	29
r_{Ge-O}(Å)	1.73	1.73	1.73	1.73
O-Ge-O(^{o})	109	109	109	109
Ge-O-Ge(^{o})	129	127	129	124

I see that all models have good fit to the Ge-O partials with peak position around 1.73Å, but a few homopolar bond exist in traditional RMC models and lead to unrealistic peaks in Ge-Ge and O-O partials. These results indicate that for both initial models, INVERT converges to a minimum faster and manage to avoid some particular local minima. The non-smooth pattern, compared with experimental data, is mainly due to the size effect. For the angle distribution, all models predict a similar peak position around 109^o for O-Ge-O and around 129^o Ge-O-Ge, which are close to experimental values 109.47^o and 132^o. However, INVERT provides a better O-Ge-O distribution and much better Ge-O-Ge distribution. Again, the unrealistic peak in angle distribution of RMC model is mainly due to the mis-coordinated atoms in the network. Considering different initial configurations, the decorated model, as expected, gives a better result than random initial, since the decorated model starts with perfect chemical order which provides a better starting point than random model. I report the structural statistics of these four models in Table 6.1. The result confirms that INVERT+RMC with decorated initial configurations gives the best result with $n_{Ge} = 3.8$. Compared with INVERT model, more homopolar bond exist in traditional RMC model. In Fig. 6.5, I show the topology of these

four models. Atoms involved in homopolar bonds are marked as gold/light/big for Ge and grey/light/small for O. The illustration indicates that there are more defects in the RMC models, implying a poorer chemical order, compared with INVERT+RMC, consistent with my prior experience[13]. All these results reveal that by fitting the partial RDFs for each distinct site, the INVERT method achieves a credible network while the unconstrained RMC result is not very chemically realistic. I should also point out that to obtain these models the RMC method is more computationally demanding than the INVERT method. (Since the INVERT+RMC model only consider the RDF for each individual site, it is an order N calculation; while it is order N^2 for traditional RMC to calculated the average RDF.) The RMC results could be improved by adding add-hoc constraints such as the coordination constraints, shortest distance constraints, which are not necessary for the INVERT+RMC method.

6.3.2 Low Density Amorphous Ice: a-H_2O

Another interesting case is Low Density Amorphous Ice (LDAI). In this approach, I use the simplest model for water molecules: O atoms connected rigidly to two H neighbors with bond length 1.0Å and bond angle 106^o. For a-H_2O, one possible model is that water molecules are packed in a way such that O atom with its first four O neighbors form a tetrahedral structure with medium range order[85]. Since intramolecular OH bonds are known, the peaks arising from O-H bond within small r region are often suppressed in reported RDF data. Thus, the H_2O molecules are often treated as rigid units and RMC is used only to fit the intermolecular peaks. Molecular dynamic simulations have also been used to model a-H_2O, but density functional theory (DFT) doesn't correctly treat the weak interactions like hydrogen bonding properly, and fails to reproduce experimental RDF data. In this section, I show that the RMC+INVERT method provides a convenient way to

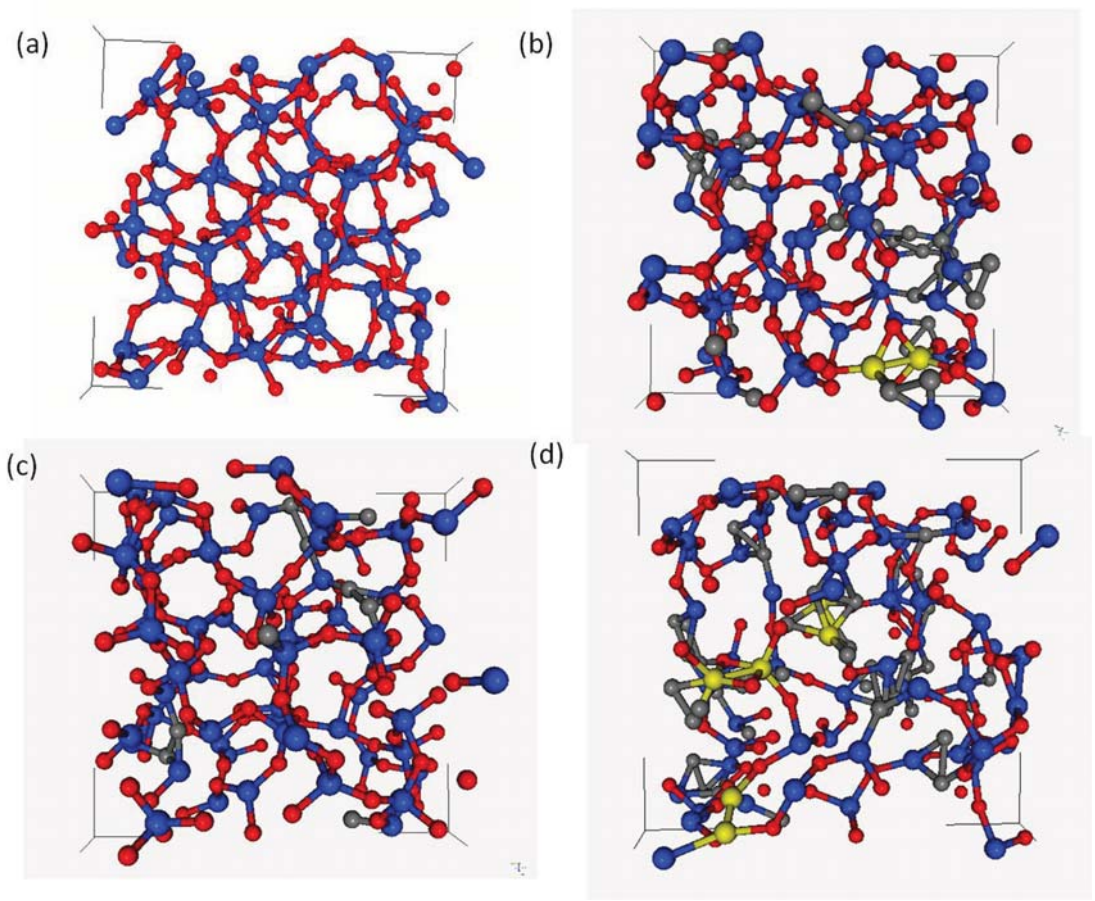

Figure 6.5: (color online)Comparison of topology of 192-atom a-GeO_2 obtained by (a)INVERT with decorated initial; (b)traditional RMC with decorated initial, (c)INVERT with random initial and (d)RMC with random initial. Blue(dark) and big atoms are Ge; gold(light) and big atoms are Ge atoms with homopolar bond(trouble Ge site); red(dark) and small atoms are O; grey(light) and small atoms are O atoms with homopolar bond(trouble O site).

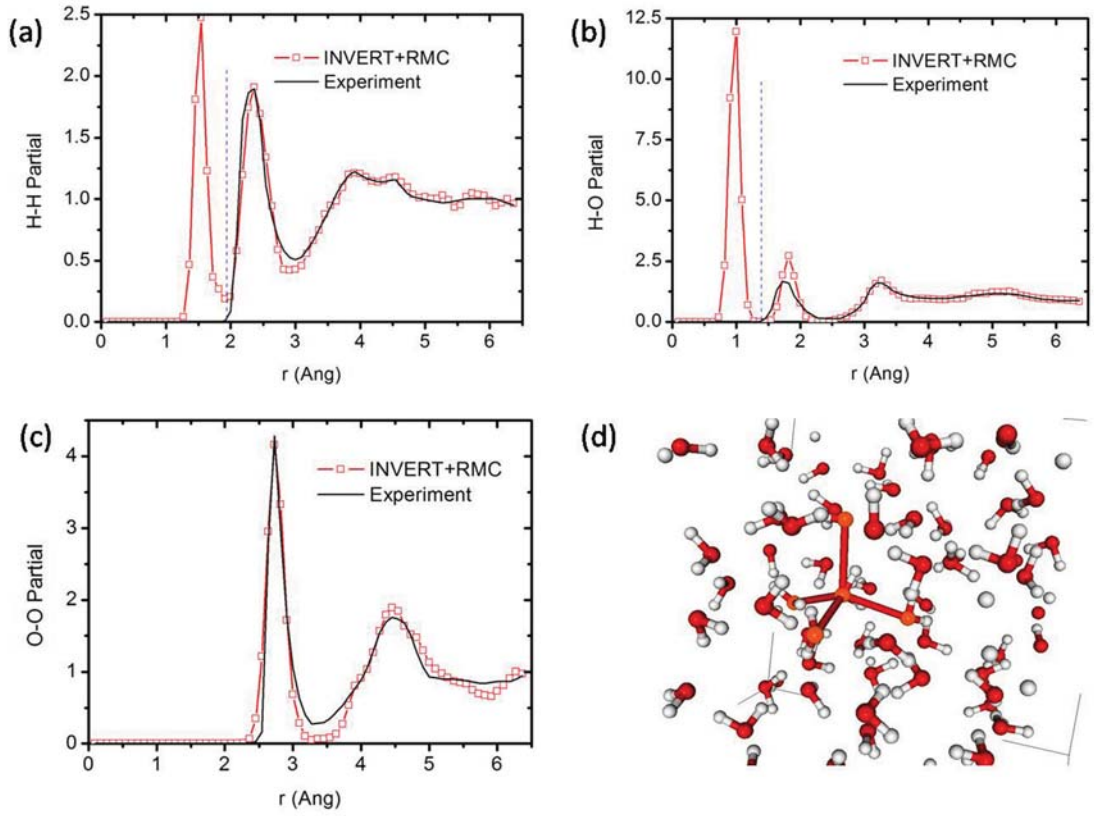

Figure 6.6: Three partial distribution functions and structure for 192-atom a-H_2O. Red(bigger) atoms are O and grey(small) atoms are H.

model LDAI, and it might improve DFT result on medium range order and generate an experiment credible model, perhaps using ECMR[3].

The rigid molecule constraint could be realized by setting the average distance to a constant value from atoms to their neighbors in the variance term. For example, for an O site, the distance to its first two H neighbors is fixed to 1.00Å; for an H site, the distance to its first H neighbor is set to be 1.6Å (this satisfies the H-O-H angle requirement). For the RDF part, I could still fit partial RDF but ignore the first peak in O-H and H-H partial. I start with previously relaxed models through DFT. 648- and 192-atom models are generated. The fitting result for 192-atom cell is plotted in Fig. 6.6 and compared to experiment[85]. In Fig. 6.6(a) and (b), I only fit the large-r region (r to the right of the dashed line) for H-H and O-H partials. After fitting, the first peaks in O-H and H-H partials are centered at 1.00Å and 1.6Å which implies the intramolecular structure is maintained. Compared with experimental data, peaks almost perfectly fit the H-H, O-O partials, but are a little bit off for O-H partial. The off-fitting on second peak of O-H partial may be due to the fix-distance constraint and the weighting factors in the variance term. To improve this, the future work need to be done is to add tolerance and better weighting factors for the variance term. Considering the first minimum after the primary peak, experiment data show a higher value which RMC+INVERT can not fit perfectly. The final configuration is also shown the in Fig. 6.6(d). One sample is shown in this plot showing how O and its four neighbors may form a tetrahedral structure.

I plot the angle distribution in Fig. 6.7. Again, the plot reveals the short range order and medium range order for water molecules. H-O-H distribution possess a peak at 103^o which is close to 106^o and represents the V-shape water molecule. The major peak in O-O-O distribution is located at 109^o, implying a tetrahedral structure.

Finally, by fixing the average distance in the variance term and assigning low tolerance, INVERT+RMC could easily handle the rigid unit constraint. Meanwhile, the

RDF term could be applied to fit second peak and force maximum uniformity in medium range order.

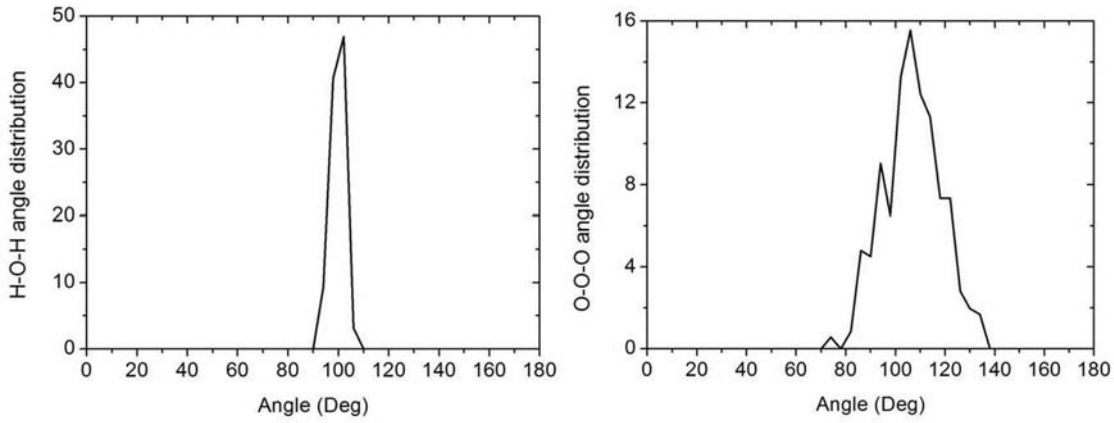

Figure 6.7: H-O-H intramolecular angle and O-O-O intermolecular angle distribution for 192-atom a-H_2O.

6.4 Conclusions

I have developed the INVERT+RMC method to fit experimental data of partial radial distribution functions. The result on a-GeO_2 indicates that the coordination number and angle distribution both are improved by using INVERT technique. For the a-H_2O case, fixing the average distance in the variance term and assigning these terms low tolerance allows the technique to handle the rigid unit constraint. I address that the INVERT+RMC method is not a panacea. For non-uniform system, it is hard to apply and needs to be reconsidered. Moreover, the information from structure factor should be also combined together with INVERT into modeling process to get better models.

7 Chapter: Conclusions and Future Work

7.1 Summary of the dissertation

In this dissertation, I reviewed the concept of direct and biased modeling, discussed various modeling techniques, applied them to build atomistic models of amorphous materials and described their structure and electronic structure properties through a set of analysis methods.

In direct modeling category, the "melt-and-quench" method can be simply applied to model any amorphous system, but it requires long thermal equilibration time and appropriate quench rate and it may create too many defects into the final model. Thus, it could be extremely time consuming for large system. Computer alchemy technique, while useful only for very special cases, if appropriately applied, is a very efficient method to achieve atomistic models. However, the species currently studied need to form similar structure with another species whose atomistic model must be known. Another modeling technique, the Building Block modeling, could also provide a short-path to generate large models.

For biased modeling, I mainly focused on developing the INVERT technique. Compared with traditional RMC, the INVERT method is more efficient and has the potential to provide a topologically unique model based on experimental diffraction data. However, I should point out that no method is without limitation, and INVERT+RMC is no exception. For systems that are not structurally uniform, the method is difficult to apply. In the future, the *ab-initio* modeling and biased modeling should be combined together, such as ECMR [4], and to obtain better atomistic models.

With reliable models available, I could predict the structural and electronic properties of amorphous materials. Based on "melt-and-quench" technique and computer alchemy, I generated 64-atom and 250-atom a-InN models which are the first *ab-initio* models ever

proposed for amorphous InN [49]. I found that homopolar bonds are rare in the system and the atoms form tetrahedral structures. A tiny electronic gap was observed. For a-GaN [86], through computer alchemy technique, I made 250-atom and 64-atom models which show improved features compared to original model published in 1997 [45]. The optical gap is estimated to be 3.0 eV and the dielectric functions are also described for the first time. In the study of phase change memory material, I obtain a-$Ge_2Sb_2Te_5$ by *ab-initio* molecular dynamic simulations [51]. I tracked the dynamic changes of network at 500 K, and correlated the structural changes in the course of the simulation with changes in electronic structure. HF calculations give a 0.4 eV electronic gap for the amorphous phase. I found that Te-p, Sb-p, Ge-p, Ge-s, and Sb-s orbitals are most important to tail states and affect the magnitude of the gap. Sixfold octahedral Ge and fourfold tetrahedral Ge give rise to similar gaps, but fourfold octahedral Ge results in a bigger gap with both shifted valence-band and conduction-band tails. Considerable fluctuation of the electronic gap is observed even for a model in equilibrium. By applying the building block method, I successfully obtained experiment credible g-$Ge_2As_4Se_4$ and g-$AsGe_{0.8}Se_{0.8}$ models [11]. The coordination statistics indicate that the "8-N" rule is often violated in these two ternary chalcogenide glasses. I also found a 0.34 eV band gap with a mid-gap state for g-$Ge_2As_4Se_4$ and a 0.38 eV band gap for g-$AsGe_{0.8}Se_{0.8}$, which could be well underestimated by the LDA method. Finally, I proved that imposing spatial uniformity may significantly improve the atomistic model in the case of a-GeO_2 and a-H_2O [14]. The 192-atom a-GeO_2 and a-H_2O models are obtained and their radial distribution functions, angle distribution functions and structural properties are described in detail. I conclude that a-GeO_2 models exhibit similar tetrahedral structure with a-SiO_2. The low density water model could be described as that water molecules are packed in a way such that O atom with its first four O neighbors forms a tetrahedral structure with medium range order.

7.2 Future work

From the study on a-InN and a-GaN, similar to oxides, the valence tail and conduction tail show a large asymmetry with the conduction tails totally delocalized. This result is somewhat similar to oxides but has not been previously reported for nitrides. The asymmetry indicates that the n-type and p-type doping for nitrides should be quite different. Further calculations are needed to study the structure and, especially, the electronic structure of a-BN and a-AlN and to summarized the general properties for nitrides. For Ge-Sb-Te system, the recent experimental results indicate that there are two kinds of Ge-Te bond with different bond length [87]. However, these two different bonds are hard to observe in the smaller atomistic model. Thus, large models of g-$Ge_2Sb_2Te_5$ are definitely required to obtain better statistics and to rule out the size effect. Further more, Matsunaga and co-authors [88] reported the recent experiment results and models on $Ag_{3.5}In_{3.8}Sb_{75.0}Te_{17.7}$ and compared with the Ge-Sb-Te alloys. The Ag doped Ge-Sb-Te system will be a new topic to study. The fundamental study of Building Block method is still needed, and a simple system such as a-Se will be a good starting point. The INVERT method gained success to model uniform system, but it is need to be further developed to model non-uniform system such as g-Ge-Se. Finally, a complete theory of H passivation in B or P doped a-Si:H is still missing. The long MD runs to study the thermal stability of B, P tetrahedral structure in a-Si, the interaction between H and impurities at high temperatures in a-Si:H, and the H passivation in a-Si:H with high concentrations of impurities distributed are still required.

References

[1] de la RosaFox, N., Esquivias, L., Villares, P., and Jimenez-Garay, R. *Phys. Rev. B* **33**(6), 4094–4099 Mar (1986).

[2] Nipko, J. C., Loong, C.-K., Balkas, C. M., and Davis, R. F. *Applied Physics Letters* **73**(1), 34–36 (1998).

[3] Drabold, D. A. *Europ Physics Journal B* **68**(1), 1 (2009).

[4] Biswas, P., Tafen, D. N., Inam, F., Cai, B., and Drabold, D. A. *Journal of Physics: Condensed Matter* **21**(8), 084207 (2009).

[5] Colombo, L. *Rivista del Nuovo Cimento* **28**(10), 1 Oct (2005).

[6] Lewis, L. J. and Mousseau, N. *Computational Materials Science* **12**(3), 210 – 241 (1998).

[7] Martin, R. M. *Electronic structure: basic theory and practical methods*. Cambridge University Press, Cambridge, UK, (2004).

[8] Hohenberg, P. and Kohn, W. *Phys. Rev. B* **136**, 864–871 (1964).

[9] Kohn, W. and Sham, L. J. *Phys. Rev. A* **140**, 1133–1138 (1965).

[10] Zhang, X. *Theoretical studies of structural, electronic and optical properties of amorphous chalcogenide materials*. Dissertation, Ohio University, March (2001).

[11] Cai, B., Zhang, X., and Drabold, D. A. *Phys. Rev. B* **83**(9), 092202 Mar (2011).

[12] Kresse, G. and Furthmüller, J. *Phys. Rev. B* **54**(16), 11169–11186 Oct (1996).

[13] Cliffe, M. J., Dove, M. T., Drabold, D. A., and Goodwin, A. L. *Phys. Rev. Lett.* **104**(12), 125501 Mar (2010).

[14] Cai, B., Goodwin, A. L., and Drabold, D. A. *Modelling and Simulation in Materials Science and Engineering* **19**(3), 035010 (2011).

[15] Pan, Y., Inam, F., Zhang, M., and Drabold, D. A. *Phys. Rev. Lett.* **100**(20), 206403 May (2008).

[16] Drabold, D. A., Li, Y., Cai, B., and Zhang, M. *Phys. Rev. B* **83**(4), 045201 Jan (2011).

[17] Lee, S. J. *Japanese Journal of Applied Physics* **37**(Part 1, No. 11), 5990–5993 (1998).

[18] Zhang, X., Chua, S.-J., Liu, W., and Li, P. *Physica Status Solidi (b)* **216**(1), 307–310 (1999).

[19] Wu, J., Walukiewicz, W., Shan, W., Yu, K. M., Ager, J. W., Haller, E. E., Lu, H., and Schaff, W. J. *Phys. Rev. B* **66**(20), 201403 Nov (2002).

[20] Wu, J., Walukiewicz, W., Yu, K. M., Ager, J. W., Haller, E. E., Lu, H., Schaff, W. J., Saito, Y., and Nanishi, Y. *Applied Physics Letters* **80**(21), 3967–3969 (2002).

[21] Davydov, V., Klochikhin, A., Emtsev, V., Ivanov, S., Vekshin, V., Bechstedt, F., Furthmller, J., Harima, H., Mudryi, A., Hashimoto, A., Yamamoto, A., Aderhold, J., Graul, J., and Haller, E. *Physica Status Solidi (b)* **230**(2), R4–R6 (2002).

[22] Tansley, T. L. and Foley, C. P. *Journal of Applied Physics* **59**(9), 3241–3244 (1986).

[23] Higashiwaki, M. and Matsui, T. *Journal of Crystal Growth* **269**(1), 162 – 166 (2004). Proceedings of the First ONR International Indium Nitride Workshop.

[24] Haddad, D. B., Dai, H., Naik, R., Morgan, C., Naik, V. M., Thakur, J. S., Auner, G. W., Wenger, L. E., Lu, H., and Schaff, W. J. *Mater. Res. Soc. Symp. Proc.* **798**(Y12.7), 2493 (2004).

[25] Butcher, K. and Tansley, T. *Superlattices and Microstructures* **38**(1), 1 – 37 (2005).

[26] Stampfl, C. and Van de Walle, C. G. *Phys. Rev. B* **59**(8), 5521–5535 Feb (1999).

[27] Stampfl, C., Van de Walle, C. G., Vogel, D., Krüger, P., and Pollmann, J. *Phys. Rev. B* **61**(12), R7846–R7849 Mar (2000).

[28] Wei, S.-H., Nie, X., Batyrev, I. G., and Zhang, S. B. *Phys. Rev. B* **67**(16), 165209 Apr (2003).

[29] Khoshman, J. M. and Kordesch, M. E. *Journal of Non-Crystalline Solids* **352**(52-54), 5572 – 5577 (2006).

[30] Mousseau, N. and Barkema, G. T. *Journal of Physics: Condensed Matter* **16**(44), S5183 (2004).

[31] Perdew, J. P. and Zunger, A. *Phys. Rev. B* **23**(10), 5048–5079 May (1981).

[32] Kresse, G. and Hafner, J. *Journal of Physics: Condensed Matter* **6**(40), 8245 (1994).

[33] Tafen, D. N. and Drabold, D. A. *Phys. Rev. B* **71**(5), 054206 Feb (2005).

[34] Ordejón, P., Drabold, D. A., Martin, R. M., and Itoh, S. *Phys. Rev. Lett.* **75**(7), 1324–1327 Aug (1995).

[35] Monkhorst, H. J. and Pack, J. D. *Phys. Rev. B* **13**(12), 5188–5192 Jun (1976).

[36] Pearton, S. J., Ren, F., Zhang, A. P., and Lee, K. P. *Materials Science and Engineering: R: Reports* **30**(3-6), 55 – 212 (2000).

[37] Zhang, Z., Pan, X., Wang, T., Xie, E., and Jia, L. *Journal of Alloys and Compounds* **467**(1-2), 61 – 64 (2009).

[38] Pearton, S. J. and Ren, F. *Advanced Materials* **12**(21), 1571–1580 (2000).

[39] Hariu, T., Usuba, T., Adachi, H., and Shibata, Y. *Applied Physics Letters* **32**(4), 252–253 (1978).

[40] Hassan, Z., Kordesch, M., Jadwisienzak, W., Lozykowski, H., Halverson, W., and Colter, P. In *Microcrystalline and Nanocrystalline Semiconductors-1998,* Canham, LT and Sailor, MJ and Tanaka, K and Tsai, CC, editor, volume 536 of *Materials Research Society Symposium Proceedings*, 245–250 (Mat Res SocMATERIALS RESEARCH SOCIETY, 506 KEYSTONE DRIVE, WARRENDALE, PA 15088-7563 USA, 1999). Symposium on Microcrystalline and Nanocrystalline Semiconductors, at the 1998 MRS Fall Meeting, BOSTON, MA, NOV 30-DEC 03, 1998.

[41] Hassan, Z., Ibrahim, K., Kordesch, M., Halverson, W., and Colter, P. *International Journal of Modern Physics B* **16**(6-7), 1086–1090 MAR 20 (2002). International Conference on Material for Advanced Technologies,SINGAPORE, Jul 01-06, 2001.

[42] Al-Zouhbi, A. and Al-Din, N. S. *Optical Review* **15**(5), 251–254 Sep (2008).

[43] Bittar, A., Trodahl, H., Kemp, N., and Markwitz, A. *Applied Physics Letters* **78**(5), 619–621 Jan (2001).

[44] Kawashima, T., Yoshikawa, H., Adachi, S., Fuke, S., and Ohtsuka, K. *Journal of Applied Physics* **82**(7), 3528–3535 (1997).

[45] Stumm, P. and Drabold, D. A. *Phys. Rev. Lett.* **79**(4), 677–680 Jul (1997).

[46] Yu, M. and Drabold, D. *Solid State Communications* **108**(7), 413–417 (1998).

[47] Ishimaru, M., Zhang, Y., and Weber, W. J. *Journal of Applied Physics* **106**(5), 053513 (2009).

[48] Nord, J., Nordlund, K., and Keinonen, J. *Phys. Rev. B* **68**(18), 184104 Nov (2003).

[49] Cai, B. and Drabold, D. A. *Phys. Rev. B* **79**(19), 195204 May (2009).

[50] Pollard, W. *Journal of Non-crystalline Solids* **283**(1-3), 203–210 May (2001).

[51] Cai, B., Drabold, D. A., and Elliott, S. R. *Applied Physics Letters* **97**(19), 191908 (2010).

[52] Kobayashi, S., Nonomura, S., Ohmori, T., Abe, K., Hirata, S., Uno, T., Gotoh, T., Nitta, S., and Kobayashi, S. *Applied Surface Science* **113**, 480–484 Apr (1997). 8th International Conference on Solid Films and Surfaces (ICSFS-8), Osaka, Japan, Jul 01-05, 1996.

[53] Atta-Fynn, R., Biswas, P., and Drabold, D. A. *Phys. Rev. B* **69**(24), 245204 Jun (2004).

[54] Robertson, J. *Journal of Non-crystalline Solids* **354**(19-25), 2791–2795 May 1 (2008). 22nd International Conference on Amorphous and Nanocrystalline Semiconductors, Breckenridge, CO, Aug 19-24, 2007.

[55] Inam, F., Lewis, J. P., and Drabold, D. A. *Physica Status Solidi A-Applications and Materials Science* **207**(3, Sp. Iss. SI), 599–604 MAR (2010).

[56] Kwon, Y.-H., Shee, S. K., Gainer, G. H., Park, G. H., Hwang, S. J., and Song, J. J. *Applied Physics Letters* **76**(7), 840–842 (2000).

[57] Van de Walle, C., Stampfl, C., and Neugebauer, J. *Journal of Crystal Growth* **189**, 505–510 Jun (1998). 2nd International Conference on Nitride Semiconductors (ICNS 97), TOKUSHIMA CITY, JAPAN, Oct 27-31, 1997.

[58] Akola, J. and Jones, R. O. *Phys. Rev. B* **76**(23), 235201 Dec (2007).

[59] Hegedüs, J. and Elliott, S. R. *Nat. Mater.* **7**(5), 399 (2008).

[60] Wełnic, W., Botti, S., Reining, L., and Wuttig, M. *Phys. Rev. Lett.* **98**(23), 236403 Jun (2007).

[61] Naito, M., Ishimaru, M., Hirotsu, Y., Kojima, R., and Yamada, N. *Journal of Applied Physics* **107**(10), 103507 (2010).

[62] Lee, B.-S., Abelson, J. R., Bishop, S. G., Kang, D.-H., ki Cheong, B., and Kim, K.-B. *Journal of Applied Physics* **97**(9), 093509 (2005).

[63] Raty, J.-Y., Otjacques, C., Gaspard, J.-P., and Bichara, C. *Solid State Sciences* **12**(2), 193 – 198 (2010).

[64] Wuttig, M., Lusebrink, D., Wamwangi, D., Welnic, W., Gilleszen, M., and Dronskowski, R. *Nat. Mater.* **6**(2), 168 (2007).

[65] Haisty, R. and Krebs, H. *Journal of Non-Crystalline Solids* **1**(5), 427 – 436 (1969).

[66] Webber, P. J. and Savage, J. A. *Journal of Non-Crystalline Solids* **20**(2), 271 – 283 (1976).

[67] Nang, T. T., Okuda, M., and Matsushita, T. *Phys. Rev. B* **19**(2), 947–955 Jan (1979).

[68] Petri, I., Salmon, P. S., and Fischer, H. E. *Phys. Rev. Lett.* **84**(11), 2413–2416 Mar (2000).

[69] Hari, P., Taylor, P., King, W., and LaCourse, W. *Journal of Non-Crystal Solids* **198**(Part 2), 736–739 MAY (1996). 16th International Conference on Amorphous Semiconductors - Science and Technology (ICAS 16), KOBE, JAPAN, SEP 04-08, 1995.

[70] Salmon, P. S., Barnes, A. C., Martin, R. A., and Cuello, G. J. *Phys. Rev. Lett.* **96**(23), 235502 Jun (2006).

[71] Sankey, O. F. and Niklewski, D. J. *Phys. Rev. B* **40**(6), 3979–3995 Aug (1989).

[72] Lewis, J. P., Glaesemann, K. R., Voth, G. A., Fritsch, J., Demkov, A. A., Ortega, J., and Sankey, O. F. *Phys. Rev. B* **64**(19), 195103 Oct (2001).

[73] Borisova, Z. U. *Glassy Semiconductors*. Plenum, New York, (1981).

[74] Greaves, G. N. and Davis, E. A. *Philosophical Magazine* **29**(5), 1201–1206 (1974).

[75] Wyckoff, R. *Crystal Structures*. John Wiley, New York, (1963).

[76] Phillips, J. C. *Journal of Non-Crystalline Solids* **34**(2), 153–181 (1979).

[77] Thorpe, M. *Journal of Non-Crystalline Solids* **57**(3), 355–370 (1983).

[78] Ouyang, L. and Ching, W. Y. *Phys. Rev. B* **54**(22), R15594–R15597 Dec (1996).

[79] Biswas, P., Tafen, D. N., Atta-Fynn, R., and Drabold, D. *Journal of Physics: Condensed Matter* **16**(44), S5173 (2004).

[80] Biswas, P., Tafen, D. N., and Drabold, D. A. *Phys. Rev. B* **71**(5), 054204 Feb (2005).

[81] Salmon, P. S., Barnes, A. C., Martin, R. A., and Cuello, G. J. *Journal of Physics: Condensed Matter* **19**(41), 415110 (2007).

[82] Giacomazzi, L., Umari, P., and Pasquarello, A. *Phys. Rev. Lett.* **95**(7), 075505 Aug (2005).

[83] Wooten, F. and Weaire, D. In *Advances in Research and Applications,* Ehrenreich, H. and Turnbull, D., editors, volume 40 of *Solid State Physics*, 1 – 15, 15a, 17–32, 32a, 32b, 32c, 32d, 32e, 33–42. Academic Press (1987).

[84] Tafen, D. N. and Drabold, D. A. *Phys. Rev. B* **68**(16), 165208 Oct (2003).

[85] Pusztai, L. *Phys. Rev. B* **61**(1), 28–31 Jan (2000).

[86] Cai, B. and Drabold, D. A. *Submitted to Phys. Rev. B* Apr (2011).

[87] B. Prasai, B. Cai, M. E. K. and Chen, G. *Submitted to Phys. Rev. B* Apr (2011).

[88] Matsunaga, T., Akola, J., Kohara, S., Honma, T., Kobayashi, K., Ikenaga, E., Jones, R. O., Yamada, N., Takata, M., and Kojima, R. *Nat. Mater.* **10**(2), 129–134 Feb (2011).

[89] Street, R. *Hydrogenated Amorphous Silicon*. Cambridge University Press, Cambridge, UK, (2002).

[90] Santos, I., Castrillo, P., Windl, W., Drabold, D. A., Pelaz, L., and Marqués, L. A. *Phys. Rev. B* **81**(3), 033203 Jan (2010).

[91] Boyce, J. B. and Ready, S. E. *Phys. Rev. B* **38**(16), 11008–11018 Dec (1988).

[92] Fedders, P. A. and Drabold, D. A. *Phys. Rev. B* **56**(4), 1864–1867 Jul (1997).

The following work is submitted:

B. Cai and D. A. Drabold, Materials Research Society Proceedings (2011).

Appendix: Electronic Activity of Boron and Phosphorous Dopants in a-Si and a-Si:H

A.1 Introduction

By introducing B or P, a-Si:H may be doped either n-type or p-type [89], a point of profound technological importance. In c-Si, B and P doping has been extensively studied. Because of translational invariance, impurities are compelled to have the same local tetrahedral environment as Si. According to the 8-N rule, B atoms create a hole when they have Td symmetry, and P similarly donates an electron. The doping efficiency is almost 100%. In c-Si:H, H atoms passivate doping by relaxing the strain, and rendering B or P doping-inactive by enabling the impurities to become three-fold[89].

However, in contrast to c-Si, there is no periodic lattice in a-Si. The absence of a unique atomic environment leads to site-dependent doping as seen in studies with low concentration Boron[90]. However, theoretical studies on P doping and high concentration of B are still required. In a-Si:H, NMR[91] shows that, for B doping, 40% of the B has a nearby H at 1.6Å; for P doping, 50% of P has a H at 2.6Å. The doping efficiency is very low, and Boyce and Ready have conjectured that the sluggish doping may be due to H passivation[92]. But the atomistic mechanism of H passivation in doped a-Si:H is unclear.

In this paper, I report molecular dynamic simulations on B and P doped a-Si and a-Si:H, focusing on the electronic structure. For a-Si, I report the electronic density of states (EDOS) for various impurity concentrations. I attempt to find the effective doping and non-doping configurations. For a-Si:H, I mainly focus on describing the H passivation mechanisms with low concentration of impurities (¡2.0%). By manually placing H in the models, I am able to investigate energetically preferred positions and explore consequent electronic structure.

A.2 Model and Simulation

All calculations were performed using the plane wave code VASP with ultrasoft pseudopotentials and the local density approximation[12, 31, 32]. A previously generated defect-free 64-atom a-Si model was used as the initial configuration. B or P atoms were introduced into the network by substituting for Si atoms. Conjugate gradient relaxations were performed at constant volume. I obtained relaxed 1.6%, 3.1%, 7.8% and 12.5% B or P doped a-Si models. To study H passivation in B- or P-doped a-Si:H, I introduced H atoms at particular sites of the 1.6% B- or P-doped a-Si models with various distances from impurities.

A.3 Results and Discussion

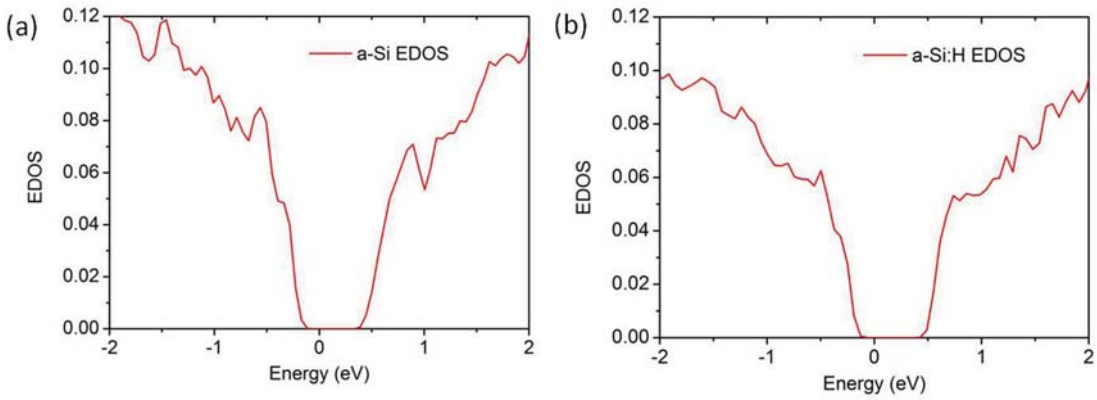

Figure A.1: (Color online) Electronic density of states (EDOS) (a) a-Si. (b) a-Si:H. The Fermi level is at 0eV.

I first present the electronic density of states of a 64-atom a-Si model and a 70-atom a-Si:H model with 8.5% H in Fig. A.1. Both a-Si and a-Si:H models exhibit gaps unsullied by defect states. In the following, I first discuss B- and P-doped a-Si with

impurity concentrations from 1.6% to 12.5%. Then, I investigate the mechanism of H passivation in both systems.

A.3.1 Boron doped a-Si

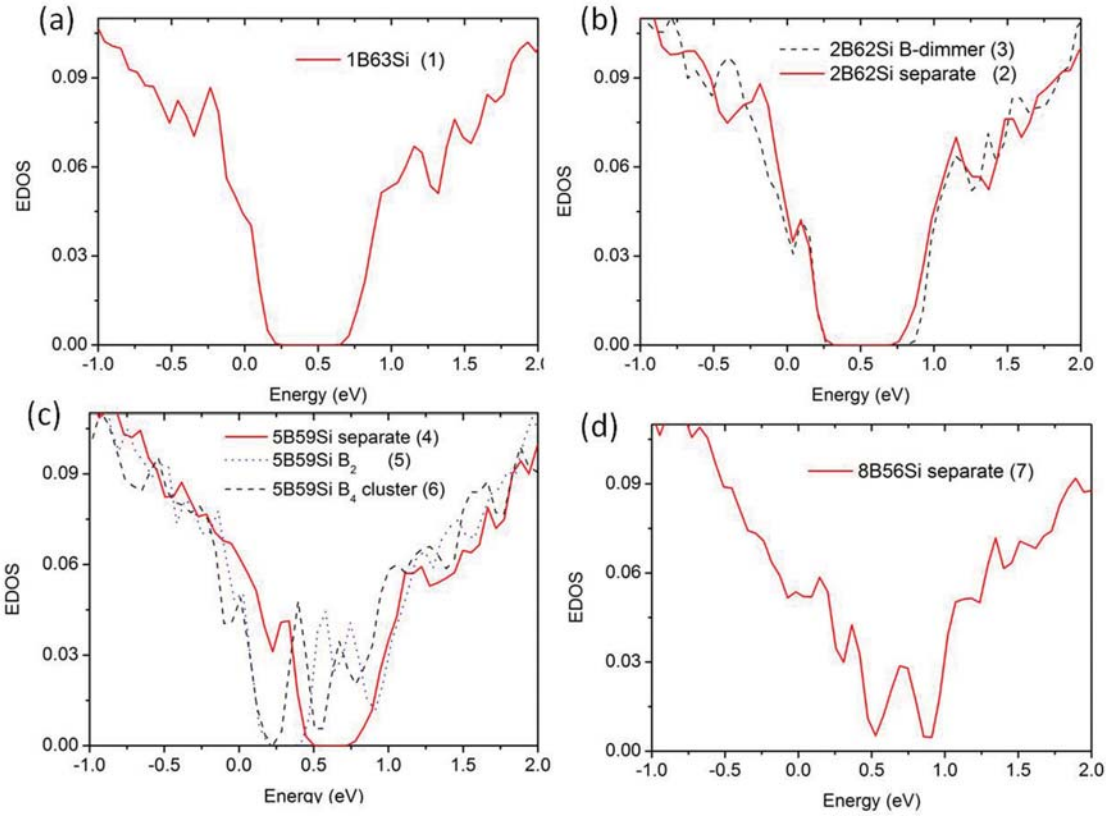

Figure A.2: (Color online) Boron doped a-Si with different concentrations. (a) 1.6% (b) 3.1% (c) 7.8% (d) 12.5%. In configuration (1), (2), (4) and (7), all B are bonded with four Si atoms. One B dimer is formed in configuration (3). Two B dimmers exist in configuration (5) and one B4 cluster formed in configuration (6). The Fermi level is at 0 eV.

I plot the EDOS of seven B-doping models [configuration (1)-(7)] in Fig. A.2. Overall, when B atoms are introduced substitutionally into the network, the Fermi level shifts toward the valence edge. In configuration (1), (2), (4) and (7), all B atoms are

four-fold and prefer to form three shorter bonds and one longer bond with Si. As concentration increases, more valence tail states are formed, and states move into the gap. Where B dimers or clusters are concerned, it seems that B-B bonds won't impact the doping as long as B atoms are four-fold as shown in EDOS of configuration (3). However, when more B dimers or clusters are formed, additional defect states appear near the conduction tail and they clutter the gap, as shown in configuration (5) and (6). Those defect states are associated with under- and over-coordinated Si atoms.

I conclude that tetrahedral B makes the Fermi level shift from mid-gap into the valence band tail and effectively dopes the system. However, as B concentration increase, more valence tail states are formed. B clusters may introduce tail and mid-gap states, which impact the electronic gap.

A.3.2 Phosphorus doped a-Si

I plot the EDOS of eight models [(1)-(8)] of P-doped a-Si in Fig. A.3. I found that tetrahedral P forms deep donor states and the Fermi level shifts toward the conduction band tail. As P concentration increases, more defect states appear, and the gap closes (configurations (1), (2), (5), and (8)). P dimers and clusters dope the system so long as all P are four-fold (Configuration (3),(5)), but they also lead to defects which give rise to tail states. If P atoms are three-fold (configuration (4)), the configuration is non-doping.

Thus, for P doping, tetrahedral P dopes the system by shifting the Fermi level into the conduction tail. As for B doping, as concentration increases, more defect states move into gap. Three-fold P is a non-doping configuration.

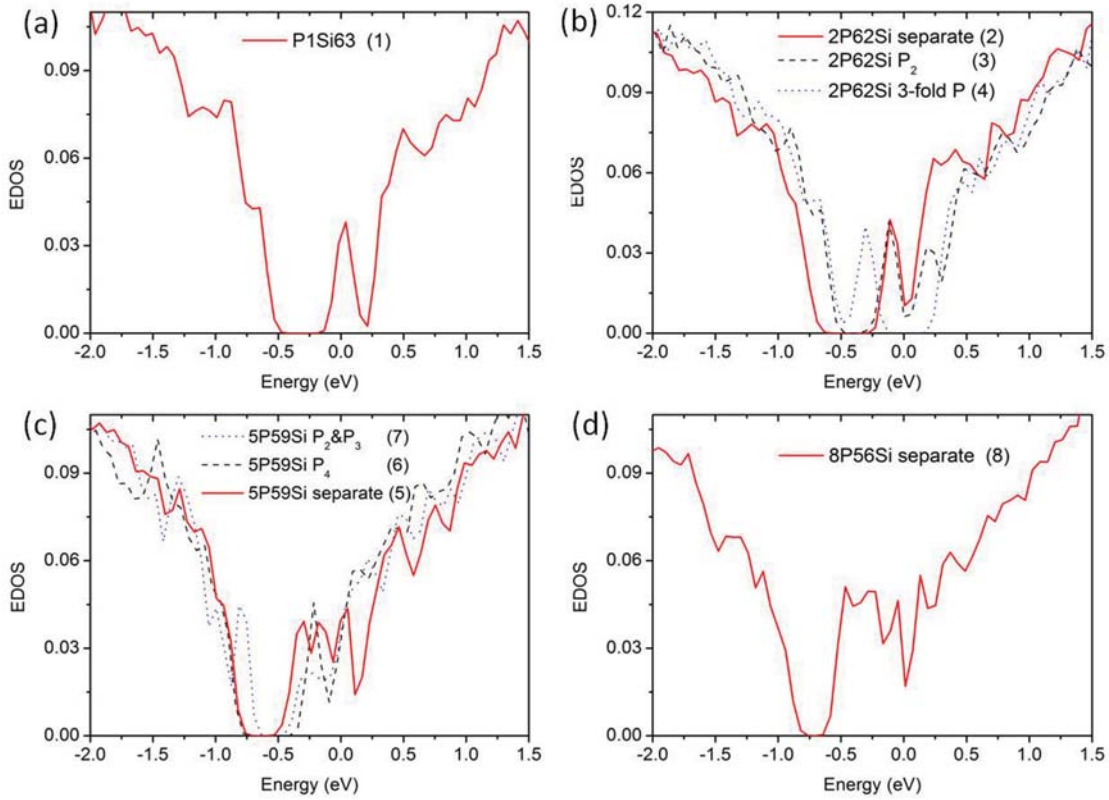

Figure A.3: (Color online)Phosphorus doped a-Si with different P concentration. (a) 1.6% (b) 3.1% (c) 7.8% (d) 12.5%. In (b) configuration(4) is non-doping configuration. The Fermi level is at 0eV.

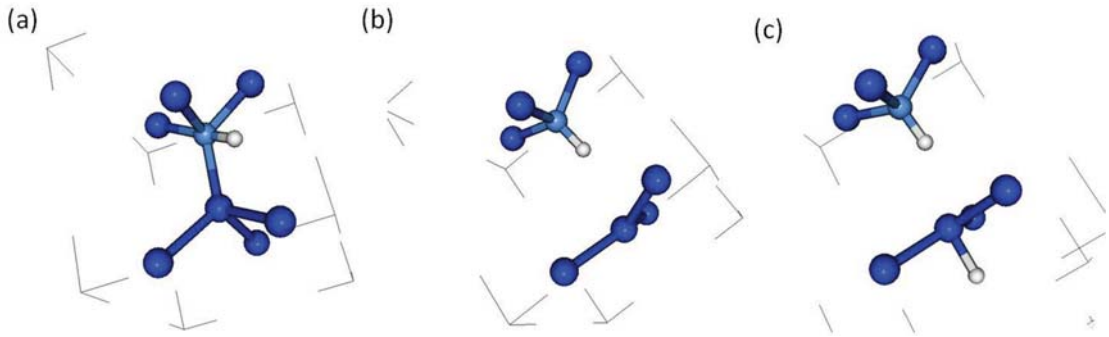

Figure A.4: (Color online) H passivation at B site. (a) H initially bond with B and B forms B(4,1) structure. (b) After relaxation, B becomes B(3,1) and leaves on Si DB. (c) Another H passivate the Si DB. The cyan (light,big) atom is B, blue(dark,big) atoms are Si and white(light,small) atom is H.

A.3.3 H passivation in B doped a-Si:H

I report first that B (3,1) (B atoms bonded with three Si atoms and one H atom) is an effective doping configuration. The structural evolution and corresponding EDOS is plotted in Fig. A.4 and Fig. A.5.

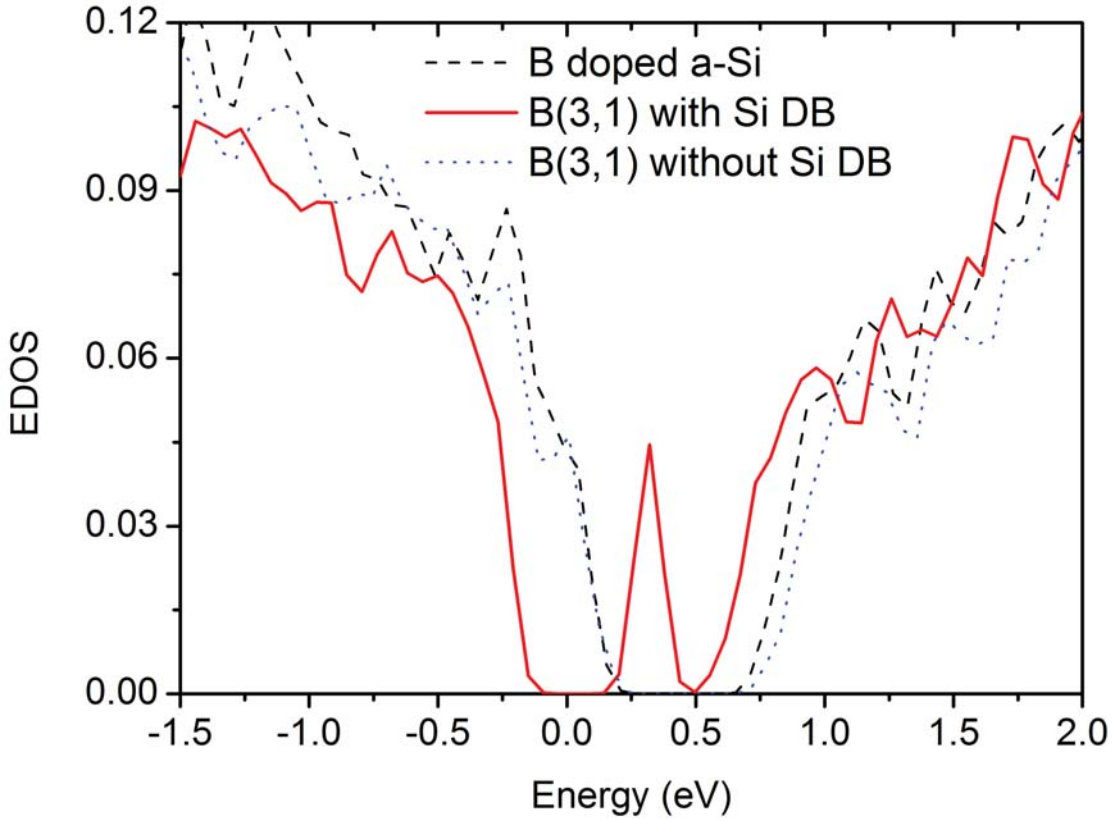

Figure A.5: (Color online) EDOS comparison of configurations during H passivation. The black (dashed) line shows the original B doped a-Si. The red(solid) line shows the EDOS of B(3,1) and one Si DB. The blue (dotted) line shows the EDOS when Si DB is passivated by another H. The Fermi level is at 0eV.

The H is initially attached to a B atom and makes B form a metastable unit B(4,1) as in Fig. A.4(a). After relaxation, H breaks one Si-B bond forming a B(3,1) structure and

leaves one Si DB, as in Fig. A.4(b). The EDOS of this configuration reveals that the Fermi level shifts back into gap. One mid-gap state forms due to the Si DB. However, if another H passivates the Si DB, like Fig. A.4(c), the Fermi level shifts into valence band tail once again and the mid-gap state disappears. Thus, I conclude that the B(3,1) without a Si DB is an effective doping conformation. This confirms the simulation results reported in Ref.[92].

Next, I show that H prefers to stay at the bond center (BC) when near a B atom and this BC H kills the doping. I show two cases of H passivation with different H-B distances in Fig. A.6. The top panel (a) of Fig. A.6 shows the situation in which H is initially bonded to a Si neighbor of the B atom. After relaxation, H breaks the Si-Si bond and stays at the BC forming a B-Si-H-Si structure, the top panel [Fig. A.6 (b)]. The EDOS shows that the Fermi level shifts back from the valence tail into the gap, indicating that the BC H kills the doping. The bottom panel of Fig. A.6 shows similar passivation with H bonded to a second neighbor Si of B atom and finally forming a B-Si-Si-H-Si structure. The EDOS of the B-Si-Si-H-Si structure shows that it is also a non-doping configuration. These results indicate that BC H sufficiently near a B atom will neutralize the doping. Notice that, in all cases, there is no reconstruction of B atoms – which are still 4-fold after relaxation. There is no Si DB left in the network and no defect states in the gap. Further calculations indicate that there is an "H poisoning range" for BC H passivation. If the distance between H and B is beyond about 6.0 Å, the passivation may not occur.

The mechanism of this BC H passivation at low B concentration may be related to charge interactions. In Ref.[90], at low concentration of B, it is confirmed that holes could be trapped at strained Si-Si bond centers. Thus, the H may compensate by staying at the BC and killing the doping structure. Another calculation in a-Si:H also confirm this. In a-Si:H, the Si (4,1) structure (Si bonded with four Si and one H) is stable. However, if one

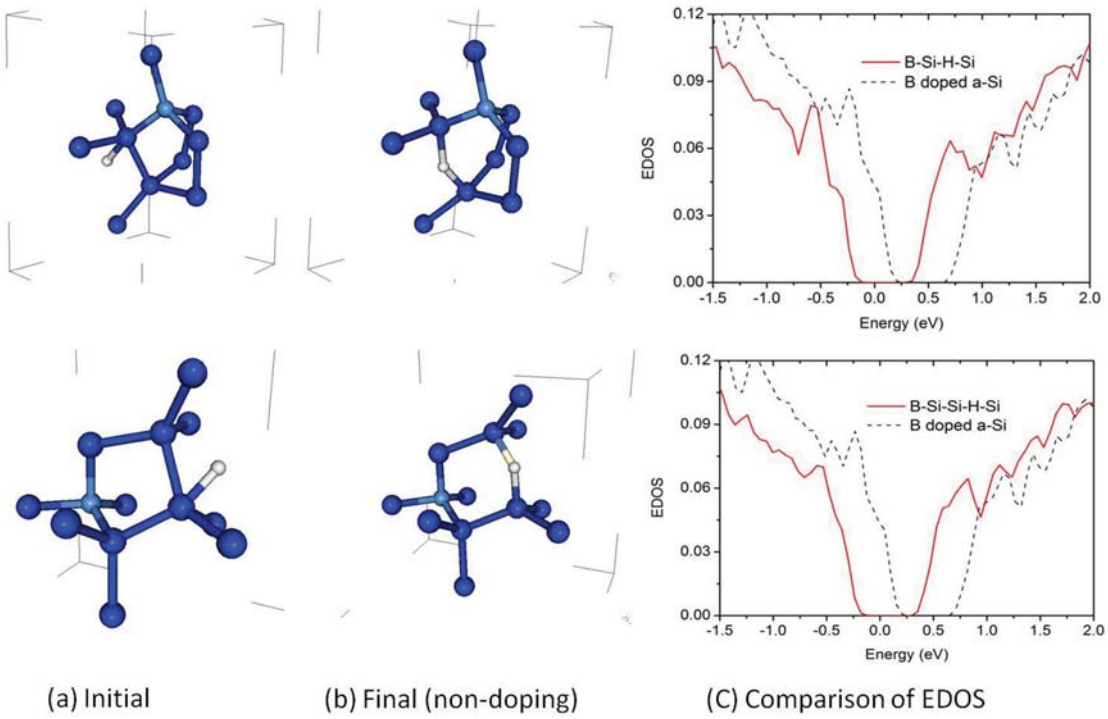

Figure A.6: (Color online) BC H passivates the doping. Top panel is the situation for B-Si-H-Si; bottom panel is the case for B-Si-Si-H-Si. The EDOS show the comparison between B doped a-Si and the final relaxation result when BC H exists in the network. The Fermi level is at 0eV.

electron is removed from the system, H tends to break a Si-Si bond and occupy the BC position. Considering the "H poisoning range", it may be related to the exciton radius [3], which is about 5.9Åin a-Si.

A.3.4 H passivation in P doped a-Si:H

In analogy with H passivation in B doped a-Si:H, I investigate H passivation in P-doped a-Si:H. I first report that P(3,1) is an effective doping configuration. The simulation is shown in Fig. A.7 and Fig. A.8. H is originally bonded to P forming a P(4,1) metastable structure. After relaxation, a P-Si bond breaks. H sticks to the P, forming a P(3,1) structure with a vestigial Si DB. The corresponding EDOS indicates that the deep donor state disappears, the Fermi level shifts back to the gap, and there is one mid-gap state formed (due to the Si DB). The configuration becomes non-doping. However, if another H passivates the Si DB as shown in Fig. A.7(c), the Fermi level again shifts to the conduction tail. Thus, I conclude that P(3,1) is an effective doping structure, but the Si DB in the network may kill the doping.

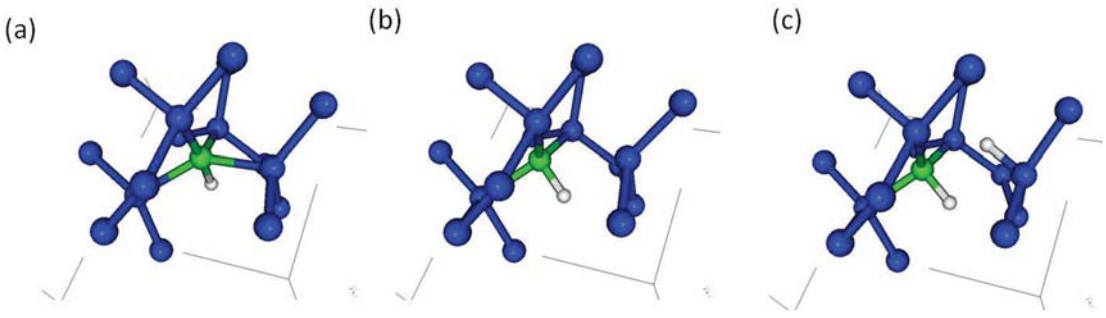

Figure A.7: (Color online) H passivation at P site. (a) H bond with P forming a P(4,1) structure. (b) H breaks one P-Si bond and makes P form P(3,1) with one Si DB. (c) another H passivates the Si DB. Green (light,big) atom is P. Blue(dark,big) atom is Si. White(small) atoms is H.

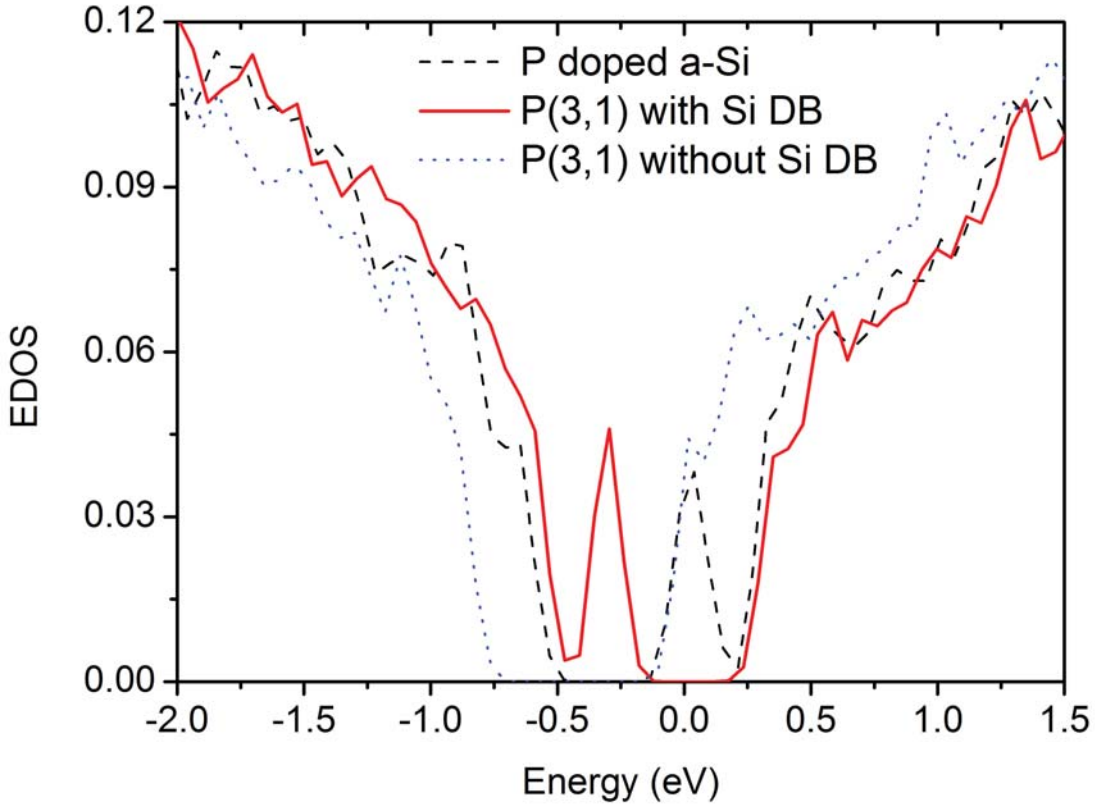

Figure A.8: (Color online) EDOS comparison of configurations during H passivation. Black (dashed) line is P doped a-Si. Red (solid) line is P(3,1) with one Si DB. Blue (dotted) line is the P(3,1) with another H passivate the Si DB. The Fermi level is at 0eV.

I then show two cases of H passivation in P doped a-Si:H in Fig. A.9. Unlike H passivation in B-doped a-Si:H, H in this network does not prefer BC position. In the top panel (a) of Fig. A.9, H is originally at BC of a P-Si bond and makes P(3,1) structure. However, after relaxation, the H-P bond ruptures, the H bonds with Si, and P becomes three-fold. The EDOS becomes non-doping as the deep donor state disappears and the Fermi level is now in the gap. The bottom panel of Fig. A.9 shows another case. H is initially at a bond center of Si-Si and forms a P-Si-H-Si structure. After relaxation, the network reconstructs as P becomes three-fold and H sticks to a Si DB. The doping is rendered inactive. Notice that there are no defect states in the EDOS of final configuration. Further calculations show that again there exists an "H poisoning range" (6.0Å). When H is sufficiently near a P site in a BC configuration, the network will reconstruct so that P becomes three-fold, H sticks to Si DB, and neutralizes the doping structure.

Unlike H passivation for B, H does not prefer the BC position, instead it prefers to bond with Si. This result is consistent with NMR, which implies that P often has a H neighbor around 2.6Åaway (not the first neighbor distance).

A.4 Conclusions

Tetrahedral B and P dope the system, but high concentration of impurities introduce mid-gap states. Clusters also create defect states in the gap. H passivation is a key to understanding doping efficiency. Covalently bonded H: B(3Si,1H), P(3Si,1H), Si(3Si,H) are effective doping states. There exists an "H poisoning range": for B doping, when H sufficiently near B, H breaks the bond and stays at the bond center; for P doping, H atoms bonds to Si and makes P three-fold. Most calculations in this paper are based on direct relaxations. I am currently performing long MD runs to study the thermal stability of B, P tetrahedral structure in a-Si, the interaction between H and impurities at high temperatures

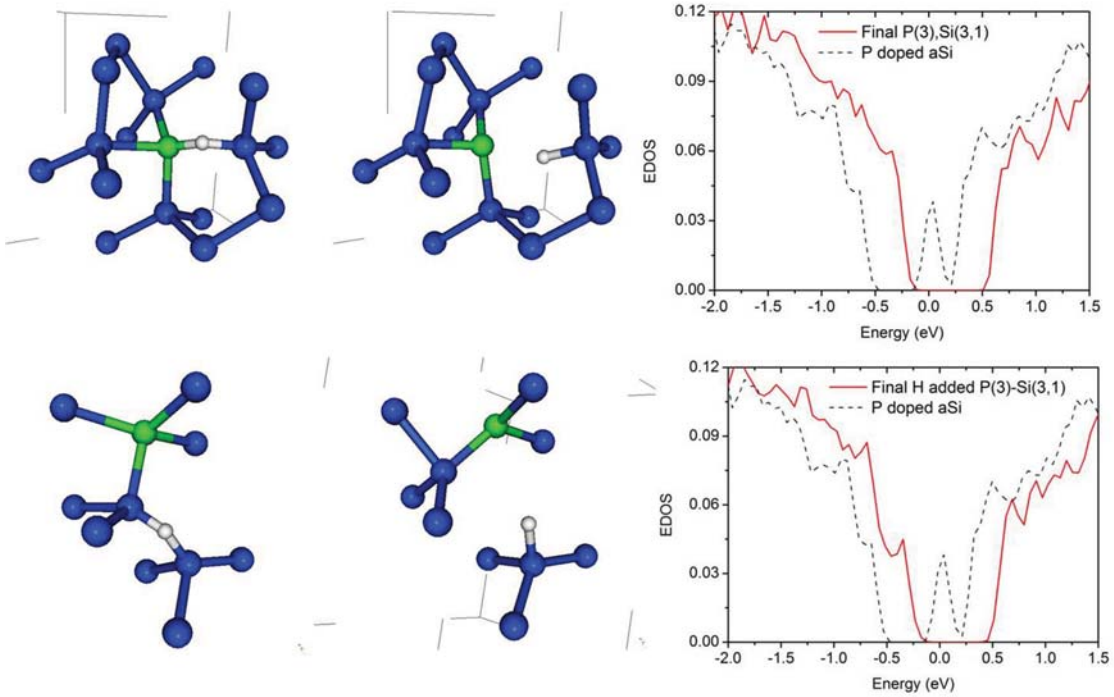

Figure A.9: (Color online) H passivation in P doped a-Si:H. Top panel, H originally formed P-H-Si; bottom panel, H originally formed p-Si-H-Si. After relaxation, in both cases, P becomes three fold and non-doping configurations. Green (light, big) atom is P. Blue(dark, big) atom is Si. White (light, small) atom is H. The Fermi level is at 0eV.

in a-Si:H, and the H passivation in a-Si:H with high concentrations of impurities distributed in various ways. Those results will appear in the future papers.

Thesis and Dissertation Services